




Universitetet
i Stavanger

Faculty of Science and Technology

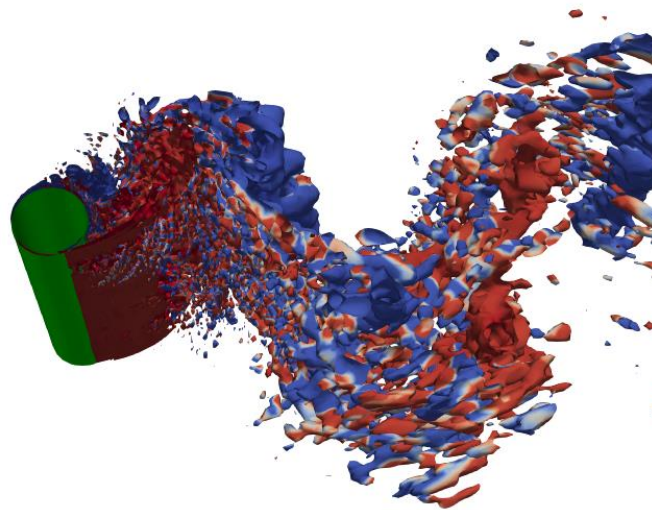
MASTER'S THESIS

Study program/specialization: MSc in Marine and Offshore Technology	Spring semester, 2021 Open / Restricted access
Author: Lukas Philip Fabricius	 (signature of author)
Supervisor: Prof. Muk Chen Ong Co-Supervisors: Dr. Guang Yin Marek Jan Janocha	
Title: Three-dimensional Numerical Simulations and Proper Orthogonal Decomposition Analysis of Flow Around a Flexibly Supported Circular Cylinder	
Credits: 30 ECTS	
Keywords: Flow-Induced Motions, CFD, circular cylinder, subcritical regime, Vortex induced vibrations	Number of pages: 85 + enclosure: 16 Stavanger, June 15, 2021

Three-dimensional Numerical Simulations and Proper Orthogonal Decomposition Analysis of Flow Around a Flexibly Supported Circular Cylinder

Autor:

Lukas Philip Fabricius



Supervisor:

Prof. Muk Chen Ong

Co-Supervisors:

Dr. Guang Yin

Marek Jan Janocha

UNIVERSITY OF STAVANGER

Faculty of Science and Technology Department of Mechanical and Structural Engineering and
Materials Science Master of Science Thesis, Spring 2021

Abstract

Numerical simulations of turbulent flow around stationary and vibrating cylinders at $Re = 3900$ are performed using the Large Eddy Simulation (LES) approach. Detailed convergence and validation studies confirm feasibility of the present model to accurately predict the Vortex-Induced Vibrations (VIV) and turbulent wake characteristics. The thesis is divided into seven chapters. First a brief introduction to the topic is given. Chapter 2 gives a brief review of the theory for flow around circular cylinders. In chapter 3 the theory of Computational Fluid Dynamics (CFD) is given. In chapter 4 a series of simulations for a stationary cylinder configuration with different mesh and time step parameters are performed to find an optimal balance between the computational cost and accuracy. Furthermore, simulation results are compared with an extensive dataset from multiple experimental studies showing a very good agreement of the present simulation results with the experimental data. In chapter 5 simulations of a self-excited cylinder vibrating in the cross-flow direction are performed at three different values of reduced velocity. The flow fields are analyzed and different vortex shedding modes are categorized and then compared with the vortex shedding map derived from forced oscillation tests. Proper Orthogonal Decomposition (POD) is performed on sampled data in the wake of the cylinder to analyze the turbulent flow. The present numerical model is found to give accurate predictions with respect to essential parameters affecting the fluid-structure interaction of circular cylinder in the subcritical regime. In chapter 6 a conclusion of the results is presented and chapter 7 presents recommendation for future work.

Acknowledgments

I would like to thank Marek Jan Janocha for all his continuously helpful guidance and the patience to answer all my questions during this project.

I would like to thank Dr. Guang Yin and Prof. Muk Chen Ong for technical guidance and to give me the opportunity to develop my skills at the University of Stavanger.

I would like to thank the University of Stavanger, Department of Mechanical and Structural Engineering and Material Science for making it possible to write this thesis.

Computational support for this project was provided by Norwegian Metacenter for Computational Science (NOTUR) under Project No. NN9372K, which is greatly acknowledged.

Stavanger, Norway

June 2021

Lukas Philip Fabricius



Contents

- 1 Introduction 1
 - 1.1 Background and Motivation 1
 - 1.2 Problem Definition and Objectives of the Thesis..... 2
 - 1.3 Outline of the Thesis 2
 - 1.4 Previous Work..... 3
- 2 Flow around Circular Cylinders 5
 - 2.1 Turbulence..... 5
 - 2.2 Boundary Layer 5
 - 2.2.1 Flow Separation..... 6
 - 2.3 Flow Regimes Around Circular Cylinder..... 6
 - 2.4 Mechanism of Vortex Shedding 7
 - 2.4.1 Vortex Shedding Frequency 10
 - 2.5 Forces on a Circular Cylinder in a Steady Flow..... 10
 - 2.6 Vortex Shedding Patterns 11
 - 2.7 Vortex Induced Vibration..... 12
 - 2.7.1 Reduced Velocity 13
 - 2.7.2 Mass-ratio..... 13
 - 2.7.3 Added Mass 13
 - 2.7.4 Lock-in 14
 - 2.8 Response Amplitude..... 16
- 3 Computational Fluid Dynamics..... 18
 - 3.1 Governing Equations 18
 - 3.2 The Finite Volume Method 20
 - 3.2.1 Spatial Discretization..... 20
 - 3.2.2 Temporal Discretization 20
 - 3.3 Numerical Model and Approach 20
 - 3.4 Turbulence Modeling 21

3.5	Mesh Generation	21
3.6	Assessment of Mesh Quality	23
4	Simulation of Fluid Flow around Stationary Cylinder	25
4.1	Numerical Domain and Computational Grids	25
4.2	Computational Mesh	26
4.3	Mesh Convergence Study	26
4.4	Time step Convergence Study	30
4.5	Validation Study	30
5	Simulations of Self-excited Cylinder Vibrations	36
5.1	Two-Point Correlations in the Wake	42
5.2	Proper Orthogonal Decomposition	48
5.2.1	POD mode distribution on XY-plane	50
5.2.2	POD mode distribution on YZ-planes	57
6	Conclusion	84
7	Future Work	85
7.1	VIV Mitigation	85
7.2	Wake Induced Vibrations (WIV)	85

List of Figures

Figure 1: The development of the boundary layer for flow over a flat plate, and the different flow regimes. Not to scale. (Çengel and Cimbala 2006, 579).....	6
Figure 2: Shear layer separation (Sumer and Fredsøe 2006, 7).	6
Figure 3: Flow regions around a circular cylinder	7
Figure 4: Vortex shedding (Sumer and Fredsøe 2006, 8)	8
Figure 5: Strouhal number for smooth circular cylinder. Experimental data from: Solid curve: (C. Williamson 1989) Dashed curve (Roshko 1961). Dots: (Schewe 1983) Figure from (Sumer and Fredsøe 2006, 10)	10
Figure 6: Vortex shedding patterns. (Williamson and Roshko 1988) and (Morse and Williamson 2009)	12
Figure 7: Map of vortex shedding patterns occurring for different combinations of y/D and Ur from Morse and Williamson (2009) at $Re = 4000$	12
Figure 8: Cross-flow response of flexibly mounted cylinder in steady current (C. Feng 1968) (plot taken from (Sumer and Fredsøe 2006, 356)).....	15
Figure 9: Schematic illustration of lock-in frequency for high (a) and low (b) mass-ratio (Sumer and Fredsøe 2006, 360).	16
Figure 10: Amplitude response for low and high mass-damping systems (Vertical axes represent the vibration amplitude and the horizontal axes represent the reduced velocity) (Khalak and Williamson 1999, 822).....	17
Figure 11: Grid terminology (Bakker 2002)	21
Figure 12: Typical cell shapes (Bakker 2002)	22
Figure 13: Structured (a) and Unstructured (b) mesh.....	22
Figure 14: Smoothness of cells (Bakker 2002)	23
Figure 15: Aspect ratio (Bakker 2002).....	23
Figure 16: Refined mesh in the region of the boundary layer	24
Figure 17: Schematic of the computational domain with imposed boundary conditions.....	25
Figure 18: Computational grid overview in x - y plane, dimensions given in terms of cylinder diameter (D). In the spanwise (z -axis) direction the grid is formed by extruding n -times the presented 2D grid using uniform spacing.	26
Figure 19: Pressure coefficient (C_p) over the surface of the cylinder for different mesh variants.....	27
Figure 20: Normalized time- and spanwise-averaged streamwise velocity component (U_x/U_∞) in the wake of the cylinder (centerline in the x - y plane) for different mesh variants.....	28
Figure 21: Normalized time- and spanwise-averaged streamwise velocity component (U_x/U_∞) at three different locations in the wake of the cylinder in the x - y plane for different mesh variants.	28
Figure 22: Normalized time- and spanwise-averaged cross-flow velocity component (U_y/U_∞) at three different locations in the wake of the cylinder in the x - y plane for different mesh variants.	29
Figure 23: Absolute value of the time- and spanwise-averaged skin friction coefficient (C_f) on the cylinder surface for different mesh variants.	29
Figure 24: Comparison of the time- and spanwise-averaged streamwise velocity component (U_x/U_∞) in the wake of the cylinder (centerline in the x - y plane) with experimental data from Parnaudeau et al. (2008), Ong and Wallace (1996) and Lourenco and Shih (1993) data taken from Kravchenko and Moin (2000).	31

Figure 25: Comparison of the time- and spanwise-averaged cross-flow velocity component (U_y/U_∞) at three different locations in the wake of the cylinder in the x - y plane with experimental data from Parnaudeau et al. (2008) and Lourenco and Shih (1993).	32
Figure 26: Comparison of the time- and spanwise-averaged streamwise velocity component (U_x/U_∞) at three different locations in the wake of the cylinder in the x - y plane ($x/D = 1.06, 1.54, 2.02$) with experimental measurements by Parnaudeau et al. (2008) and Lourenco and Shih (1993).	32
Figure 27: Comparison of the pressure coefficient (C_p) on the cylinder surface with experimental measurements by Norberg and Sunden (1987) and Ma et al. (2000).	33
Figure 28: Comparison of the absolute value of the skin friction coefficient (C_f) on the cylinder surface with experimental data from Son and Hanratty (1969) at $Re = 5000$.	33
Figure 29: Power spectra of the streamwise velocity fluctuations measured at different locations in the wake of the cylinder.	34
Figure 30: Power spectra of the cross-flow velocity fluctuations measured at different locations in the wake of the cylinder.	34
Figure 31: Comparison of normalized cross-flow vibration amplitudes obtained by the present simulations compared with experimental measurements by Assi, Bearman and Meneghini (2010).	36
Figure 32: Time series of lift coefficient and cross-flow displacement (a) and drag coefficient (b) for $Ur 4$.	37
Figure 33: Time series of lift coefficient and cross-flow displacement (a) and drag coefficient (b) for $Ur 5$.	37
Figure 34: Time series of lift coefficient and cross-flow displacement (a) and drag coefficient (b) for $Ur 7$.	38
Figure 35: Normalized power spectral density of lift (a) and drag (b) coefficients for $Ur 4$.	38
Figure 36: Normalized power spectral density of lift (a) and drag (b) coefficients for $Ur 5$.	39
Figure 37: Normalized power spectral density of lift (a) and drag (b) coefficients for $Ur 7$.	39
Figure 38: Iso-surface of pressure coefficient ($C_p = -0.25$) colored by spanwise vorticity for $Ur4$ at $tU/D = 130$.	40
Figure 39: Iso-surface of Q-criterion ($Q = 1$) colored by spanwise vorticity for $Ur4$ at $tU/D = 130$.	40
Figure 40: Iso-surface of pressure coefficient ($C_p = -0.25$) colored by spanwise vorticity for $Ur 5$ at $tU/D = 140$.	40
Figure 41: Iso-surface of Q-criterion ($Q = 1$) colored by spanwise vorticity for $Ur 5$ at $tU/D = 140$.	40
Figure 42: Iso-surface of pressure coefficient ($C_p = -0.2$) colored by spanwise vorticity for $Ur 5$ at $tU/D = 19.6$.	41
Figure 43: Iso-surface of pressure coefficient ($C_p = -0.1$) colored by spanwise vorticity for $Ur 7$ at $tU/D = 160$.	41
Figure 44: Iso-surface of Q-criterion ($Q = 1$) colored by spanwise vorticity for $Ur 7$ at $tU/D = 160$.	41
Figure 45: Map of vortex shedding modes from Morse and Williamson (2009) at $Re = 4000$ with superposed results from the present study.	42
Figure 46: Spanwise correlation coefficient distribution $R(z)$ in the wake of the cylinder for different streamwise locations (x) and different reduced velocities (Ur); (a, d, g, j) $Ur 4$; (b, e, h, k) $Ur 5$; (c, f, i, l) $Ur 7$; (a, b, c) $x = 1$; (d, e, f) $x = 2$; (g, h, i) $x = 4$; (j, k, l) $x = 8$.	44
Figure 47: Iso-surface of Q-criterion colored by pressure for $Ur 4$ at $tUD = 100$: (a,b) $Q = 10$; (c) $Q = 3$.	45
Figure 48: Iso-surface of Q-criterion colored by pressure for $Ur 5$ at $tUD = 40$: (a,b) $Q = 10$; (c) $Q = 3$.	46

Figure 49: Iso-surface of Q-criterion colored by pressure for $Ur 7$ at $tUD = 160$: (a,b) $Q = 10$; (c) $Q = 3$	47
Figure 50: Schematic of the data sampling planes locations in the computational domain, (a) XZ-planes, (b) XY-plane.....	49
Figure 51: The mean value of E_{ortho} of the first ten most energetic evaluated for POD analysis with different sampling time intervals.	50
Figure 52: Energy and accumulated energy of POD modes on XY plane; (a) $Ur 4$; (b) $Ur 5$; (c) $Ur 7$	52
Figure 53: Energy contribution of the first 20 POD modes on XY plane; (a) $Ur 4$; (b) $Ur 5$; (c) $Ur 7$	52
Figure 54: Spatial structure of two leading POD modes: (a, b) $Ur 4$; (c, d) $Ur 5$; (e, f) $Ur 7$	53
Figure 55: second super harmonic shedding POD modes: (a,b) $Ur 4$; (c,d) $Ur 5$; (e,f) $Ur 7$; (a) mode 7; (b) mode 8; (c) mode 5; (d) mode 6; (e) mode 3; (f) mode 4.....	54
Figure 56: Time coefficient and power spectra for harmonic mode pairs on the XY plane for $Ur 4$: (a) first harmonic mode pair; (b) second harmonic mode pair.	55
Figure 57: Phase portraits of the time coefficients for the first two most energetic POD modes on the XY plane for; $Ur 4$ (a); $Ur 5$ (b); $Ur 7$ (c).	55
Figure 58: Phase portraits of the time coefficients for the second super harmonic shedding POD modes on the XY plane for; $Ur 4$ (a); $Ur 5$ (b); $Ur 7$ (c).	56
Figure 59: Time coefficient and power spectra for harmonic mode pair on XY-plane for $Ur 5$: (a) first harmonic mode pair; (b) second harmonic mode pair.	56
Figure 60: Time coefficients and power spectra for harmonic mode pair on XY-plane for $Ur 7$: (a) first harmonic mode pair; (b) second harmonic mode pair.	57
Figure 61: $\Phi 3$ u-component of the POD modes at different x locations for $Ur 4$: (a) mode 1; (b) mode 2; (c) mode 3; (d) mode 4.	59
Figure 62: $\Phi 3$ u-component of the POD modes at different x locations for $Ur 4$: (a) mode 5; (b) mode 6; (c) mode 7; (d) mode 8.	60
Figure 63: $\Phi 3$ v-component of the POD modes at different x locations for $Ur 4$: (a) mode 1; (b) mode 2; (c) mode 3; (d) mode 4.	61
Figure 64: $\Phi 3$ v-component of the POD modes at different x locations for $Ur 4$: (a) mode 5; (b) mode 6; (c) mode 7; (d) mode 8.	62
Figure 65: $\Phi 3$ w-component of the POD modes at different x locations for $Ur 4$: (a) mode 1; (b) mode 2; (c) mode 3; (d) mode 4.	63
Figure 66: $\Phi 3$ w-component of the POD modes at different x locations for $Ur 4$: (a) mode 5; (b) mode 6; (c) mode 7; (d) mode 8.	64
Figure 67: Energy and accumulated energy of POD modes for $Ur 4$ on YZ planes: (a) $x = 0.5D$; (b) $x = 1D$; (c) $x = 2D$; (d) $x = 4D$; (e) $x = 6D$; (f) $x = 8D$	65
Figure 68: Energy contribution of the first 20 POD modes for $Ur 4$ on YZ planes: (a) $x = 0.5D$; (b) $x = 1D$; (c) $x = 2D$; (d) $x = 4D$; (e) $x = 6D$; (f) $x = 8D$	66
Figure 69: $\Phi 3$ u-component of the POD modes at different x locations for $Ur 5$: (a) mode 1; (b) mode 2; (c) mode 3; (d) mode 4.	67
Figure 70: $\Phi 3$ u-component of the POD modes at different x locations for $Ur 5$: (a) mode 5; (b) mode 6; (c) mode 7; (d) mode 8.	68

Figure 71: Φ_3 v-component of the POD modes at different x locations for Ur 5: (a) mode1; (b) mode2; (c) mode3; (d) mode4.	69
Figure 72: Φ_3 v-component of the POD modes at different x locations for Ur 5: (a) mode 5; (b) mode 6; (c) mode 7; (d) mode 8.	70
Figure 73: Φ_3 w-component of the POD modes at different x locations for Ur 5: (a) mode 1; (b) mode 2; (c) mode 3; (d) mode 4.	71
Figure 74: Φ_3 w-component of the POD modes at different x locations for Ur 5: (a) mode 5; (b) mode 6; (c) mode 7; (d) mode 8.	72
Figure 75: Energy and accumulated energy of POD modes for Ur 5 on YZ planes: (a) $x = 0.5D$; (b) $x = 1D$; (c) $x = 2D$; (d) $x = 4D$; (e) $x = 6D$; (f) $x = 8D$	73
Figure 76: Energy contribution of the first 20 POD modes for Ur 5 on YZ planes: (a) $x = 0.5D$; (b) $x = 1D$; (c) $x = 2D$; (d) $x = 4D$; (e) $x = 6D$; (f) $x = 8D$	74
Figure 77: Φ_3 u-component of the POD modes at different x locations for Ur 7: (a) mode 1; (b) mode 2; (c) mode 3; (d) mode 4.	76
Figure 78: Φ_3 u-component of the POD modes at different x locations for Ur 7: (a) mode 5; (b) mode 6; (c) mode 7; (d) mode 8.	77
Figure 79: Φ_3 v-component of the POD modes at different x locations for Ur 7: (a) mode 1; (b) mode 2; (c) mode 3; (d) mode 4.	78
Figure 80: Φ_3 v-component of the POD modes at different x locations for Ur 7: (a) mode 5; (b) mode 6; (c) mode 7; (d) mode 8.	79
Figure 81: Φ_3 w-component of the POD modes at different x locations for Ur 7: (a) mode 1; (b) mode 2; (c) mode 3; (d) mode 4.	80
Figure 82: Φ_3 w-component of the POD modes at different x locations for Ur 7: (a) mode 5; (b) mode 6; (c) mode 7; (d) mode 8.	81
Figure 83: Energy and accumulated energy of POD modes for Ur 7 on YZ planes: (a) $x = 0.5D$; (b) $x = 1D$; (c) $x = 2D$; (d) $x = 4D$; (e) $x = 6D$; (f) $x = 8D$	82
Figure 84: Energy contribution of the first 20 POD modes for Ur 7 on YZ planes: (a) $x = 0.5D$; (b) $x = 1D$; (c) $x = 2D$; (d) $x = 4D$; (e) $x = 6D$; (f) $x = 8D$	83

List of Tables

Table 1: Regimes of flow around a smooth, circular cylinder in steady current. (Sumer and Fredsøe 2006, 2)....	8
Table 2: Mesh density sensitivity study	30
Table 3: Time step sensitivity study.....	30
Table 4: Summary of root-mean-square and maximum cross-flow displacement obtained in present simulations.	42

Nomenclature

C_d	Drag coefficient
C_L	Lift coefficient
U_r	Reduced velocity
f_n	Natural frequency of the cylinder submerged in a fluid.
f_{osc}	Frequency of the oscillation of the cylinder
f_{st}	Strouhal frequency
f_{vac}	Natural frequency of the cylinder in a vacuum.
f_{vs}	Vortex shedding frequency
f_{vs}	frequency of vortex shedding.
m^*	Mass ratio
m_a	Added mass
A	Surface area projected in the direction of the flow
C_f	Skin friction factor
C_p	Pressure coefficient
D	Diameter of the cylinder
I	Identity tensor
L	Spanwise dimension of cylinder
Re	Reynolds number
n	Unity vector normal to the cylinder surface
Γ	Surface area of cylinder
ζ	Damping ratio
ρ	Density of fluid
τ	Skin shear stress

Acronyms

DoF	Degree of Freedom
CFD	Computational Fluid Dynamics
VIV	Vortex-Induced Vibration
SGS	Sub Grid Scale
LES	Large Eddy Simulation
WALE	Wall-adapting Local Eddy-viscosity
WIV	Wake Induced Vibrations
SVD	Singular Value Decomposition
POD	Proper Orthogonal Decomposition
RMS	Root Mean Square
PSD	Power Spectral Density

1 Introduction

1.1 Background and Motivation

A cylinder is a shape that can be found in all kinds of structural cross-sections ranging from support towers, pipelines, cables, chimneys to floaters. Cylindrical structures can be affected by Vortex-Induced Vibrations (VIV) which results in additional loads like drag amplification and cyclic loading that can cause fatigue. The study of VIV is of great interest from the perspective of fluid dynamics. In offshore applications loads caused by VIV are a major challenge. Vortex shedding and therefore VIV occurs for cylinders exposed to a steady flow when the Reynolds number ($Re = UD/\nu$ where U is the free stream flow velocity, D is the cylinder diameter and ν is the kinematic viscosity of the fluid) is larger than 40.

The VIV behavior depends on the flow velocity, Reynolds number (Re), damping on the cylinder and the mass ratio. The mass ratio m^* is the mass of the cylinder divided by the mass of the displaced fluid. Commonly used for the classification of systems is also the mass-damping parameter which is the product of m^* and the damping ratio of the system.

Systems undergoing VIV can be classified in the definitions of low and high mass ratios. An example for a high mass ratio system is an industrial chimney exposed to wind, an example for a low mass ratio is an offshore oil riser. Research of VIV for spar type floaters is a field of great interest due to the big potential of floating wind turbines with a spar type floater. For bottom fixed offshore wind turbines VIV loads are not of such a relevance due to the solid foundation which restricts horizontal movements.

Like all cylindrical objects spar type floaters can be influenced by VIV. This can happen especially when the floating wind turbine is exposed to a high velocity steady current, which can occur on sites with high sea currents or while towing the structure. Due to the tall structure of a wind turbine the floater must handle big bending moments in relation to the buoyancy force. The bending is counteracted with a big draft. Therefore, spar type floaters for offshore wind turbines are slim compared to spar oil platforms which is resulting in a higher reduced velocity for the same flow velocity. It is desirable to better understand the flow for VIV scenarios at a low mass ratio. This thesis concentrates on the detailed flow behavior for low mass ratio structures. Numerical simulations are used to simulate the flow field around an elastically supported circular cylinder. The numerical simulation method is chosen since it offers several advantages over experimental investigations. The simulation allows to save a large data set for a detailed analysis of the flow field, which would be more complicated for a physical experiment since the measuring probes would interact with the flow. Further advantages are the lower cost of numerical simulations, compared to experimental investigations.

1.2 Problem Definition and Objectives of the Thesis

The geometry for the simulation is a circular cylinder which is flexibly supported. The cylinder is set to move freely in 1 degree of freedom (DoF) in the cross-flow direction. The simulations are performed using the open source finite volume method code OpenFOAM. OpenFOAM is a Computational Fluid Dynamics code which is used in commercial and academic applications.

Research objective 1: Parametric study of the flow characteristics and vibration responses of an elastically supported cylinder exposed to a steady current at $Re = 3900$.

Research objective 2: Investigation of wake dynamics behind a cylinder undergoing VIV via Proper Orthogonal Decomposition.

1.3 Outline of the Thesis

The structure of the thesis is the following

Chapter 2. Flow around a Cylinder:

A review of fluid dynamics around circular cylinders is given, which includes the vortex shedding mechanism and the behavior of vortex-induced vibrations.

Chapter 3. Computational Fluid Dynamics (CFD):

A review of numerical methods used in the present study is given, including an introduction to the OpenFOAM toolbox and mesh generation procedures.

Chapter 4. Simulation of Stationary Cylinder:

A stationary cylinder is simulated with different mesh resolutions for the purpose of a mesh convergence study. For the validation of the simulation, results are compared to experimental data.

Chapter 5. Simulations of self-excited Cylinder Vibrations:

The flow structure of a single cylinder which is undergoing VIV is analyzed. Flow parameters are compared to results from experimental investigations. Proper Orthogonal decomposition is used for the analyses of the wake structure.

Chapter 6. Conclusion:

A conclusion of the finding from the simulations is given.

Chapter 7. Future Work:

Two fields of Future work are presented, the simulation of VIV mitigation designs and the simulation of a tandem arrangement of two cylinders for the analyses of Wake induced vibration.

1.4 Previous Work

The phenomenon of vortex shedding has been a core interest of fluid mechanics studies for many years. In the 20th century Theodore von Kármán was the first to describe the Kármán vortex street. He derived the conditions under which the oscillation pattern occurs. Feng (1968) performed an experiment of a cylinder in air (high m^*) and was the first to perform detailed measurements of vortex induced vibration and discovered the lock-in phenomenon. Sumer and Fredsøe (2006) give an extensive description of flow around circular cylinders. Numerous studies show the effects of physical parameters like m^* and DoF on the VIV behavior. Jauvtis and Williamson (2004) showed that for a cylinder free to respond in 2DoF the mass ratio has a significant effect on the vortex shedding dynamics. A new vortex shedding mode named a 2T mode occurring for m^* lower than 6 was observed. Assi et al. (2006) performed experiments for cylinders vibrating in 1DoF (cross-flow direction) and a m^* of 0.96 and 0.90, they reported maximum displacements of approximately 2 times the cylinder diameter ($2D$). Govardhan and Williamson (2002) found a critical $m^* = 0.54$ based on their observations where the cross-flow amplitude response for experiments with $m^* \leq 0.54$ was increased dramatically. Since VIV can result in drag amplification and fatigue, the mitigation of VIV is of great interest. For some systems, changing the eigenfrequency of the cylinder by mass redistribution can be used for the mitigation of VIV. However, based on the results of Baz and Kim (1993), Gabbai and Benaroya (2005) have found that for structures vibrating in water, it is not possible to completely suppress the vibration only by mass redistribution alone. For a low m^* systems, the added mass has the dominant effect on the system so that changes in the mass distribution of the cylinder have no significant effect on the VIV response. Therefore, other means for VIV mitigation need to be applied. Most studies on vortex suppression methods have been conducted for high m^* structures since these ratios are more common for coated pipelines and chimneys. The most common VIV mitigation approach is to attach a set of helix strakes to the cylinder. Normally two or three rows of strakes are used. The strakes change the separation angle which is disrupting the spanwise correlation of the vortex formation. Important parameters of a helical strake are the heights of the strake and the pitch of the strake. The pitch is defined as the distance it takes for a single helical strake to make a complete rotation around the cylinder. Quen et al. (2018) has shown that the strake height should be larger than the boundary layer thickness in order to effectively reduce the VIV and that a change in the strake pitch does not significantly suppress the VIV, but it can delay the occurrence of lock-in of the cylinder. Furthermore Quen et al. (2018) concluded that a pitch of $5D$ is ineffective for low m^* cylinders and pitches of 10 to 15 D are recommended for low mass ratio structures ($m^* = 1.17$). We know from Bearman and Branković (2004) that passive suppression devices that work well for structures with high mass-damping, have only a limited effect on structures with low mass-damping. This indicates that different mitigation techniques should be used depending on the mass-damping of the system. Assi and Crespi (2019) conducted laboratory investigations on a low mass-ratio cylinder ($m^* = 0.6$) using a new helical strake design where the strakes are separated in an arrangement of blades and the blades are twisted. This design was able to reduce the drag coefficient

compared to a conventional strake by 15%, with the same cross-flow vibration suppression as a conventional strake. Several other designs for VIV mitigation have been investigated. Cicolin and Assi (2017) conducted extensive research on VIV reduction with different forms of passive flexible structures and managed to reduce the lift coefficient but with an increase in the drag coefficient. Assi et al. (2018) tested an active suppression system that uses small rotating cylinders around the main cylinder and found a reduction in the drag coefficient while suppressing the vortex shedding. To further develop VIV mitigation strategies comprehensive knowledge of the flow structure around a cylinder undergoing VIV is of great interest. For a detailed analysis of the coherent structure in turbulent flow the Proper Orthogonal Decomposition (POD) is a commonly used algorithm that was first introduced by Lumley (1967). Samani (2014) used POD for a detailed analysis the coherent structure of turbulent flow around a square cylinder and demonstrated the advantages of POD for the study of turbulent flow. Feng et al. (2011) used POD to analyse the vortex dynamics of a circular cylinder under synthetic jet control and described how the vortex shedding changes between symmetric and antisymmetric modes under the influence of the jet control. Riches et al. (2018) have used POD on experimental data to analyze the wake-dynamics of a low mass-ratio ($m^* = 5.3$) circular cylinder. They have found that for the initial branch 6 POD modes are required to capture the salient aspects of the flow while in the upper branch 7 modes are required. The increase in computational performance in the last years has made numerical simulations faster and cheaper than ever, three-dimensional computational simulations of the VIV phenomenon can be used at a relatively low cost. Sidebottom et al. (2015) conducted large eddy simulations (LES) on a stationary cylinder assessing the influence of the parameters discretization schemes, subgrid scale (SGS) models and the wall models. They found that the central discretization scheme is more accurate than the upwind scheme and that the SGS models affect the flow-field, but only with small differences between the results from the Smagorinsky model and the one equation eddy viscosity model. Furthermore, they found that the wall model has a significant effect on the flow up to $10 D$ downstream of the cylinder but the effect of the wall model was difficult to quantify. Sarwar and Mellibovsky (2020) have conducted a direct numerical simulation for flows around a circular cylinder and have shown that while Kármán vortices remain predominantly two-dimensional, streamwise vortical structures appearing along the braids connecting consecutive vortices are mainly responsible for rendering the flow three-dimensional.

2 Flow around Circular Cylinders

2.1 Turbulence

Turbulent flow is characterized by irregular motions of the fluid particles, in contrast to laminar flow which is characterized by smooth and steady motions of the fluid particles. Turbulent flow is more complex due to random mixing in the flow field. The Reynolds number can be used to predict the onset of turbulent flow. The Reynolds number is defined as:

$$Re = \frac{U_{\infty} D}{\nu} \quad (2-1)$$

Where U_{∞} is the free stream velocity, D is the characteristic length (in this case the diameter of the cylinder) and ν is the kinematic viscosity.

Turbulent flow is characterized by chaotic fluctuations in the velocity and pressure. According to Tennekes and Lumley (1972) and Ecke (2005) the characteristics of turbulent flow are:

Turbulent flow is irregular, due to the randomness of turbulent flow, statistic methods are needed to analyze the flow. (Tennekes and Lumley 1972)

Due to the high diffusivity, turbulent flow has rapid mixing which is increasing the rate of momentum, mass and heat transfer. (Ecke 2005)

Turbulent flow has a large Reynolds number. The viscous effects in turbulent flow are dominated by the inertia forces. (Ecke 2005)

Turbulent flow is three dimensional. (Tennekes and Lumley 1972)

Turbulent flow is dissipating energy. In the smallest eddies the kinetic energy is dissipated by viscosity into heat. (Ecke 2005)

Turbulent flow has random velocity fluctuations over time and location. (Ecke 2005)

The geometry of the flow has a significant impact on large-scale eddies. The boundary conditions control the flow and mixing. The small-scale eddies can be predicted by the rate of energy transfer from the large-scale to the small-scale. (Tennekes and Lumley 1972)

Turbulent flow is rotational and characterized by a fluctuating vorticity. Vorticity represents the rotational effects of the flow. (Tennekes and Lumley 1972)

2.2 Boundary Layer

In a viscous flow a boundary layer is forming near the surface of objects. Due to the viscosity the skin friction causes the flow velocity on the surface to be zero, the so-called no-slip condition. The fluid layer that sticks to the solid surface in a no-slip condition slows the neighboring fluid layer, which then slows the next layer, and so on, due to the viscous force between the fluid layers. Boundary layers can be classified into turbulent and laminar boundary layers. The development of a boundary layer for laminar,

transitional and turbulent regimes is shown in Figure 1. The fluid particles are subjected to a no-slip condition when they are close to the surface, and their velocity becomes zero, resulting in the creation of a viscous sublayer. Shear stress develops in the thin fluid layer near the plate as a result of this. The flow becomes unstable after a certain distance, and eddies form in the shear layer. (Çengel and Cimbala 2006)

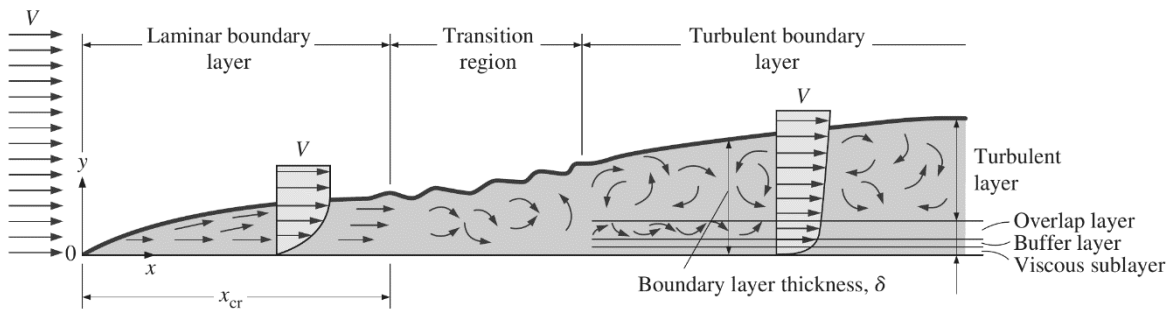


Figure 1: The development of the boundary layer for flow over a flat plate, and the different flow regimes. Not to scale. (Çengel and Cimbala 2006, 579)

2.2.1 Flow Separation

Separation of the boundary layer from the surfaces of bluff bodies can occur due to a strong adverse pressure gradient. The velocity along the boundary layer begins to decrease, the thickness of the boundary layer increases, and the flow begins to reverse. The boundary layer cannot follow the surface any longer and detaches. A shear layer is formed, and a recirculation bubble occurs (Sumer and Fredsøe 2006). Figure 2 shows the shear layer separating from the surface of a cylinder. The shear layer is characterized by a high vorticity.

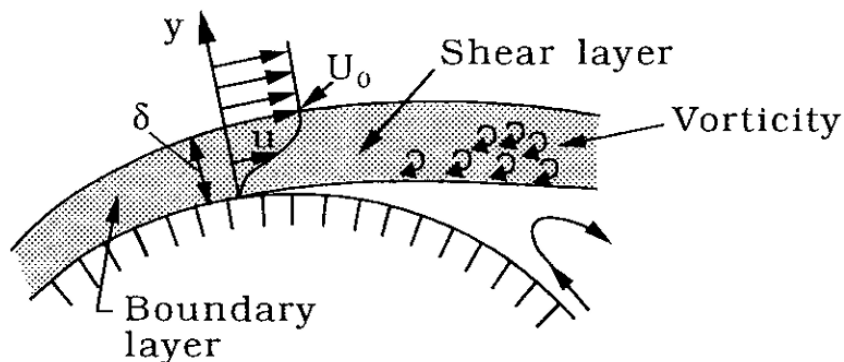


Figure 2: Shear layer separation (Sumer and Fredsøe 2006, 7).

2.3 Flow Regimes Around Circular Cylinder

The loads on a circular cylinder in a steady flow heavily depend on the occurrence of vortex shedding. The Reynolds number is governing the flow around a cylinder. The vortex formation takes place for flows with $Re > 40$. The flow field around the cylinder can be categorized in different regimes, which

are shown in Figure 3. The flow approaching the cylinder needs to move around the cylinder which results in a flow acceleration on the sides of the cylinder. In front of the cylinder the flow decelerates due to the static pressure. Behind the cylinder is the wake where the average flow velocity is lower than the freestream velocity. The wake is the zone where the vortices form.

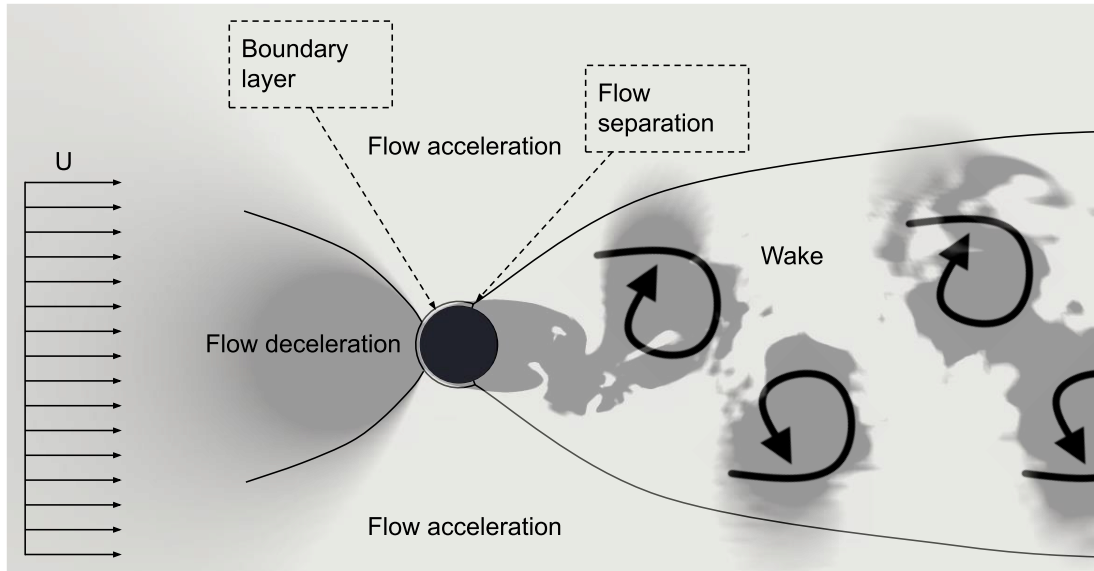


Figure 3: Flow regions around a circular cylinder

2.4 Mechanism of Vortex Shedding

As mentioned in section 2.2, when $Re > 40$ the boundary layer will separate, and a shear layer is formed, this shear layer is the source for the formation of vortices. Figure 4 shows the vortex formation sequence. The boundary layer has a high vorticity, this vorticity is transferred to the shear layer and causes the shear layer to roll up to a vortex (vortex A). A vortex of opposite rotation is formed on the other side of the cylinder (Vortex B). The formation of vortices is unstable and therefore one will grow larger and stronger (Vortex A in Figure 4 (a)). Vortex A eventually becomes strong enough to draw vortex B across the wake. Vortex A has clockwise vorticity and vortex B has counterclockwise vorticity. The counterclockwise vorticity of vortex B is coming into contact with the clockwise shear layer of vortex A which cuts the supply of vorticity for vortex A. Resulting in vortex A being shed, vortex A is now free from the cylinder. A new vortex (Vortex C) with clockwise vorticity will form from the shear layer that is separated from vortex A. Vortex B is now the biggest vortex that is still connected to the shear layer from the cylinder, it will grow bigger until vortex C gets drawn across the wake and vortex B is shed. This process will be repeated on alternating sides of the cylinder.

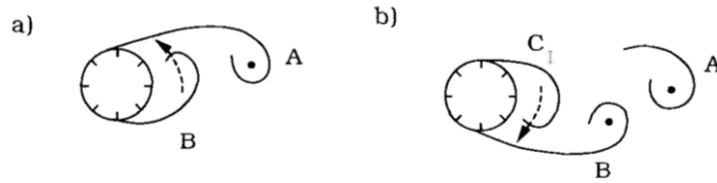


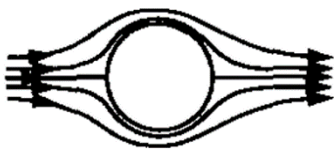
Figure 4: Vortex shedding (Sumer and Fredsøe 2006, 8)

With an increasing Re the flow around a circular cylinder changes as the flow becomes more turbulent. The regimes for a smooth circular cylinder at increasing Re are shown in Table 1.

For a flow around a cylinder at a $Re < 40$ no vortex shedding occurs, and the flow field is steady and symmetric. For a flow in the Re range of $40 < Re < 200$. The vortices become unstable and start to detach from the cylinder. The vortices are laminar. When the Re is increased to $Re > 200$ the wake starts to transition to turbulent flow. For a $Re > 300$ the wake is completely turbulent. In the subcritical regime $300 < Re < 3 \times 10^5$ the wake is completely turbulent, but the boundary layer separation is still laminar. In the critical regime of $3 \times 10^5 < Re < 3.5 \times 10^5$ the boundary layer is still laminar. However, on one side of the cylinder the boundary layer separation point becomes turbulent. So, one separation point is turbulent while the other is still laminar, this is resulting in a non-zero mean lift. In the supercritical regime $3.5 \times 10^5 < Re < 1.5 \times 10^6$ the boundary layer is partly turbulent. The transition from laminar to turbulent in the boundary layer occurs somewhere between the stagnation point and the separation point. The upper transitional regime $1.5 \times 10^6 < Re < 4 \times 10^6$ the boundary layer is completely turbulent in one side of the cylinder. For $1.5 \times 10^6 < Re$ the transcritical regime is reached and the boundary layer is completely turbulent on both sides. (Sumer and Fredsøe 2006)

Table 1: Regimes of flow around a smooth, circular cylinder in steady current. (Sumer and Fredsøe 2006, 2)

(a)



No separation.
Creeping flow

$Re < 5$

(b)



A fixed pair of
symmetric vortices

$5 < Re < 40$

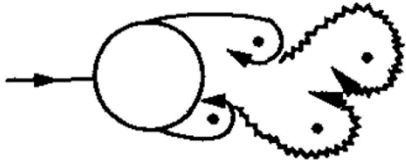
(c)



Laminar vortex street

$$40 < Re < 200$$

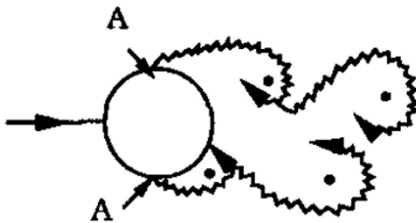
(d)



Transition to
turbulence in the
wake

$$200 < Re < 300$$

(e)

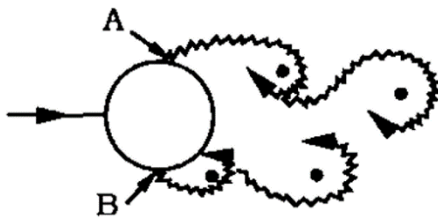


Wake completely
turbulent.
A: Laminar boundary
layer separation

$$300 < Re < 3 \times 10^5$$

Subcritical

(f)

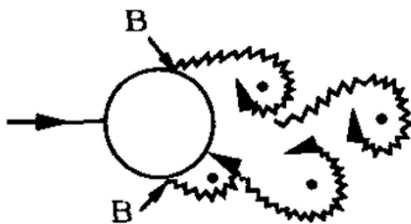


A: Laminar boundary
layer separation
B: Turbulent
boundary layer
separation

$$3 \times 10^5 < Re < 3.5 \times 10^5$$

Critical (Lower transition)

(g)



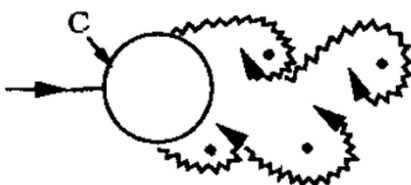
B: Turbulent
boundary layer
separation; the
boundary layer partly
laminar partly
turbulent

$$3.5 \times 10^5 < Re$$

$$< 1.5 \times 10^6$$

Supercritical

(h)

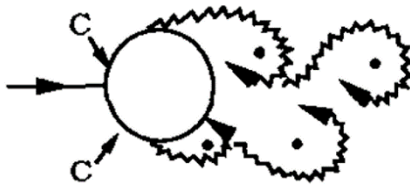


C: Boundary layer
completely turbulent
at one side

$$1.5 \times 10^6 < Re < 4 \times 10^6$$

Upper transition

(i)



C: Boundary layer
completely turbulent
at two sides

$4 \times 10^6 < Re$
Transcritical

2.4.1 Vortex Shedding Frequency

The vortex shedding frequency is characterized by the dimensionless Strouhal number. The Strouhal number is a function of Re . The vortex shedding frequency can be normalized by the cylinder diameter D and the free stream flow velocity U_∞

$$St = St(Re) \quad (2-2)$$

where

$$St = \frac{f_v D}{U_\infty} \quad (2-3)$$

and f_v is the frequency of vortex shedding. The Strouhal number over Re for a smooth cylinder is shown in Figure 5. The shedding frequency changes drastically in the lower and upper transition regimes.

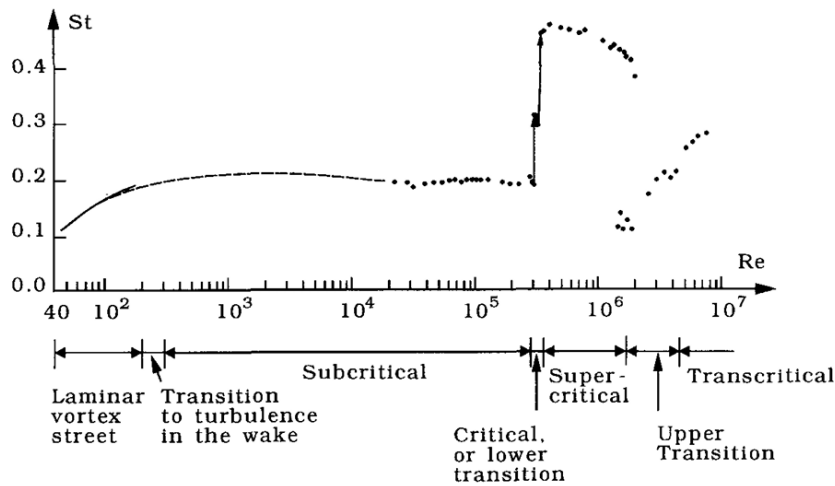


Figure 5: Strouhal number for smooth circular cylinder. Experimental data from: Solid curve: (C. Williamson 1989) Dashed curve (Roshko 1961). Dots: (Schewe 1983) Figure from (Sumer and Fredsøe 2006, 10)

2.5 Forces on a Circular Cylinder in a Steady Flow

The vortex shedding phenomenon has a significant impact on the forces acting on the cylinder. According to Sumer and Fredsøe (2006) the total force on a cylinder in a steady flow can be divided into the pressure and the viscous component, F_p and F_f , respectively. By integrating of the orthogonal

components of the pressure and viscous force, along the cylinder surface, the cross-flow and in-line force can be isolated, resulting in the mean drag force:

$$\overline{F_D} = \overline{F_{p\ x}} + \overline{F_{f\ x}} \quad (2-4)$$

and the lift force:

$$\overline{F_L} = \overline{F_{p\ y}} + \overline{F_{f\ y}} \quad (2-5)$$

The lift force F_L will be zero when the flow is symmetric for $Re < 40$, however, for flow scenarios of $Re > 40$ when vortex shedding occurs the lift force will be nonzero and will oscillate with the vortex shedding frequency. Due to equal vortex shedding on both sides of the cylinder the mean lift force $\overline{F_L}$ will be zero for most vortex shedding patterns, except for the critical regime for $3 \times 10^5 < Re < 3.5 \times 10^5$ where the asymmetric boundary layer results in a nonzero mean lift. The drag force F_D will oscillate around the mean value.

2.6 Vortex Shedding Patterns

Depending on the reduced velocity and displacement amplitude in cross-flow direction the vortex patterns in the wake may take different forms. Some relevant wake patterns defined by Williamson and Roshko (1988) and Morse and Williamson (2009) are listed below. The classification of the shedding pattern is defined by the number of vortices shed for each cycle of oscillation. Examples of the shedding patterns are shown in Figure 6.

2S: The 2 single pattern is defined by 2 single vortices. A single vortex is shed from each side of the cylinder

2P: The 2 pairs pattern is defined by 2 pairs of vortices. A pair of vortices is shed from each side of the cylinder

P+S: The pair and single pattern is defined by a single vortex in one side of the cylinder and a pair of 2 vortices being shed on the other side of the cylinder

2Po: In the 2 pairs overlap pattern the shedding pattern switches between 2S and 2P and the secondary vortex is significantly smaller than the primary vortex.

The vortex shedding patterns are dependent on the flow velocity and oscillation amplitude Figure 7 shows the shedding patterns found by Morse and Williamson (2009).

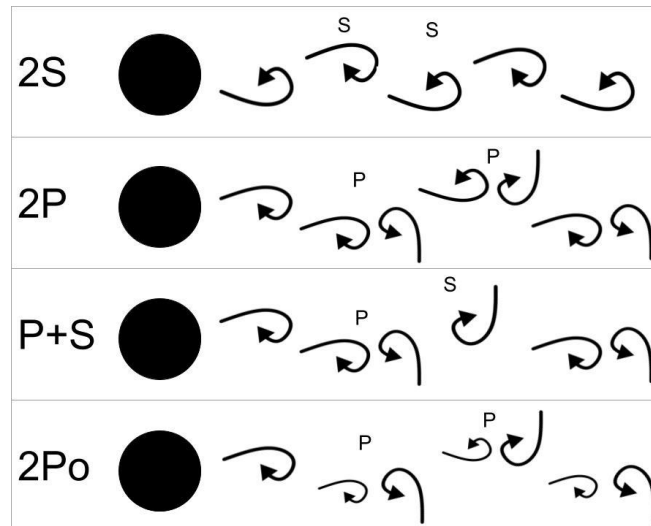


Figure 6: Vortex shedding patterns. (Williamson and Roshko 1988) and (Morse and Williamson 2009)

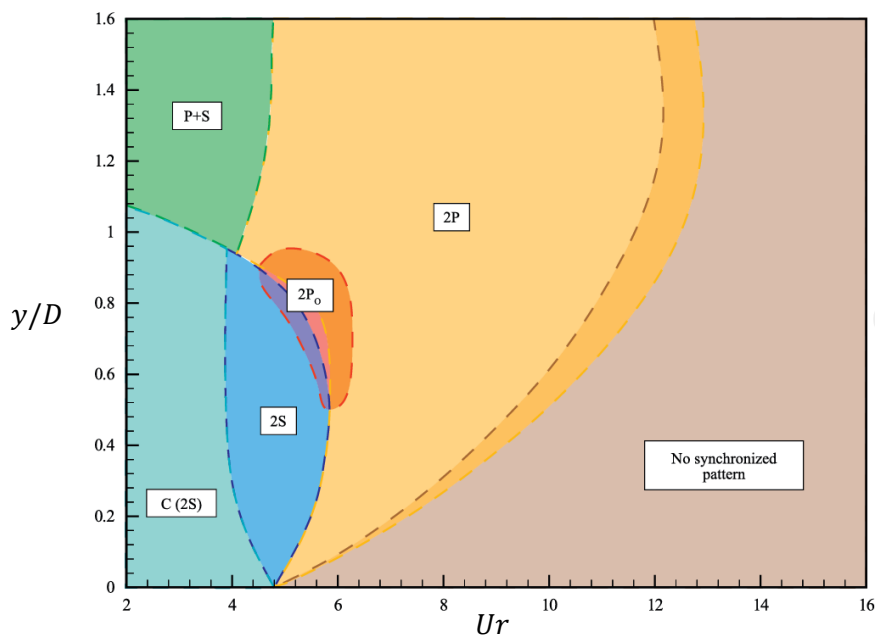


Figure 7: Map of vortex shedding patterns occurring for different combinations of y/D and Ur from Morse and Williamson (2009) at $Re = 4000$

2.7 Vortex Induced Vibration

For an elastically mounted cylinder which is exposed to a steady flow where vortex shedding occurs, the forces acting on the cylinder might result in vibrations of the cylinder. This phenomenon is called vortex induced vibration (VIV). It occurs due to the feedback between the vortex shedding and the cylinder motion. The VIV is influenced by different parameters. Different frequencies are defined for the description of the VIV phenomenon:

f_{osc} is the frequency of the oscillation of the cylinder.

f_{vs} is the frequency of vortex shedding.

f_{st} is the Strouhal frequency which is the frequency of vortex shedding for a cylinder at rest.

$f_{vac} = \frac{1}{2} \sqrt{\frac{k}{m}}$ is the natural frequency of the cylinder in a vacuum.

$f_n = \frac{1}{2} \sqrt{\frac{k}{m+m_a}}$ is the natural frequency of the cylinder submerged in a fluid.

2.7.1 Reduced Velocity

The distance that the flow travels pass the cylinder for one vibration cycle has an important influence on the cross-flow vibration amplitude, a quantity that is used to indicate this is the reduced velocity. The reduced velocity is the flow velocity normalized by the diameter of the cylinder and the natural frequency of the cylinder oscillation.

$$Ur = \frac{U}{f_n D} \quad (2-6)$$

2.7.2 Mass-ratio

The mass-ratio is the ratio between the mass of the cylinder and the mass of the displaced fluid.

$$m^* = \frac{m}{m_d} \quad (2-7)$$

This ratio indicates the importance of added mass and buoyancy effects on the cylinder. The mass-ratio has influence on the frequency response and the amplitude. Low mass-ratio systems have a large amplitude response for a wider Ur range than high mass-ratio systems, however the maximum response occurs on similar values of Ur for different mass-ratio (Sumer and Fredsøe 2006). For some studies of VIV the mass-damping is used as a parameter for the system classification. The mass-damping of a system is the mass-ratio multiplied by the damping ratio ($m^* \zeta$) (Khalak and Williamson 1999).

2.7.3 Added Mass

A vibrating cylinder submerged in a fluid is subject to additional forces due to the added mass (m_a). The Added or virtual mass is the inertia that is added to the cylinder due to the fluid that is move together with the cylinder. The force resulting from the added mass is acting against the movement of the cylinder. This is resulting in the equation of motion for a cylinder with 1 DoF in cross-flow expressed as:

$$m\ddot{y} + c\dot{y} + ky = F_y - m_a\ddot{y} \quad (2-8)$$

where m is the mass of the cylinder, y the displacement in cross flow direction and F_y is the force on the cylinder in cross flow direction.

2.7.4 Lock-in

The frequency lock-in of a cylinder exposed to a steady flow is described on the example of the experiment from Feng (1968). A cylinder that is elastically mounted and allows movement in the cross-flow direction is exposed to a steady air flow. The velocity of the flow is gradually increased. Frequencies f_{vs} , f_{osc} , vibration amplitude and the phase angle between the displacement and the lift force are measured. The results of this experiment are shown in Figure 8. For the region of the highest amplitude the vortex shedding frequency f_{vs} follows the natural frequency of the cylinder. This is the so-called lock-in range. In the lock-in range the three frequencies, natural frequency of the cylinder, frequency oscillation and frequency of vortex shedding are the same: $f_{vs} = f_{osc} = f_n$. Therefore, the lift force, which is dependent on the vortex shedding, and the cylinder motion are synchronized which results in a large amplitude of the vibration. When the flow increases more the vortex shedding frequency detaches from the natural frequency and the vibration amplitude drops significantly. There is a hysteresis effect which manifests in different amplitudes for the scenarios of an increased or decreased flow velocity. The experiment by Feng (1968) was performed on a system with a high mass-ratio. The effect of mass-ratio on the VIV response is further explained in the section 2.8. The sudden drop in the vibration amplitude, for the change from the upper to the lower branch, comes with a change of the vortex shedding pattern from 2S to 2P.

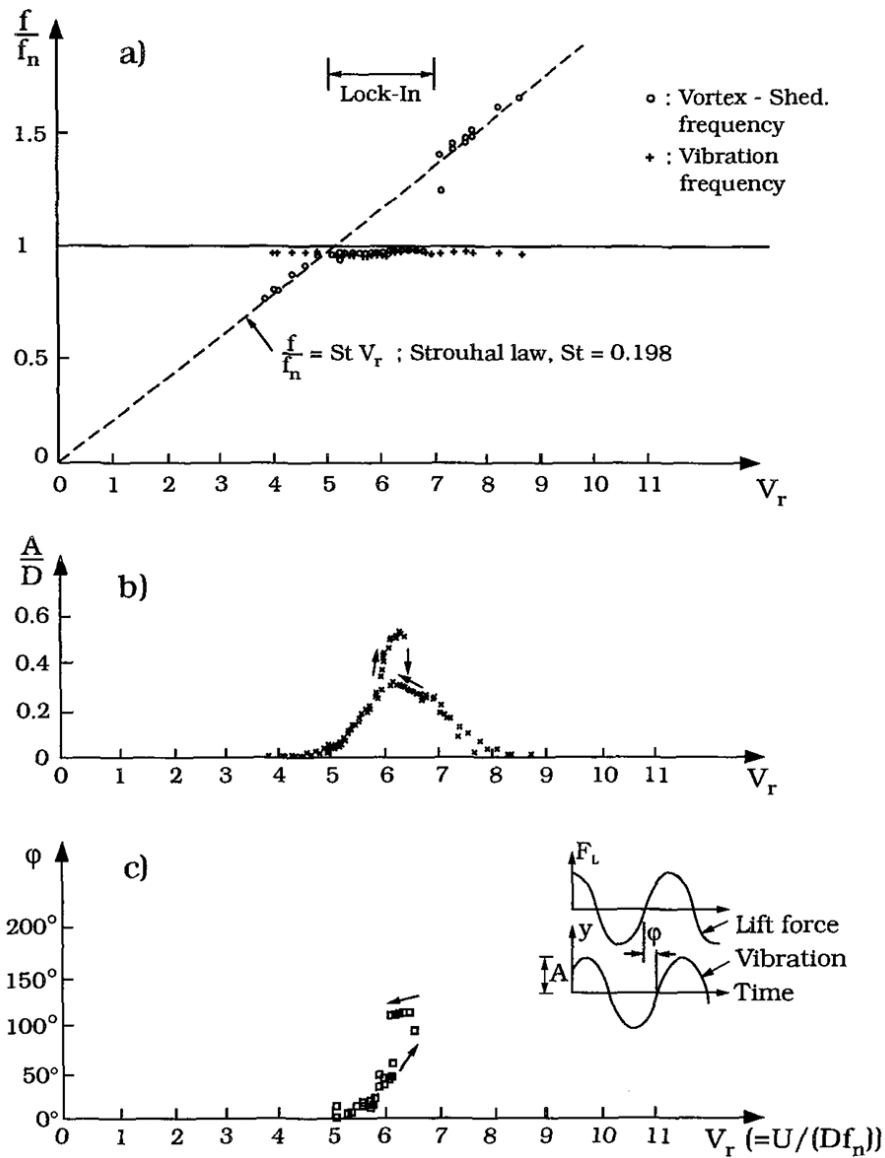


Figure 8: Cross-flow response of flexibly mounted cylinder in steady current (C. Feng 1968) (plot taken from (Sumer and Fredsøe 2006, 356))

For a system with low m^* , like it is common for a cylinder exposed to a water flow, the frequency response is different. Due to the effect of a change in the added mass f_n changes in the lock-in range. Figure 9 shows the frequency response for a high and low m^* system.

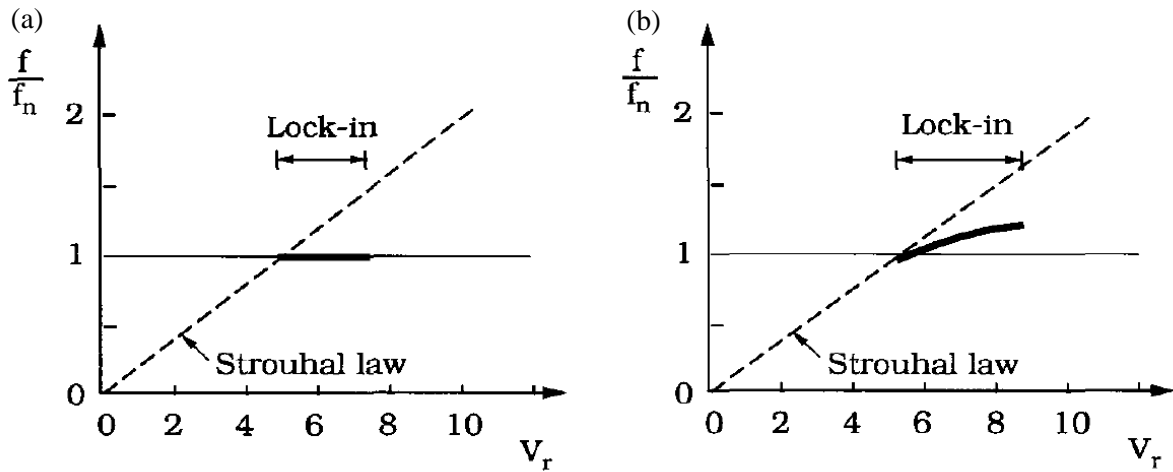


Figure 9: Schematic illustration of lock-in frequency for high (a) and low (b) mass-ratio (Sumer and Fredsøe 2006, 360).

2.8 Response Amplitude

The amplitude of the VIV in the lock-in range is dependent on Ur . The amplitude response is dependent on mass-damping. For high mass-damping there are two distinctive branches of the amplitude response, the initial and lower branch. Figure 10(a) shows the amplitude response for a high mass-damping system. When the vibration amplitude changes between the two branches there is a hysteresis effect. For high mass-damping systems, the maximum amplitude is reached in the initial branch. For low mass-damping systems, there is an additional branch, the upper branch, there is a hysteresis effect for the change between the three branches. Figure 10(b) shows the amplitude response for a low mass-damping system. In the upper branch the maximum vibration amplitude is reached, this maximum amplitude is higher than the maximum that can be reached in a high mass-damping system (Khalak and Williamson 1999).

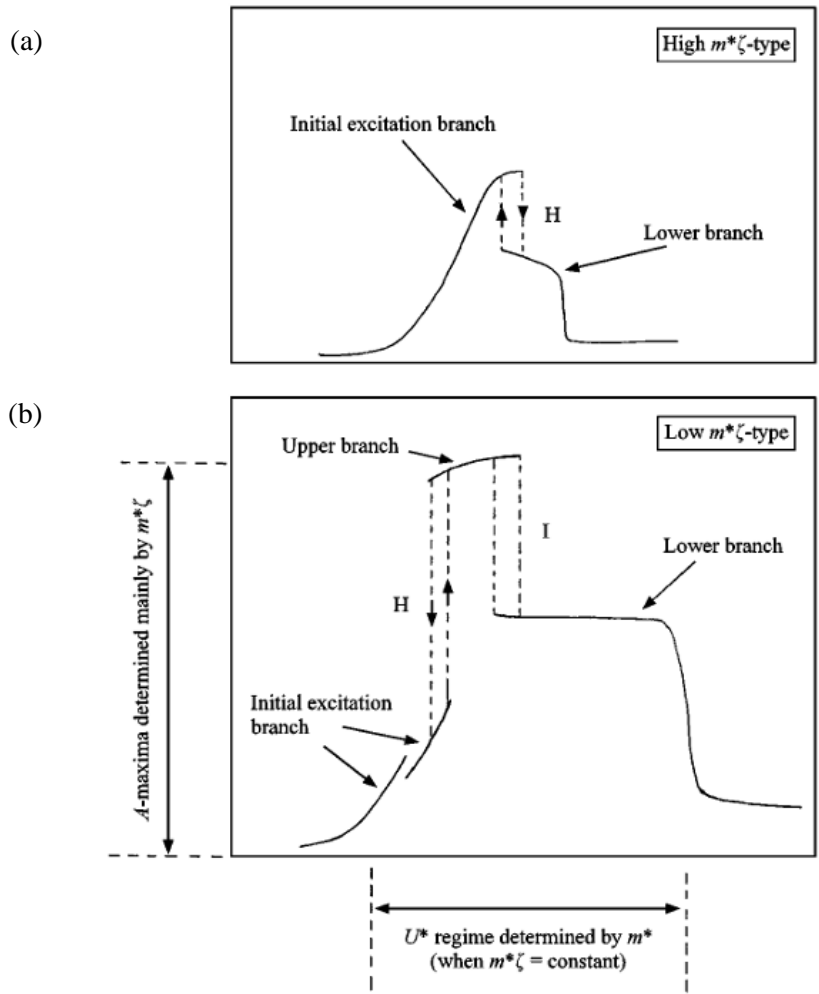


Figure 10: Amplitude response for low and high mass-damping systems (Vertical axes represent the vibration amplitude and the horizontal axes represent the reduced velocity) (Khalak and Williamson 1999, 822)

3 Computational Fluid Dynamics

This chapter presents the general concept of Computational Fluid Dynamics (CFD). CFD is a powerful tool that is commonly used in the industry and academia. CFD simulations can be a cost-effective alternative to experimental investigations.

3.1 Governing Equations

The governing equations of the present problem are the incompressible filtered Navier Stokes equations solved using Large Eddy Simulation (LES) methodology. Filtering out the turbulent eddies that are smaller than the filter. The filter width is set as the cube root of a computational grid volume which results in the equations (3-1) and (3-2) (Prsic, et al. 2014)

$$\frac{\partial \bar{u}_i}{\partial x_i} = 0 \quad (3-1)$$

$$\frac{\partial \bar{u}_i}{\partial t} + \frac{\partial (\bar{u}_i \bar{u}_j)}{\partial x_j} = -\frac{1}{\rho} \frac{\partial \bar{p}}{\partial x_i} + \nu \frac{\partial^2 \bar{u}_i}{\partial x_j^2} - \frac{\partial \tau_{ij}}{\partial x_j} \quad (3-2)$$

where $\bar{u}_i, i \in [1,2,3]$ is the filtered velocity, ρ is the density of the fluid, \bar{p} is the filtered pressure and τ_{ij} is the unresolved sub-grid stress. The sub-grid stress is given by equation.

$$\tau_{ij} = \overline{u_i u_j} - \bar{u}_i \bar{u}_j \quad (3-3)$$

where overbar denotes the filtering. In the present study the Wall-adapting Local Eddy-viscosity (WALE) sub-grid stress model (Nicoud and Ducros 1999) is selected to model the sub-grid stress. The sub-grid model is based on the squared velocity gradient tensor and it takes the shear stress and rotation tensor into consideration. The turbulent eddy viscosity ν_t is given by equation

$$\nu_t = (c_\omega \Delta)^2 \frac{(s_{ij}^d s_{ij}^d)^{3/2}}{(\bar{S}_{ij} \bar{S}_{ij})^{5/2} + (s_{ij}^d s_{ij}^d)^{5/4}} \quad (3-4)$$

where

$$\bar{S}_{ij} = \frac{1}{2} \left(\frac{\partial \bar{u}_i}{\partial x_j} + \frac{\partial \bar{u}_j}{\partial x_i} \right) \quad (3-5)$$

and

$$\varepsilon_{ij}^d = \bar{S}_{ik}\bar{S}_{kj} + \bar{\Omega}_{ik}\bar{\Omega}_{kj} - \frac{1}{3}\delta_{ij}[\bar{S}_{mn}\bar{S}_{mn} - \bar{\Omega}_{mn}\bar{\Omega}_{mn}] \quad (3-6)$$

In these equations, \bar{S}_{ij} is the strain rate tensor and $\bar{\Omega}_{ik}$ is the rotation rate tensor.

The present simulations consider a rigid cylinder that is elastically supported by a spring-damper system. The cylinder is free to move in cross-flow directions which can be modeled as a 1 DoF system. The system is modeled with the equation of motion in the cross-flow direction given as:

$$\frac{\partial^2 y}{\partial t^2} + 4\pi\zeta \frac{\partial y}{\partial t} + 4\pi^2 x = \frac{2}{\pi} \frac{U_r^2 C_D}{m^*(1 + d/D)} \quad (3-7)$$

where x and y denote the in-line and cross-flow displacements, respectively, U_r is the reduced velocity and ζ is the damping ratio. The mass-ratio is given by

$$m^* = \frac{m}{m_d} \quad (3-8)$$

where m is the mass of the cylinder and m_d is the displaced mass. The structural damping ratio is given by:

$$\zeta = \frac{c}{2\sqrt{km}} \quad (3-9)$$

with c being the structural damping and k the structural stiffness

The lift and drag coefficients C_L and C_D are computed by:

$$C_L = \frac{1}{\frac{1}{2}U_\infty^2 \rho DL} \int_{\Gamma} [(-pI + \mu(\nabla u + (\nabla u)^T))n]n_y d\Gamma \quad (3-10)$$

$$C_D = \frac{1}{\frac{1}{2}U_\infty^2 \rho DL} \int_{\Gamma} [(-pI + \mu(\nabla u + (\nabla u)^T))n]n_x d\Gamma \quad (3-11)$$

where ρ is the fluid density, Γ the surface area of the cylinder, L the spanwise dimension of the cylinder, n the unity vector normal to the cylinder surface and I is the identity tensor. The fluid forces on the cylinder, F_x in streamwise direction and F_y in cross-flow direction, are computed by solving iteratively the flow equations (3-1) and (3-2) together with the structural equation (3-7).

3.2 The Finite Volume Method

The Finite Volume Method (FVM) is the most common method for CFD simulations. For the simplicity only this method is considered here. This method is based on discretization. Discretization means that differential equations are transformed into algebraic equations.

For a simulation of an unsteady flow three discretization steps are performed:

Spatial discretization: splitting the space domain in to control volumes (CV), so called meshing.

Temporal discretization: the time domain is split in to timesteps.

Equation discretization: applying the governing equations, this results in a system of algebraic equations for the specific locations in the computational mesh.

3.2.1 Spatial Discretization

The space domain is split into a finite amount of control volumes (CV). A control volume has flat faces that are shared with neighboring CVs or a boundary condition. Control volumes are used for the calculation of the values in the mesh and the values are stored in the centroid of a CV. The values of all centroids are stored in an arrangement called the grid or mesh. For the CFD code used in this study the values on the surface of a CV are obtained by interpolation. linear interpolation is used for this study.

3.2.2 Temporal Discretization

Unsteady flows require discretization in time. Temporal discretization is achieved by the integration over the time of the discretization equation. For the time discretization the implicit backward time integration scheme is used in the present study. The scheme expresses the face values based on the values of the old time-levels. It can be written as:

$$\frac{\partial}{\partial t} \phi = \frac{1}{\Delta t} \left(\frac{3}{2} \phi - 2\phi^o + \frac{1}{2} \phi^{oo} \right) \quad (3-12)$$

where ϕ^o donates the old and ϕ^{oo} old time levels. Δt is the time step.

3.3 Numerical Model and Approach

The governing equations are solved numerically using the open-source finite volume CFD code OpenFOAM (Weller, et al. 1998) (Greenshields 2020). The turbulent flow is modeled using LES methodology. The PIMPLE algorithm combining the Pressure-Implicit Split-Operator (PISO) and the Semi-Implicit Method for Pressure-Linked Equations (SIMPLE) is applied to solve the pressure-velocity coupling. The time discretization is handled by the second order implicit backwards scheme. The spatial discretization applies the second order Gauss linear scheme. Therefore, the overall method is of second order accuracy.

3.4 Turbulence Modeling

There are three popular methods for the modeling of turbulent flow. Direct Numerical Simulation (DNS), Large Eddy Simulations (LES), Reynolds-Averaged Navier-Stokes approach (RANS) and Unsteady Reynolds-Averaged Navier-Stokes approach (URANS). The DNS approach solves the full Navier Stokes equation and no turbulence model is used, eddies of all sizes are resolved. In order to resolve small eddies a fine mesh and a small timestep is necessary, which is resulting in high computational costs. RANS is a steady state solver that is used for steady state simulations. For the URANS solver the mean quantities change over time so that it can be used for transient simulations. RANS and URANS simulations require significantly less computational time than LES or DNS but come in a reduction in the accuracy of the result. For the LES approach only the large scale eddies are resolved. Small scale eddies are ignored, which is achieved by applying a low pass filter to the Navier-Stokes equation. To accurately resolve a turbulent flow LES still requires a fine mesh with is associated with high computational cost. However, the computational demand is significantly reduced compared to DNS and has a higher accuracy than the RANS simulation. Hence a LES is selected for this study. In a LES the velocity field is separated in a filtered (resolved) part and a sub grid scale (SGS) component (Moghadam, Zahra and Garon 2021)

3.5 Mesh Generation

Due to the sensitivity of the mesh quality to the computational cost and the accuracy of the solution, the mesh generation is an important task that is given a lot of attention. A mesh is consisting of a finite number of cells. Figure 11 shows the terminology for a three-dimensional mesh. The surfaces of a cell is called a face and is constrained by edges. The points on the cell vertices are called a node.

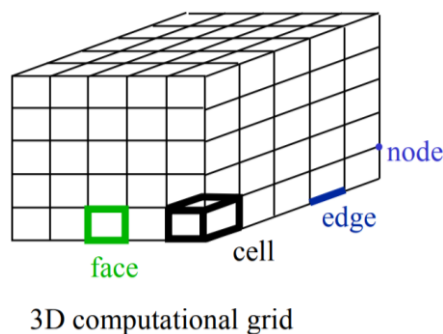


Figure 11: Grid terminology (Bakker 2002)

Different types of cells are shown in Figure 12. The structured mesh that is used for the simulation in this study consist of hexahedron cells.

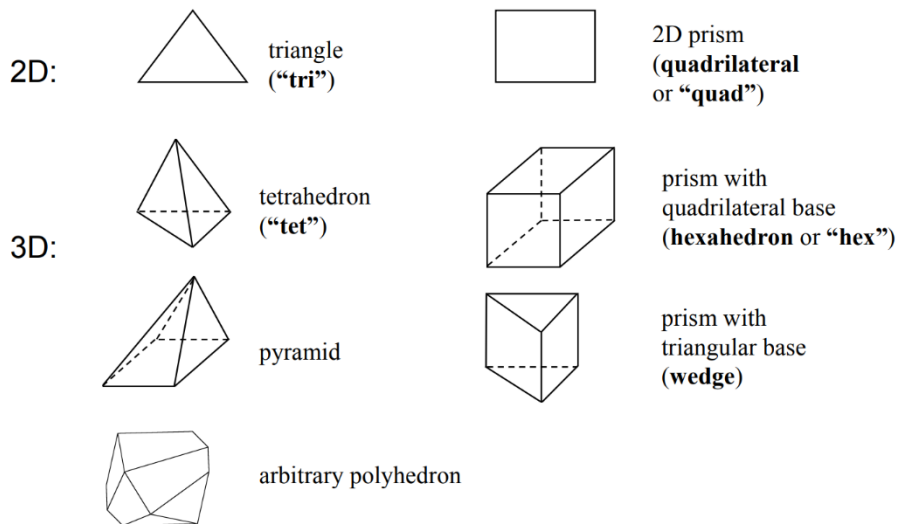


Figure 12: Typical cell shapes (Bakker 2002)

The computational mesh can be classified into structured or unstructured. Figure 13 shows an example of a structured and unstructured mesh.

Structured meshes: have a regular distribution of cells and every cell has a fixed number of faces. The cells in the mesh are arranged following a clear pattern. Grid points are located along coordinate lines and can therefore be addressed by coordinates. In a 2D case cells are quadrangles.

Unstructured meshes: have cells of different amounts of faces and no regular structure. All cells must be numbered individually. In a 2D case, cells are commonly triangles.

The structured grid has advantages in the memory usage compared to the unstructured mesh, while the unstructured mesh makes it easier to model complex geometry and can easily be used for mesh refinement in certain areas of the domain.

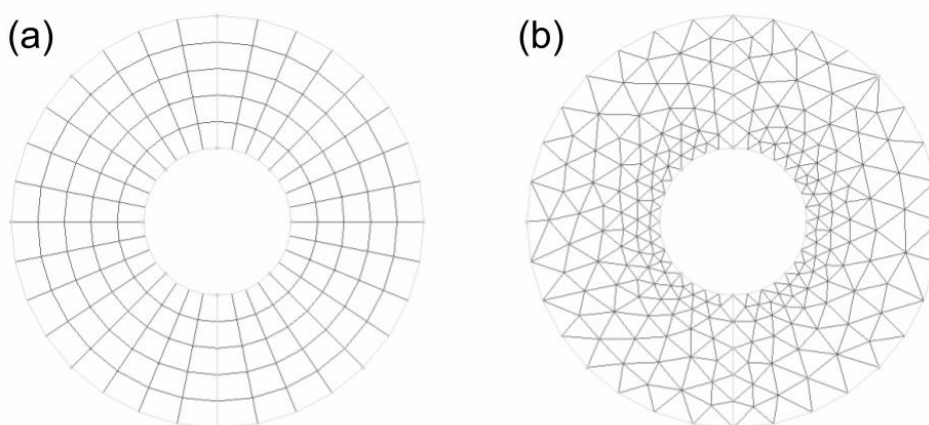


Figure 13: Structured (a) and Unstructured (b) mesh

3.6 Assessment of Mesh Quality

For the assessment of the mesh quality the parameters such as: equiangle skewness, nonorthogonality, smoothness and aspect ratio are important.

Equiangle Skewness describes how distorted a cell is and is defined by

$$\max \left[\frac{\theta_{max} - \theta_e}{180 - \theta_e}, \frac{\theta_e - \theta_{min}}{\theta_e} \right] \quad (3-13)$$

where θ_{max} and θ_{min} are the biggest and smallest angles of a cell and θ_e is the angle for an equiangular cell (90° for a hexahedron) (Bakker 2002).

Nonorthogonality is defined as the angle between a vector that connects the centroids of two cells and the normal vector of the face between the cells. For the CFD code Open FOAM the nonorthogonality should be less than 65° .

Smoothness describes the difference between the volume of neighboring cells. Figure 14 shows an example of a smooth and non smooth cell arrangement.

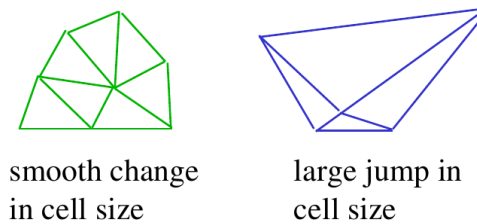


Figure 14: Smoothness of cells (Bakker 2002)

Aspect ratio is defined as the ratio between the longest edge to the shortest edge of a cell. Figure 15 shows cells at high and low aspect ratios.

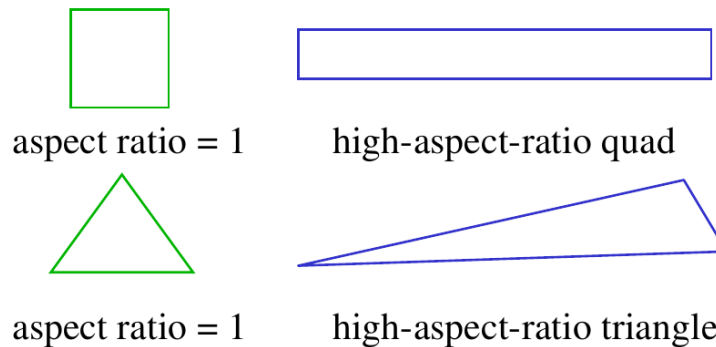


Figure 15: Aspect ratio (Bakker 2002)

Some areas in the domain require a high cell density to properly resolve complex flow phenomena like the boundary layer. Figure 16 shows a mesh that has smaller cell spacing close to the cylinder to accurately resolve the boundary layer.

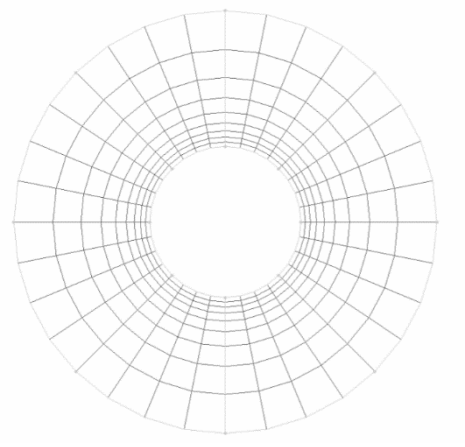


Figure 16: Refined mesh in the region of the boundary layer

4 Simulation of Fluid Flow around Stationary Cylinder

4.1 Numerical Domain and Computational Grids

The size of the computational domain is $(L_x \times L_y \times L_z) = (40D \times 20D \times 4D)$ and the schematic of the domain is shown in Figure 17. Prsic et al. (2014) conducted extensive simulations for the flow around static smooth cylinders in the subcritical regime and reported that in order to properly resolve spanwise velocity fluctuations a domain size of at least $4D$ in the spanwise direction is required. Therefore, in the present simulations the domain is chosen to be $4D$ in the spanwise direction. The boundary conditions used in the present simulations are set as following:

The inlet is prescribed with a uniform flow profile with component values set to be $\bar{u}_x = 1$, $\bar{u}_y = 0$ and $\bar{u}_z = 0$;

A no-slip boundary condition is applied on the cylinder surface as $\bar{u}_x = \bar{u}_y = \bar{u}_z = 0$;

The upper and lower boundaries are specified as symmetry boundary condition, where

$$\frac{\partial \bar{u}_i}{\partial n} = 0 \text{ and } \frac{\partial p}{\partial n} = 0 ;$$

In the spanwise direction, a cyclic boundary condition is imposed;

At the outlet, a reference pressure is set to be $p = 0$ and $\frac{\partial \bar{u}_i}{\partial n} = 0$.

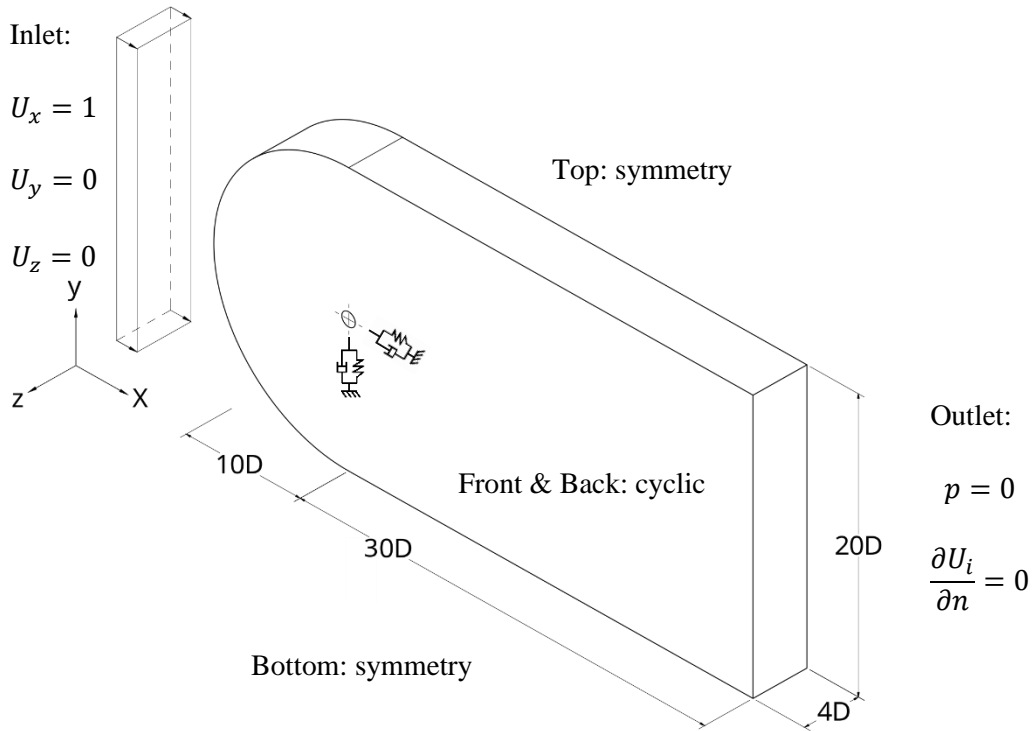


Figure 17: Schematic of the computational domain with imposed boundary conditions.

4.2 Computational Mesh

The accuracy of LES simulations is highly dependent on the computational grid density and quality of computational cells. The computational grid topology in the x - y plane used in present simulations is showed in Figure 18. The circular zone around the cylinder is generated by radial extrusion of quadrilateral cells with a constant stretching factor $r_s = 1.05$. Downstream the cylinder cells are clustered in the wake region, away from the wake region cells are progressively stretched to decrease the overall cell number and, therefore, the computational cost. Grid in the spanwise direction (z -axis) is generated by extruding the 2D grid (Figure 18) with n equidistant steps.

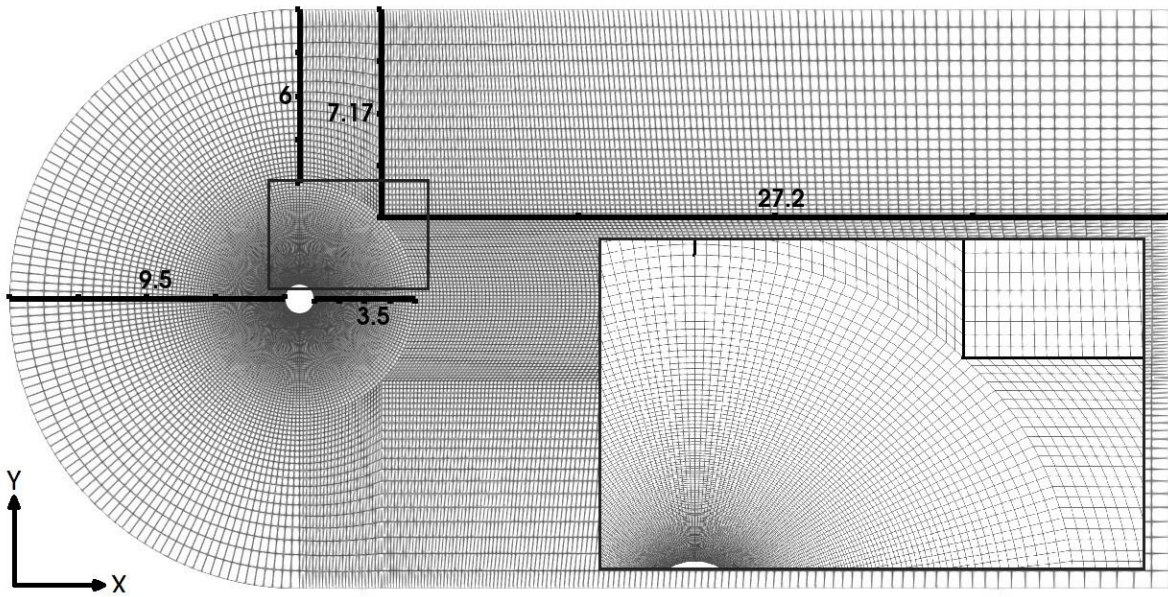


Figure 18: Computational grid overview in x - y plane, dimensions given in terms of cylinder diameter (D). In the spanwise (z -axis) direction the grid is formed by extruding n -times the presented 2D grid using uniform spacing.

4.3 Mesh Convergence Study

A mesh sensitivity study is performed to make sure that the results are independent of the mesh size. Three simulations of a static cylinder with different mesh resolutions are performed. To evaluate the influence of the mesh size on the results, representative hydrodynamic quantities are compared. The mesh resolution is refined with a constant refinement factor. The cell number for each mesh is shown in Table 2. St and $\overline{C_D}$ are relatively insensitive to mesh refinement and the relative error between the cases with the normal and fine mesh is smaller than 5%. The C_L^{rms} shows larger variation and is sensitive to mesh resolution. The large differences between the obtained C_L^{rms} values can be partially attributed to the random nature of the turbulent fluctuations in the separated shear layers. In Figure 19 the pressure coefficient (C_p) over the cylinder surface is shown, the simulation results for cases with fine and normal

meshes are in close agreement. The simulation with the coarse mesh overpredicts slightly suction on the downstream side of the cylinder after the shear layer separation. Figure 20 shows the streamwise velocity in the wake along a straight line in the direction of the flow, for all three investigated mesh variants. The simulations with dense and normal mesh predict a recirculation bubble of a similar size. The simulation on the coarse mesh predicts a smaller recirculation bubble length and a larger streamwise velocity behind the recirculation bubble and a smaller streamwise velocity far in the wake ($x/D > 4$) compared with fine and normal cases. Figures 21 and 22 show, respectively, the time- and spanwise-averaged cross-flow and streamwise velocity in the cylinder's wake at different x/D positions. The results from the simulations with the fine and normal meshes show similar velocity distributions in the wake while the simulation result with coarse mesh deviate significantly from fine and normal cases. The skin friction factor (C_f) distribution on the cylinder surface is shown in Figure 23. The simulations with normal and fine meshes predict the same C_f distribution on the cylinder's surface. The simulation with the coarse mesh predicts higher C_f values for $\theta = 35^\circ - 87^\circ$ and shows different C_f distribution at the backside of the cylinder after separation point ($\theta = 87^\circ - 140^\circ$).

The comparison of the simulation results of the streamwise velocity and cross-flow velocity indicates that the simulation with the coarse mesh is not as accurate as the other simulations. The simulations with normal and fine meshes give similar results. For the fine and normal mesh cases, the differences between $\overline{C_D}$ and St are smaller than 1% and the predicted separation angles are nearly identical. The results obtained in the mesh sensitivity study show a clear convergent behavior when increasing mesh refinement and are in support for selecting the normal mesh variant for further computations which provides a good balance of computational cost and accuracy.

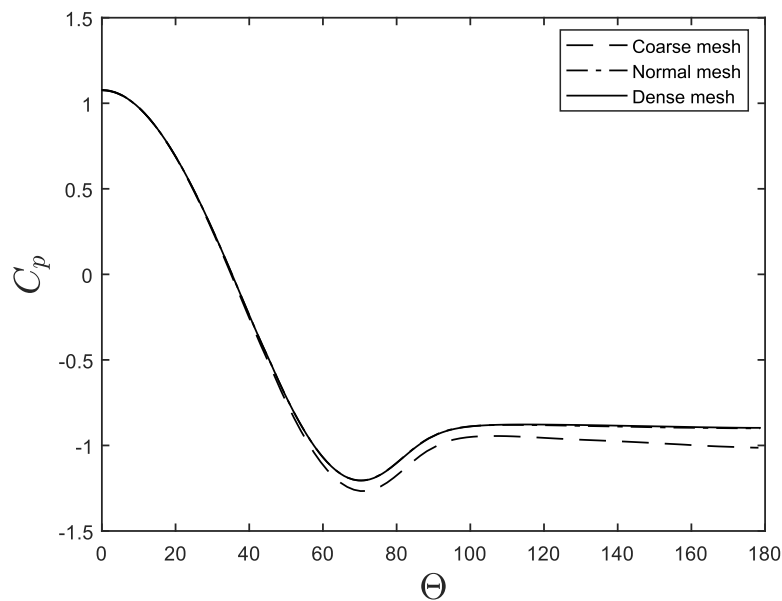


Figure 19: Pressure coefficient (C_p) over the surface of the cylinder for different mesh variants.

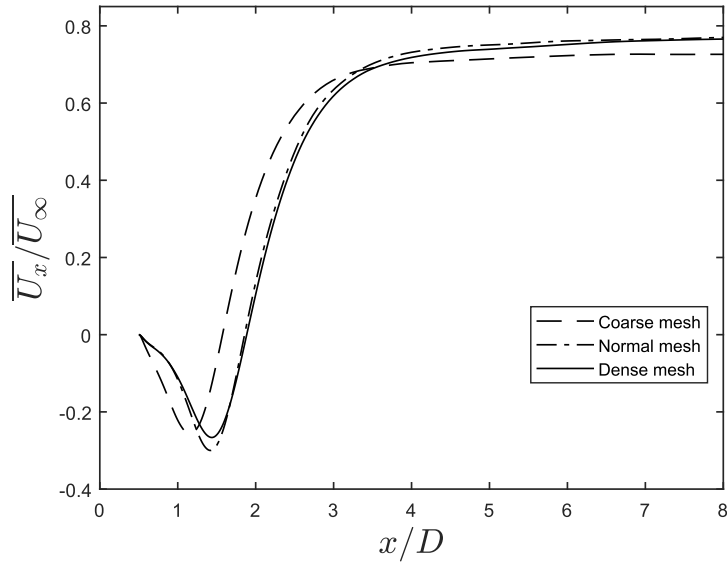


Figure 20: Normalized time- and spanwise-averaged streamwise velocity component ($\overline{U_x}/\overline{U_\infty}$) in the wake of the cylinder (centerline in the x - y plane) for different mesh variants.

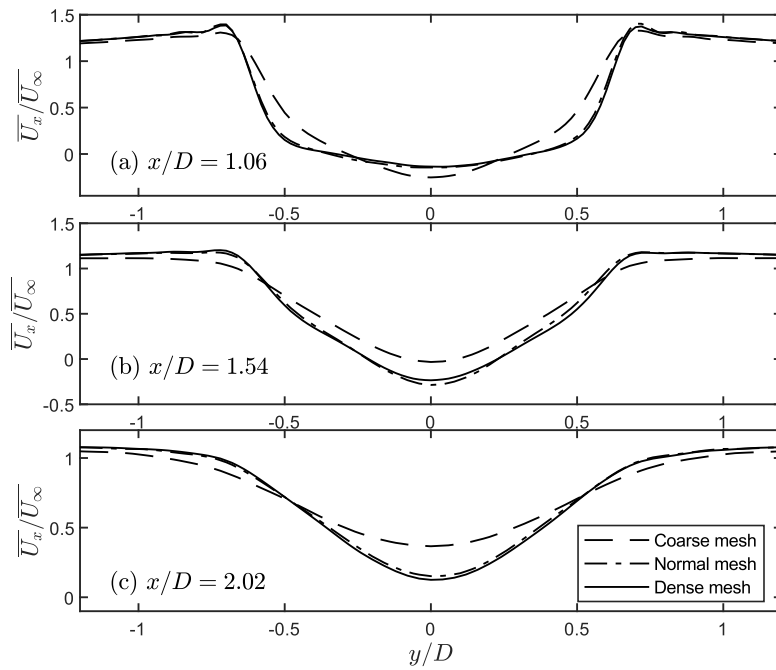


Figure 21: Normalized time- and spanwise-averaged streamwise velocity component ($\overline{U_x}/\overline{U_\infty}$) at three different locations in the wake of the cylinder in the x - y plane for different mesh variants.

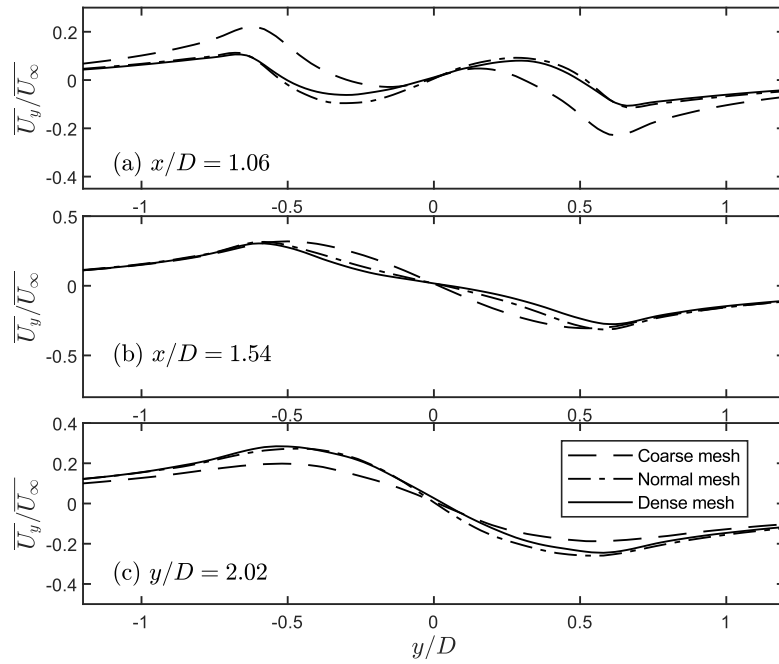


Figure 22: Normalized time- and spanwise-averaged cross-flow velocity component ($\overline{U_y/U_\infty}$) at three different locations in the wake of the cylinder in the x - y plane for different mesh variants.

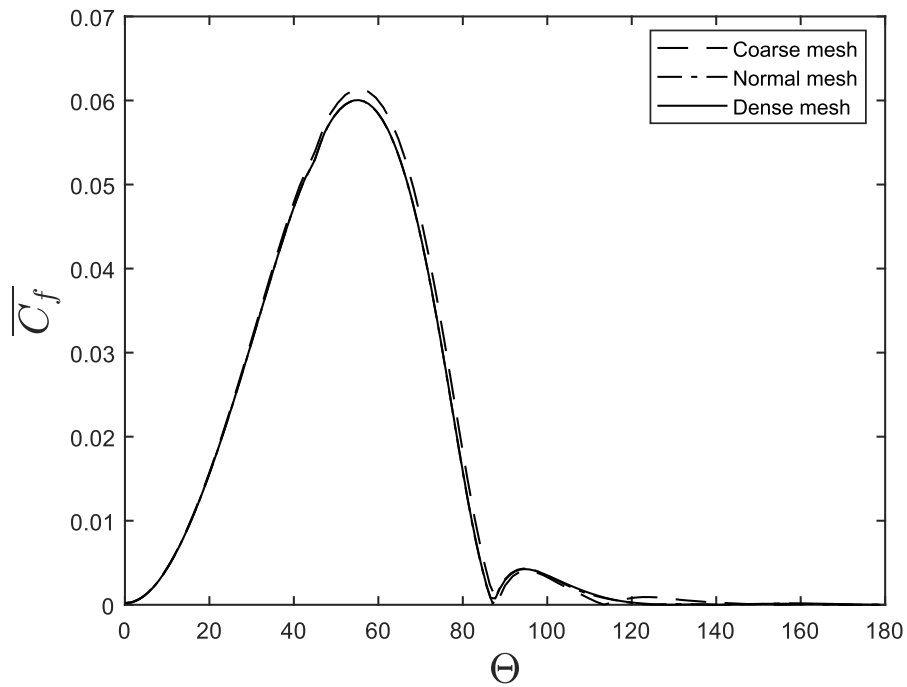


Figure 23: Absolute value of the time- and spanwise-averaged skin friction coefficient (C_f) on the cylinder surface for different mesh variants.

Table 2: Mesh density sensitivity study

Mesh parameters:			Hydrodynamic parameters:			
Mesh No.	Mesh density	Cell count	$\overline{C_D}$	C_L^{rms}	St	Separation angle (Θ)
L1	Coarse	2636296	1.1178(7.8%)	0.2734(54.6%)	0.2198(0.7%)	87.97°
L2	Normal	5031296	1.04(0.3%)	0.1574(-10.9%)	0.2193(0.5%)	87.02°
L3	Fine	9935520	1.0362	0.1768	0.2182	87.14°

4.4 Time step Convergence Study

In order to obtain a result that is independent of the time step size, three simulations with different time steps are performed.

Table 3 shows the resulting representative hydrodynamic quantities for different time step sizes. The differences between the hydrodynamic quantities of the investigated cases are small with a relative difference of max 1.8% for $\overline{C_D}$ and 1% for St . A large variation in the C_L^{rms} is observed due to the stochastic variation of the lift force and not the difference in the time step. The max courant number defined as $Co = \frac{u\Delta t}{\Delta l}$ is below 1 for all simulation cases. Based on the results of time step sensitivity study, a time step $\Delta t = 0.002$ is considered to be sufficient and is selected for the remaining simulations presented in this paper.

Table 3: Time step sensitivity study.

Mesh No.	Mesh parameters:				Hydrodynamic parameters:			
	Mesh density	Time step	Cell count	Max Courant number	$\overline{C_D}$	C_L^{rms}	St	Separation angle (Θ)
L2	Normal	$\Delta t = 0.002$	5031296	0.62	1.05(-1.8%)	0.1776(-15.5%)	0.2179(-1.0%)	87.18°
L2	Normal	$\Delta t = 0.001$	5031296	0.29	1.03(-3.7%)	0.1409(-32.9%)	0.2203(0.0%)	87.25°
L2	Normal	$\Delta t = 0.0005$	5031296	0.15	1.07	0.2102	0.2203	87.35°

4.5 Validation Study

A series of simulations using normal mesh of Mesh No L2 and time step of $\Delta t = 0.002$ is performed and compared with the experimental measurements for the same configuration and flow parameters to validate the present numerical model. Figure 24 shows the comparison of the time- and spanwise-averaged streamwise velocity component ($\overline{U_x}/\overline{U_\infty}$) in the wake of the cylinder (centerline in the x - y plane) from the present simulation with the experimental data from Parnaudeau et al. (2008), Ong and

Wallace (1996) and Lourenco and Shih (1993). There is a good agreement between the present values of $\overline{U_x}/\overline{U_\infty}$ and measurements made by Parnaudeau et al. (2008). Figures 25 and 26 show, respectively, the time- and spanwise-averaged streamwise and cross-flow velocity components at different locations in the wake. Similar to the streamwise velocity distribution along the centerline, the $\overline{U_x}/\overline{U_\infty}$ and $\overline{U_y}/\overline{U_\infty}$ distributions in the wake show very good agreement with the measurements by Parnaudeau et al. (2008). The C_p distribution showed in Figure 27 matches closely the data reported by Norberg and Sunden (1987) and Ma et al. (2000). Figure 28 shows the skin friction factor from the present simulations and data from measurements by Son and Hanratty (1969) at $Re = 5000$. The magnitude of C_f is not precisely fitting the experimental data due to Re difference between the present simulation and the experiment. However, the separation point is similar in both cases at around $\approx 86^\circ$.

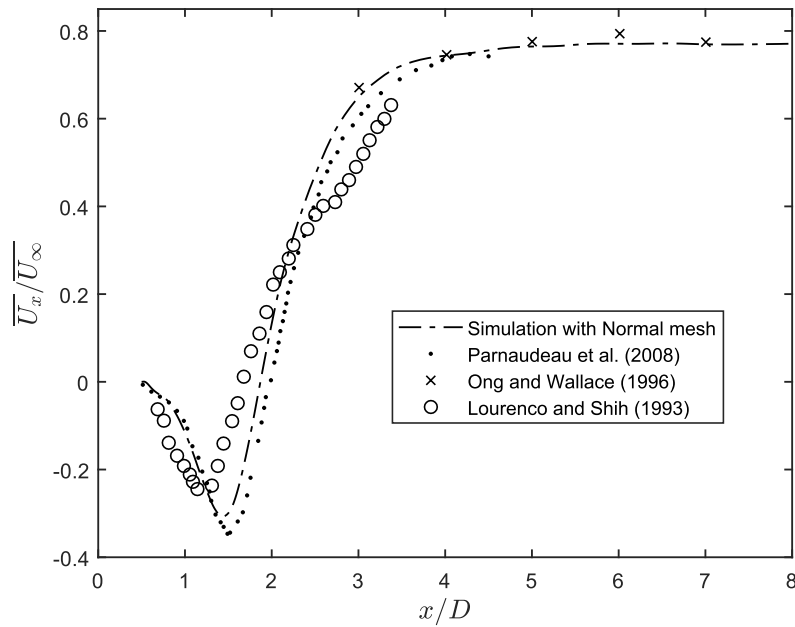


Figure 24: Comparison of the time- and spanwise-averaged streamwise velocity component ($\overline{U_x}/\overline{U_\infty}$) in the wake of the cylinder (centerline in the x - y plane) with experimental data from Parnaudeau et al. (2008), Ong and Wallace (1996) and Lourenco and Shih (1993) data taken from Kravchenko and Moin (2000).

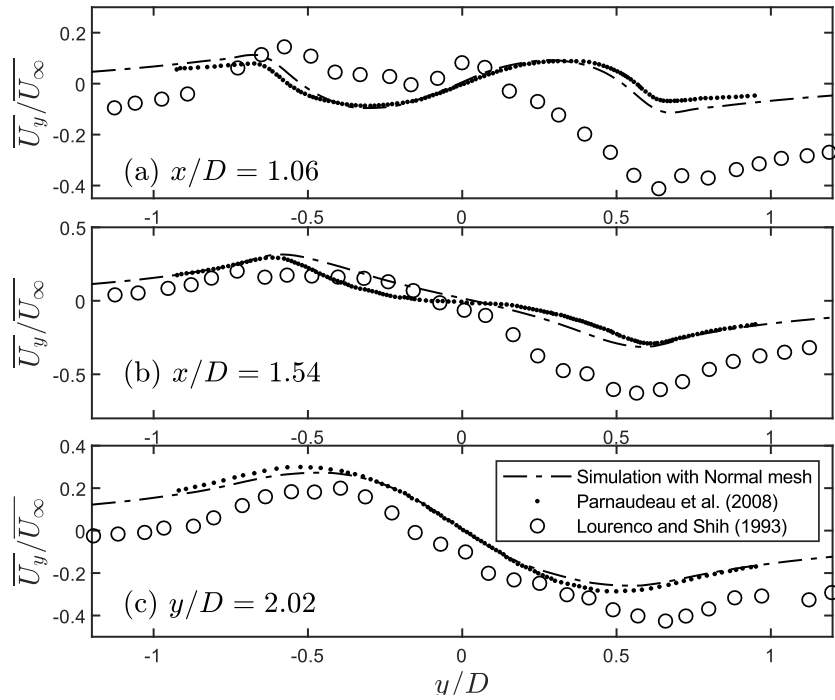


Figure 25: Comparison of the time- and spanwise-averaged cross-flow velocity component ($\overline{U}_y/\overline{U}_\infty$) at three different locations in the wake of the cylinder in the x - y plane with experimental data from Parnaudeau et al. (2008) and Lourenco and Shih (1993).

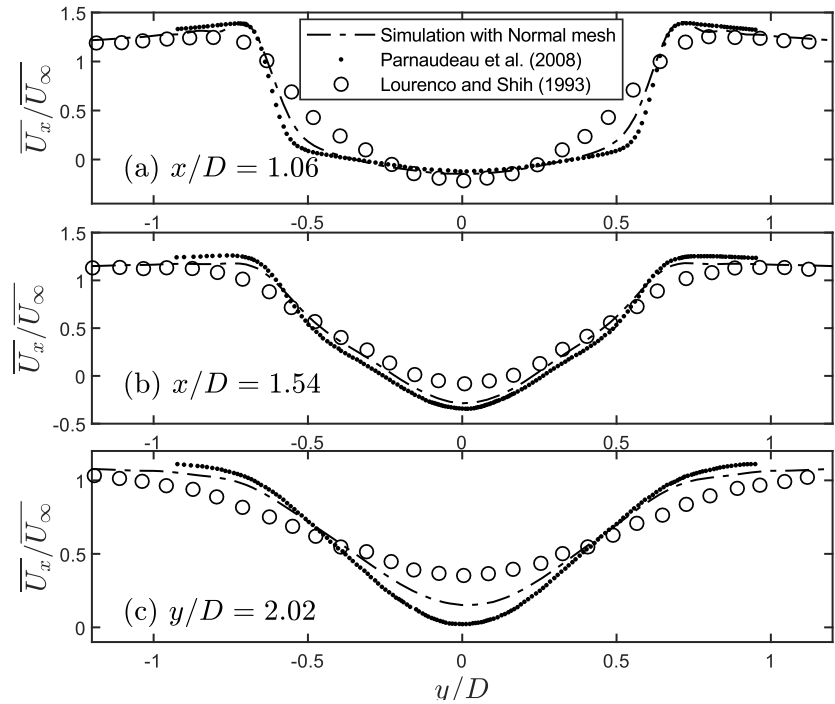


Figure 26: Comparison of the time- and spanwise-averaged streamwise velocity component ($\overline{U}_x/\overline{U}_\infty$) at three different locations in the wake of the cylinder in the x - y plane ($x/D = 1.06, 1.54, 2.02$) with experimental measurements by Parnaudeau et al. (2008) and Lourenco and Shih (1993).

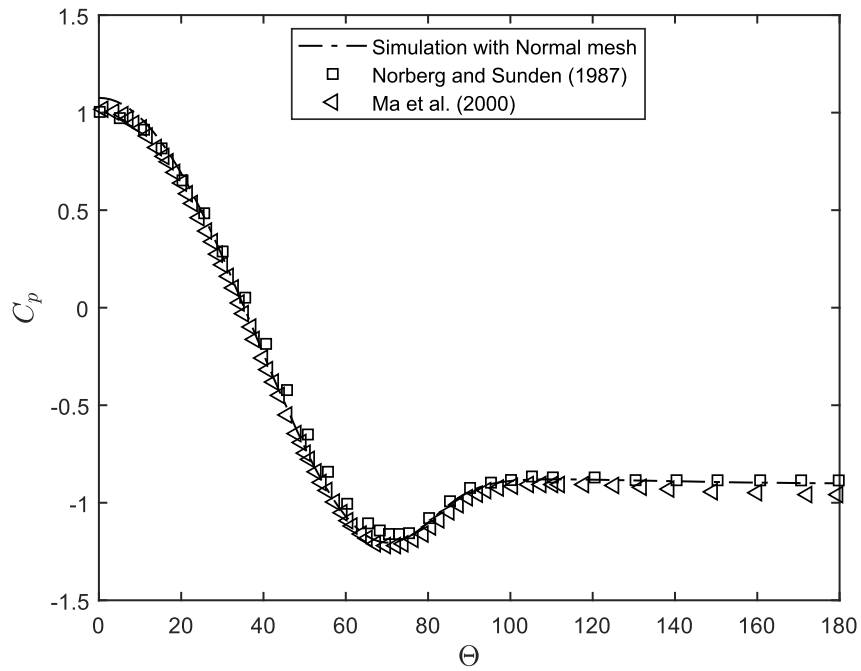


Figure 27: Comparison of the pressure coefficient (C_p) on the cylinder surface with experimental measurements by Norberg and Sunden (1987) and Ma et al. (2000).

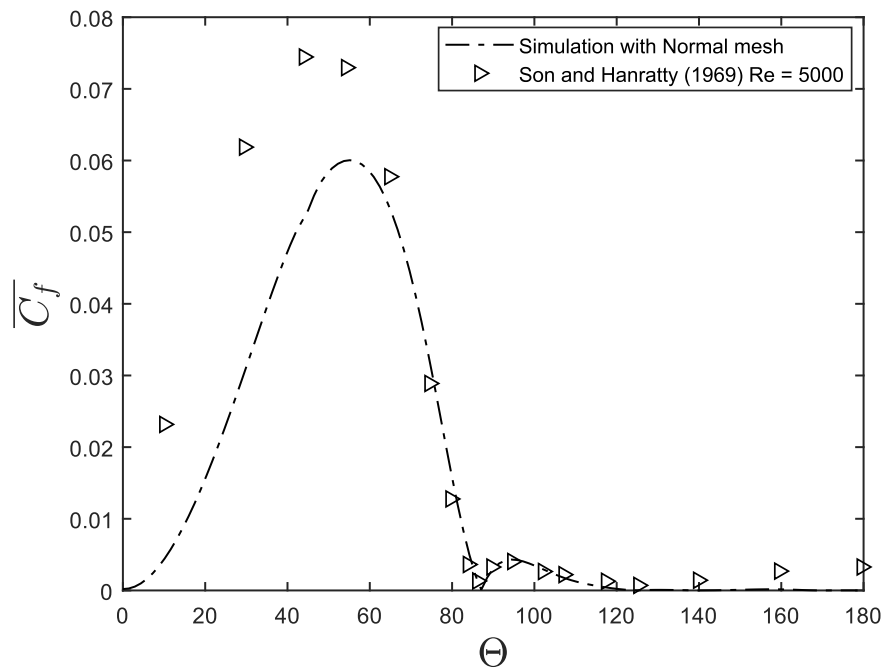


Figure 28: Comparison of the absolute value of the skin friction coefficient (C_f) on the cylinder surface with experimental data from Son and Hanratty (1969) at $Re = 5000$.

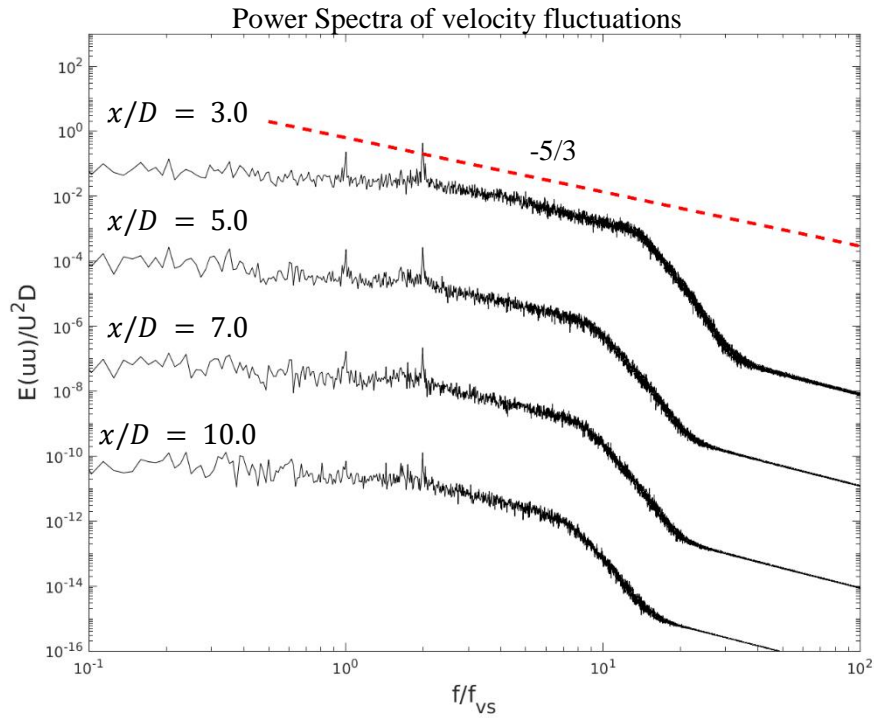


Figure 29: Power spectra of the streamwise velocity fluctuations measured at different locations in the wake of the cylinder.

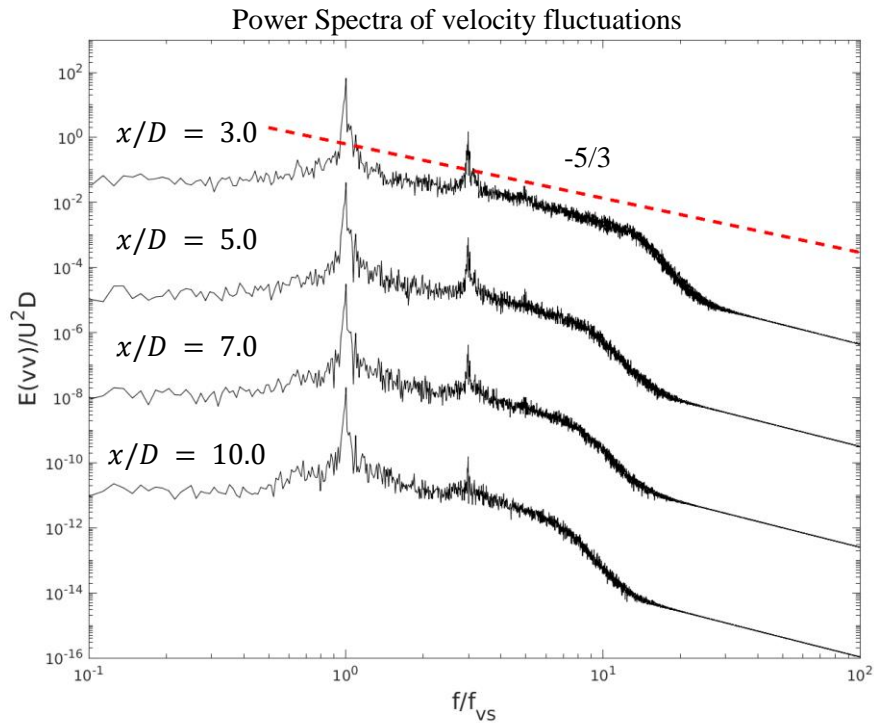


Figure 30: Power spectra of the cross-flow velocity fluctuations measured at different locations in the wake of the cylinder.

Figures 29 and 30 show the power spectral densities (PSD) of the fluctuating components of the streamwise and cross-flow velocity at different locations in the wake of the cylinder. Only the plots for the $x/D = 3.0$ conform to the y -axis scale while plots for other x/D position are offset to prevent the

plot lines from overlapping and becoming unreadable. The frequency is normalized by the vortex shedding frequency (f_{vs}). The present simulations appear to capture the inertial subrange with a characteristic $-5/3$ slope, thus satisfy the Kolmogorov's scaling law. At around $\frac{f}{f_{vs}} \approx 20$ the power spectra depart from the $-5/3$ slope. The late departure from the $-5/3$ line indicates that most of the turbulent energy cascade is resolved by the LES model in the simulations.

Overall, it can be concluded that the simulations results are in a very good agreement with the experimental data. The present numerical model appears to be suitable for investigating fluid-structure interaction problems of bluff bodies at $Re = 3900$.

5 Simulations of Self-excited Cylinder Vibrations

A series of simulations of a cylinder undergoing vortex-induced vibration is presented and discussed in this section. The physical properties of the modeled cylinder are set to be $m^* = 2.6$ and $Re = 3900$, to approximate the experimental setup used by Assi, Bearman and Meneghini (2010) ($m^* = 2.6$, $Re \in [3300, 5833]$). Three simulation cases are performed for $Ur \in [4, 5, 7]$. The normalized cross-flow displacement \hat{y}/D is calculated by taking the root mean square (RMS) of the displacement series and multiplying by $\sqrt{2}$. The first 10 oscillation cycles are removed from the analysis to exclude the effect of initial transient, thus the fully developed flow is considered. Figure 31 shows \hat{y}/D predicted by the present simulations compared with the experiment conducted by (Assi, Bearman and Meneghini, On the wake-induced vibration of tandem circular cylinders: the vortex interaction excitation mechanism. 2010). In the upper branch of the VIV response (Ur 4 and Ur 5 in Figure 31) the results from the simulation cases are slightly lower than the experimental results. A possible reason for this could be due to the different Re values. For the experiment at Ur 4, $Re = 3300$, at Ur 5, $Re = 4166$ and at Ur 7, $Re = 5833$ while in the simulations a constant $Re = 3900$ is used.

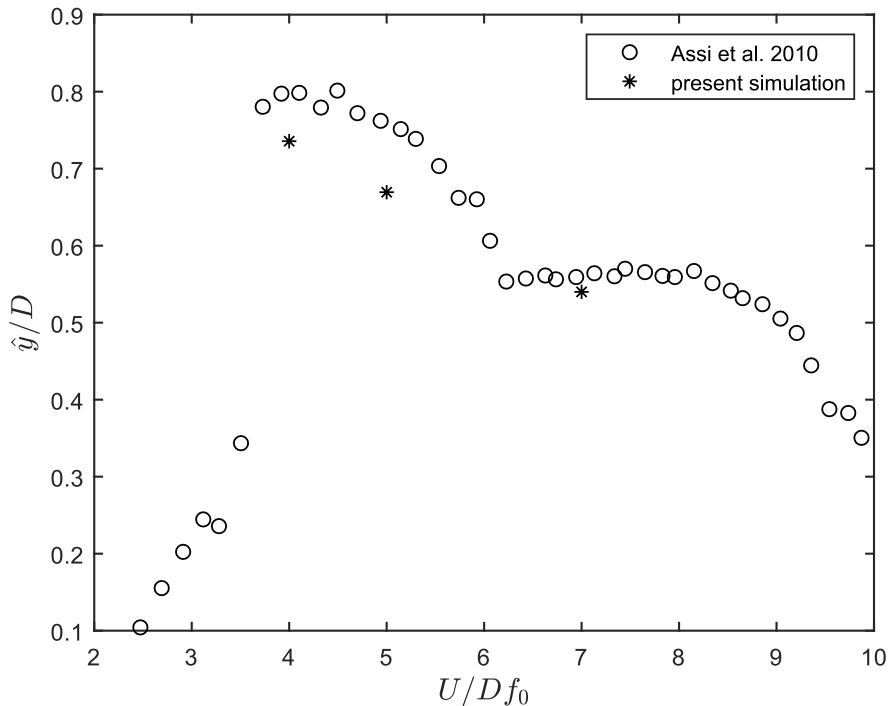


Figure 31: Comparison of normalized cross-flow vibration amplitudes obtained by the present simulations compared with experimental measurements by Assi, Bearman and Meneghini (2010).

The time series of hydrodynamic forces and displacement from the simulation are analyzed. $\overline{C_d}$ is calculated by excluding the time tU/D from 0 to 40, to exclude the buildup phase. Figures 32-34 show a time window from $tU/D = 70$ to 120 of the cross-flow displacement (y/D), C_L and C_D time series

for the simulation cases. For the case with Ur 4, C_L and y/D signals are approximately sinusoidal while for the cases with Ur 5 and Ur 7 there is a clear additional harmonic content resulting in irregular signals. The simulation case with Ur 5 shows the highest value of $\bar{C}_D = 2.51$, see Figure 33. Even though the cross-flow displacement is highest for the simulation case with Ur 4 the drag is highest for the case with Ur 5. The oscillation in the drag coefficient is the most stable for this case. The Ur 7 simulation shows a beating of the drag coefficient where the drag amplitude varies over time and this could be the result of the superposition of two oscillations with a similar frequency.

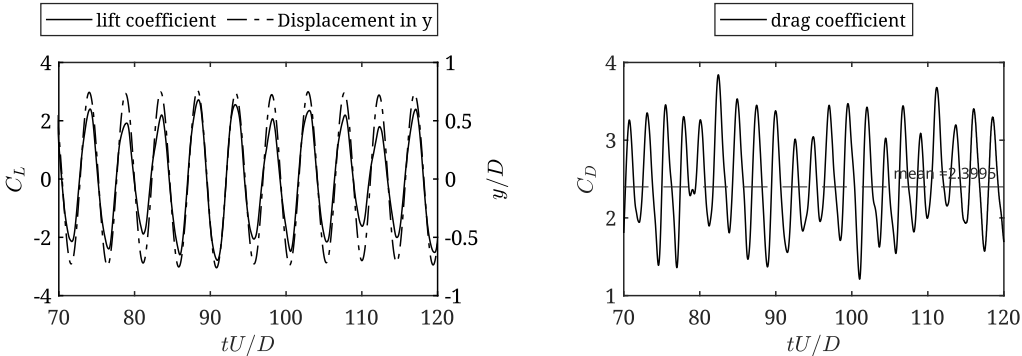


Figure 32: Time series of lift coefficient and cross-flow displacement (a) and drag coefficient (b) for Ur 4.

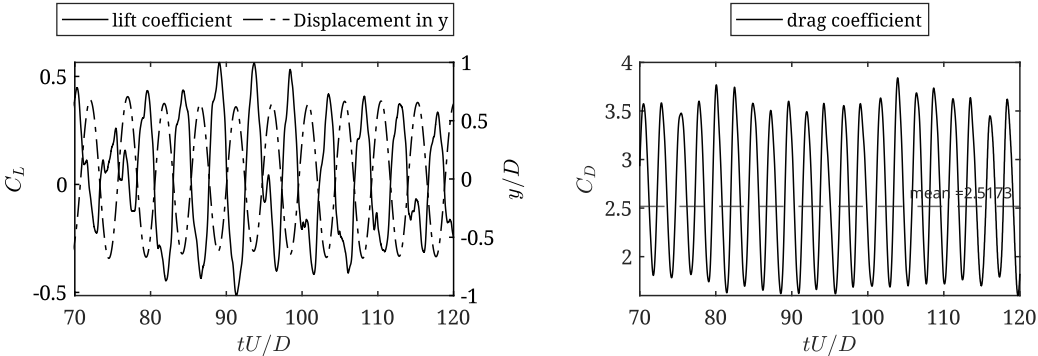


Figure 33: Time series of lift coefficient and cross-flow displacement (a) and drag coefficient (b) for Ur 5.

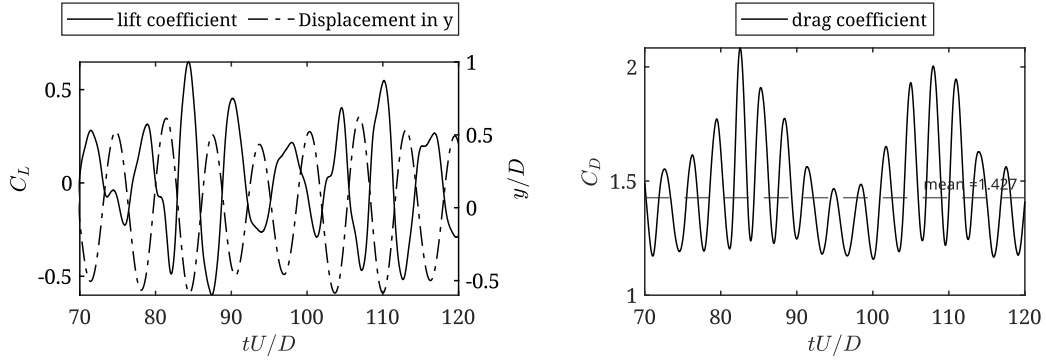


Figure 34: Time series of lift coefficient and cross-flow displacement (a) and drag coefficient (b) for Ur 7.

Power spectral densities of C_l and C_d are computed to identify the dominant frequencies of hydrodynamic forces. The spectral values are normalized by their max value. Figure 35-37 show the power spectral densities of C_l and C_d for the investigated simulation cases. For the case with Ur 4 (Figure 35) the dominant peak in the $|\hat{C}_l|$ spectra occur at $f/f_n = 0.84$ and the dominant peak in the spectra of $|\hat{C}_d|$ occurs at $f/f_n = 1.67$. The power spectra of $|\hat{C}_l|$ for the case with Ur 5 (Figure 36) show a clear peak around $f/f_n = 3.1$ which indicates presence of a third harmonic component in the lift force. For the case with Ur 7 (Figure 37) there is a secondary peak at $f/f_n = 2.5$ close to the dominant peak at $f/f_n = 2.2$. This can explain the beating of the drag force (see Figure 35) since the interference between two signals with slightly different frequencies will result in a periodic variation in signal amplitude with a frequency that is the difference of the two interfering frequencies. In Figure 37(b) there is a clear peak at $f/f_n = 0.3$ as a result of the beating phenomenon.

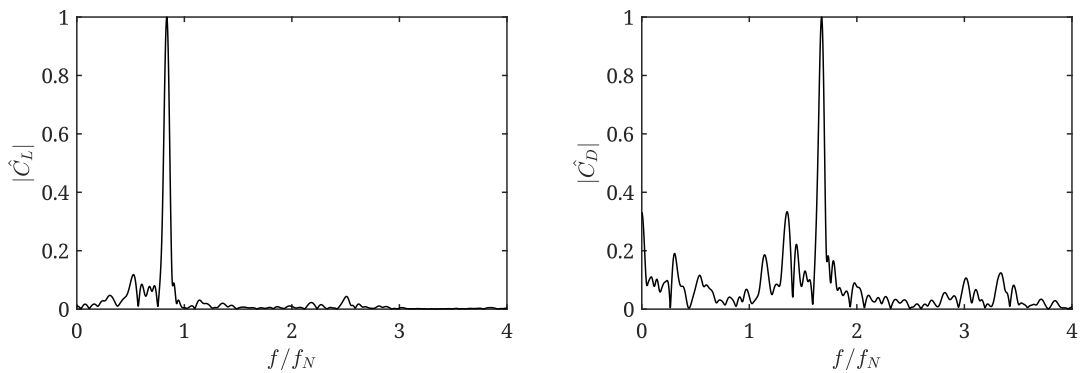


Figure 35: Normalized power spectral density of lift (a) and drag (b) coefficients for Ur 4.

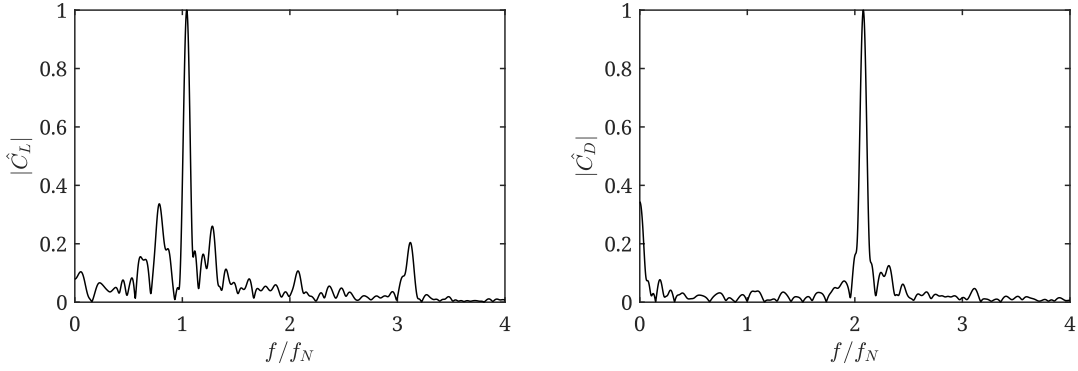


Figure 36: Normalized power spectral density of lift (a) and drag (b) coefficients for Ur 5.

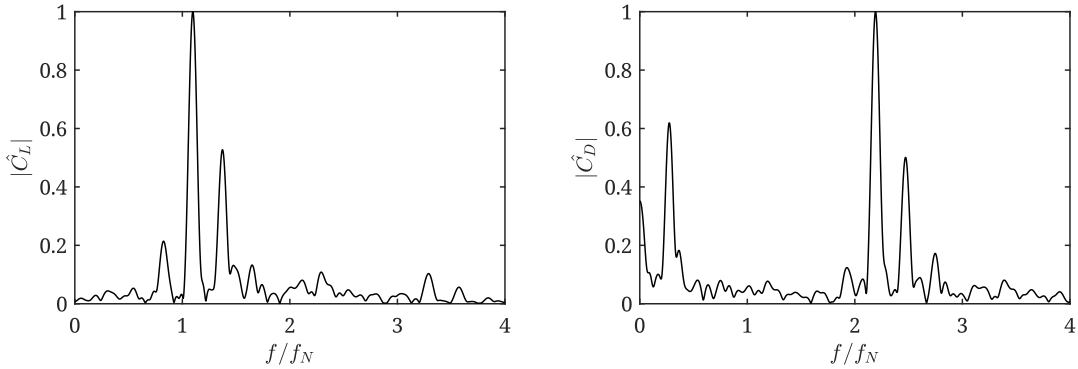


Figure 37: Normalized power spectral density of lift (a) and drag (b) coefficients for Ur 7.

For the identification of vortex shedding modes, the iso-surfaces of pressure coefficient and Q-criterion are generated and plotted in a three-dimensional (3D) view. The iso-surfaces are colored by spanwise vorticity magnitude, where blue color indicates clockwise vortex rotation and red color indicates counterclockwise rotation. The 3D view of C_p iso-surface shown in Figure 39 clearly reveals the 2S shedding pattern. In the 2S vortex shedding pattern a single clockwise and a single counterclockwise vortex are shed. All vortices on one side rotate in the same direction and the rotation direction changes with each vortex that is shed per cycle. The turbulent wake structures for the simulation case with $Ur = 5$ are shown in figures 40 and 41. Here, the vortex shedding mode is also classified as 2S type. The C_p iso-surface pattern looks similar to that observed for the case with Ur 4 (see figures 38 and 39). Compared with the case with Ur 4 (Figure 38), the vortex cores in the case with Ur 5 are more distorted with secondary longitudinal vortices developing in the $x - y$ direction between the main spanwise vortices. During the buildup of the simulation when the cylinder starts to oscillate the vortex shedding mode changes temporarily to a $2P_0$ pattern. The $2P_0$ pattern defined by Morse and Williamson (2009) is a pattern similar to 2P but the secondary vortex is much weaker. This shedding pattern occurs when the cross-flow displacement reaches the maximum value around $tU/D = 20$, a corresponding snapshot

of C_p iso-surface is shown in Figure 42. Figure 43 and 44 show the wake structures for the simulation case with Ur 7. For this simulation case a 2P vortex shedding pattern is identified. The Q-criterion iso-surface colored by z-vorticity shows two closely spaced positive and negative vorticity zones that are shed every half-cycle of vibration, which represents two vortices rotating in opposite direction. It is also observed that the secondary vortex in each pair is weaker and smaller.

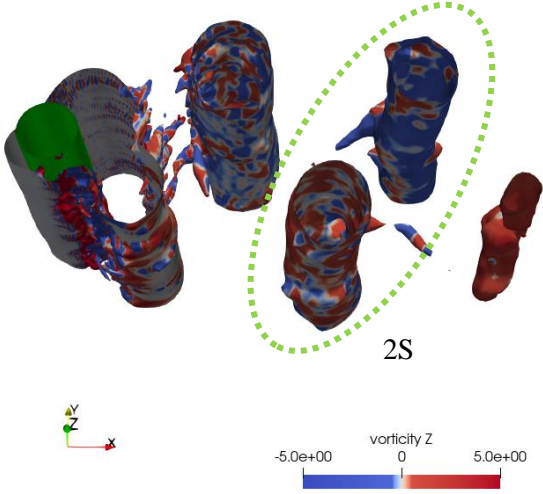


Figure 38: Iso-surface of pressure coefficient ($C_p = -0.25$) colored by spanwise vorticity for $Ur4$ at $tU/D = 130$.

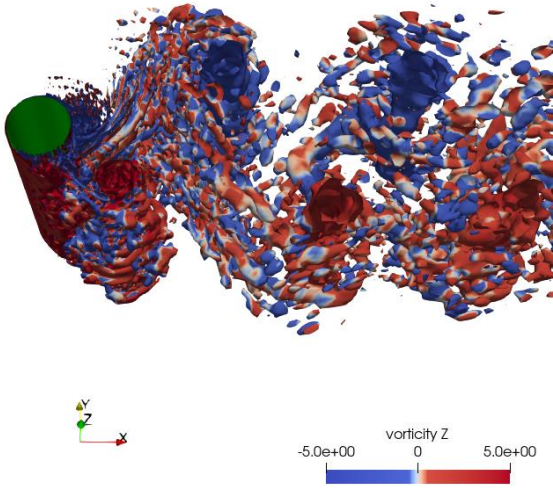


Figure 39: Iso-surface of Q-criterion ($Q = 1$) colored by spanwise vorticity for $Ur4$ at $tU/D = 130$.

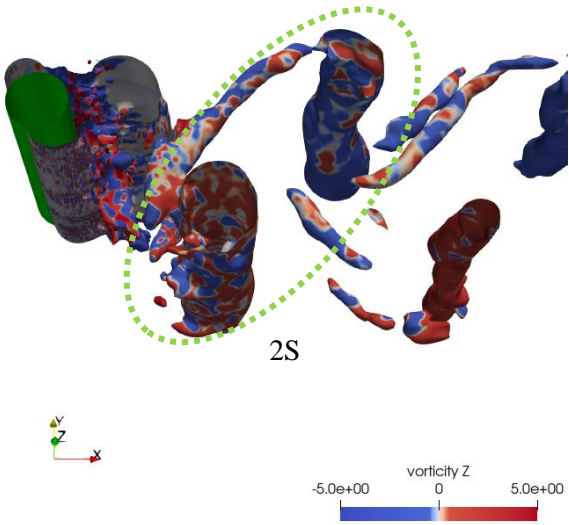


Figure 40: Iso-surface of pressure coefficient ($C_p = -0.25$) colored by spanwise vorticity for $Ur 5$ at $tU/D = 140$.

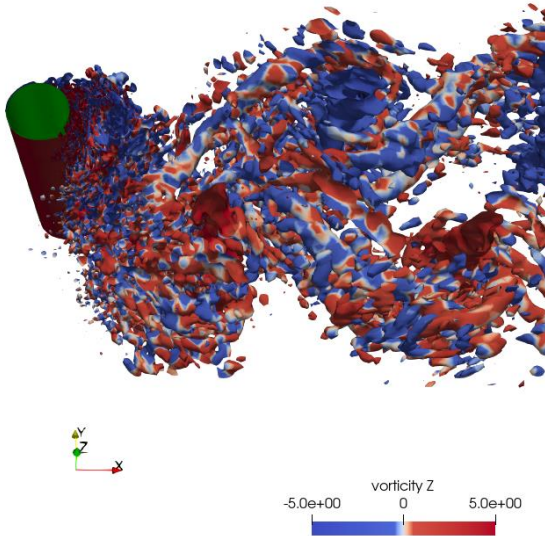


Figure 41: Iso-surface of Q-criterion ($Q = 1$) colored by spanwise vorticity for $Ur 5$ at $tU/D = 140$.

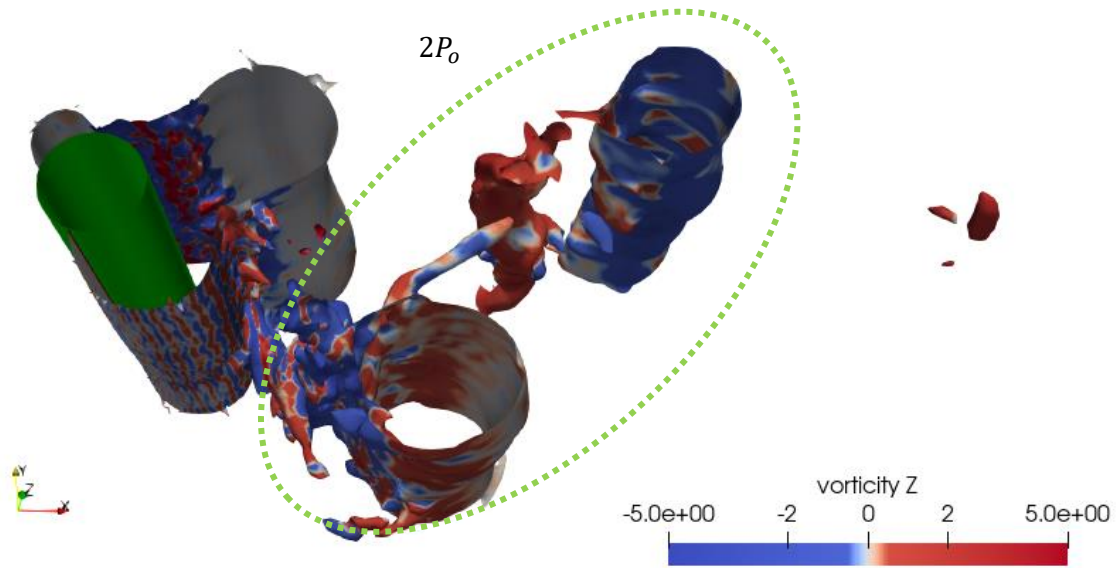


Figure 42: Iso-surface of pressure coefficient ($C_p = -0.2$) colored by spanwise vorticity for Ur 5 at $tU/D = 19.6$.

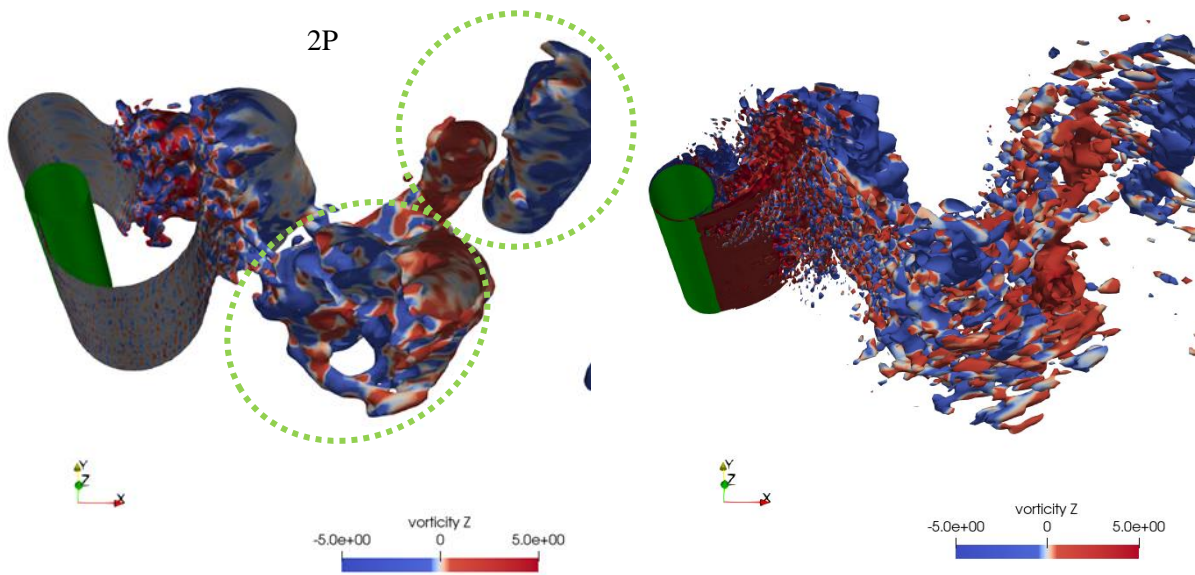


Figure 43: Iso-surface of pressure coefficient ($C_p = -0.1$) colored by spanwise vorticity for Ur 7 at $tU/D = 160$.

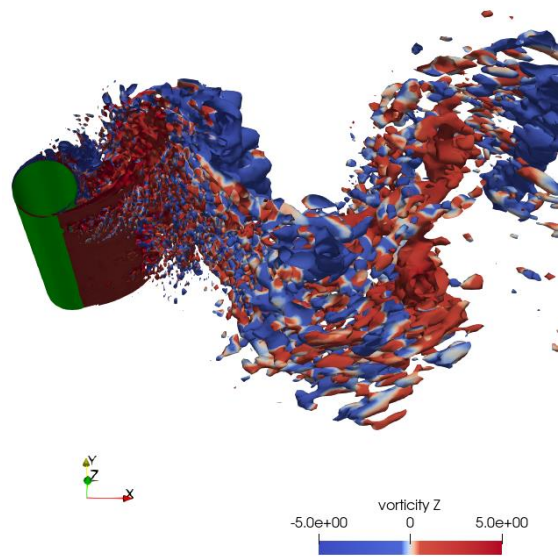


Figure 44: Iso-surface of Q-criterion ($Q = 1$) colored by spanwise vorticity for Ur 7 at $tU/D = 160$.

The vortex shedding modes are dependent on the cross-flow displacement and Ur . In the self-excited oscillations, the displacement signal is not perfectly sinusoidal, hence both the maximum observed amplitude and *RMS* displacement are computed for the investigated cases. The values of the

displacements are shown in Table 4, the maximum displacement is taken from the entire time series and, therefore, includes the buildup phase of the simulation. The cross-flow displacements found in the present simulations are plotted in the map of vortex shedding regimes proposed by Morse and Williamson (2009) based on their forced oscillation tests and observed vortex patterns (Figure 45). Based on the map of vortex shedding regimes we can confirm the 2S shedding mode for the simulation case at Ur 4 and Ur 5. The max displacement of the Ur 5 simulation is close to the $2P_0$ shedding regime which confirms the $2P_0$ shedding mode that was discovered during the buildup of the flow. The simulation case with Ur 7 is well in the region of the 2P shedding regime which confirms our finding for this simulation.

Table 4: Summary of root-mean-square and maximum cross-flow displacement obtained in present simulations.

Simulation case	Displacement ($y/D \text{ RMS} * \sqrt{2}$)	Max Displacement
Ur 4	0.736	0.762
Ur 5	0.669	0.726
Ur 7	0.540	0.658

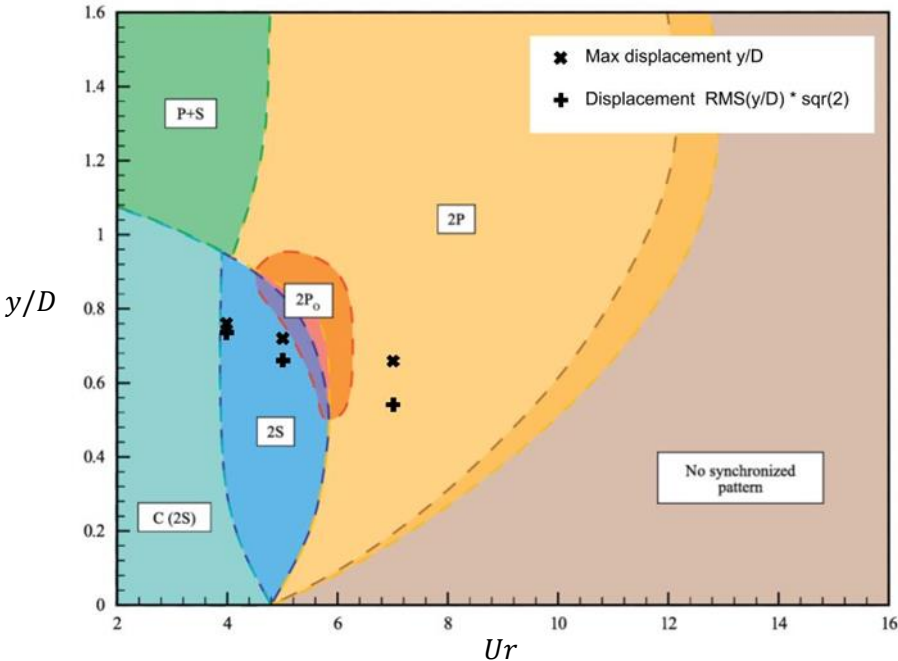


Figure 45: Map of vortex shedding modes from Morse and Williamson (2009) at $Re = 4000$ with superposed results from the present study.

5.1 Two-Point Correlations in the Wake

The wake flow behind the cylinder at $Re = 3900$ is not uniform in the spanwise direction as shown in the figures 47,48 and 49. An effective way of quantifying the three-dimensionality of the wake flow is

by calculating the spatial correlation of flow variables. The correlation coefficient, $R(z)$, is a measure of strength and direction of a linear relationship between two random variables:

$$R(z) = \frac{\overline{\sum \sigma'(\zeta)\sigma'(\zeta + z)}}{\sqrt{\overline{\sum [\sigma'(\zeta)]^2}}} \quad (5-1)$$

where z is the spanwise distance between two measuring points, ζ is the spanwise location, σ' is the fluctuating random flow variable. The overbar denotes the time average. For calculating the correlation coefficient, the fluctuating pressure p' is used as the random variable σ' in Eq. 2-1. The contour maps presented in Figure 46. show the vertical variation of $R(z)$ calculated between the midspan ($z = 2.0$) and spanwise separation (Δz) plotted on a 2D plane normal to the flow direction. A set of planes with different streamwise positions in the wake is selected to show the variation of spatial correlation of the flow. $R(z)$ is averaged over five full shedding cycles (corresponding to approximately $\frac{tU}{D} = 19$ dimensionless time units).

General observation apparent for all the investigated plane positions and Ur is a gradual decrease of $R(z)$ values with Δz . In the immediate proximity to the cylinder, at $x = 1.0D$ (Figure 46(a-c)), the $R(z)$ values decrease in a relatively wide zone spanning approximately $\Delta y = 5D$ across the wake centerline. At $Ur 5$ the extent of the low-correlation zone is the largest among the investigated cases, followed by the case of $Ur 7$ and $Ur 4$, respectively. Further downstream, at $x = 2.0D$ (Figure 46(d-f)), the rate at which $R(z)$ drops with spanwise separation is greatly increased as compared to the observations made at $x = 1D$. This indicates that at $x = 2D$ there is significantly more flow disturbances than in the immediate proximity to the cylinder which can be explained by the transition to turbulence in the separated shear layers. In the subcritical range of Reynolds number, the near wake of the cylinder is surrounded by initially laminar free shear layers. The shear layers for the different Ur can be seen in the figures 47,48 and 49 which show isometric plots of the Q-criteria for $Ur 4$, $Ur 5$ and $Ur 7$ respectively. The transition to turbulence occurs before the free shear layers roll up into the wake vortices. The secondary instabilities in the free shear layers in the form of Gerrard-Bloor transition waves emanate as eddy filaments which become more irregular further downstream. In the case of $Ur 4$ the flow in the wake becomes uncorrelated in a wide zone measuring approximately $\Delta y = 6D$. Similar extent of the flow disturbance zone is observed for the case of $Ur 5$. Here the flow is highly uncorrelated close to the wake centerline ($y = 0$). For the case of $Ur 7$ the flow disturbance zone is narrower in comparison to the cases of $Ur 4$ and $Ur 5$, measuring approximately $\Delta y = 4D$. Figure 47(a) suggests that possible explanation of the increased correlation for the $Ur 4$ case is that at $x = 4D$ the vortex street is wide, but vortices are not stretched significantly and secondary instabilities are not developed strong enough to affect the fluid close to the centerline.

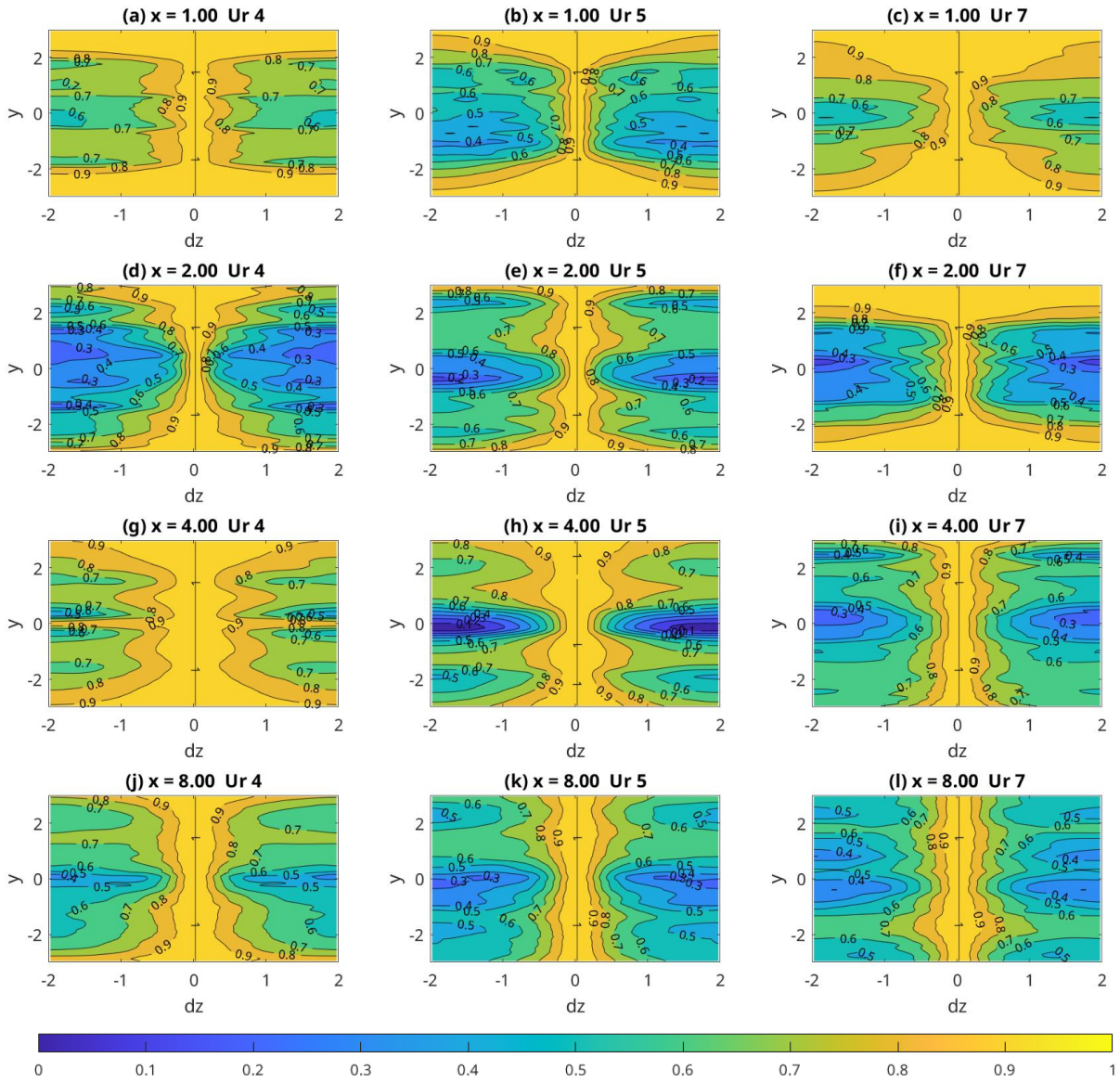


Figure 46: Spanwise correlation coefficient distribution $R(z)$ in the wake of the cylinder for different streamwise locations (x) and different reduced velocities (Ur); (a, d, g, j) $Ur 4$; (b, e, h, k) $Ur 5$; (c, f, i, l) $Ur 7$; (a, b, c) $x = 1$; (d, e, f) $x = 2$; (g, h, i) $x = 4$; (j, k, l) $x = 8$.

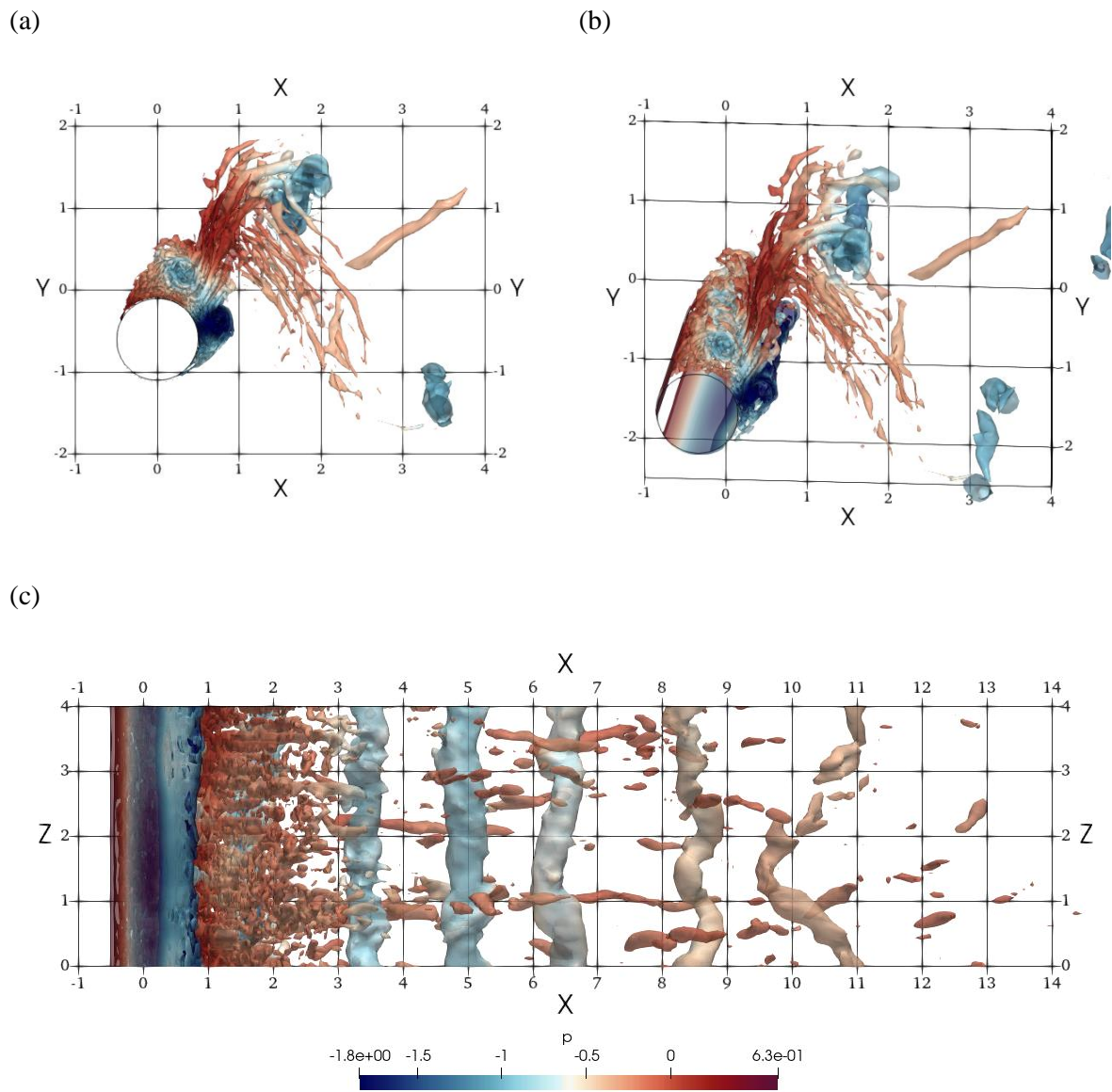
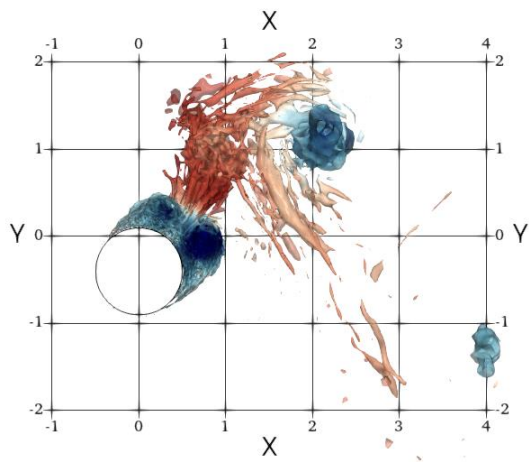
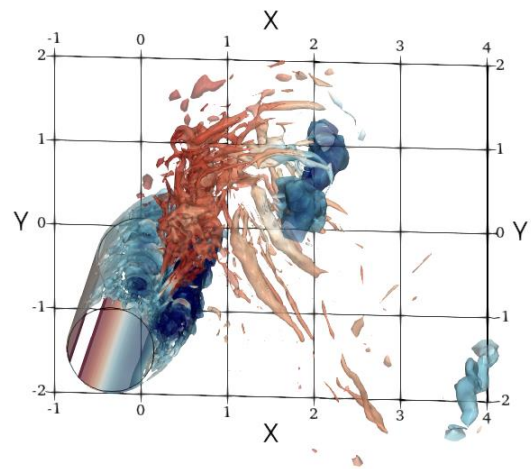


Figure 47: Iso-surface of Q-criterion colored by pressure for $Ur = 4$ at $\frac{tU}{D} = 100$: (a,b) $Q = 10$; (c) $Q = 3$.

(a)



(b)



(c)

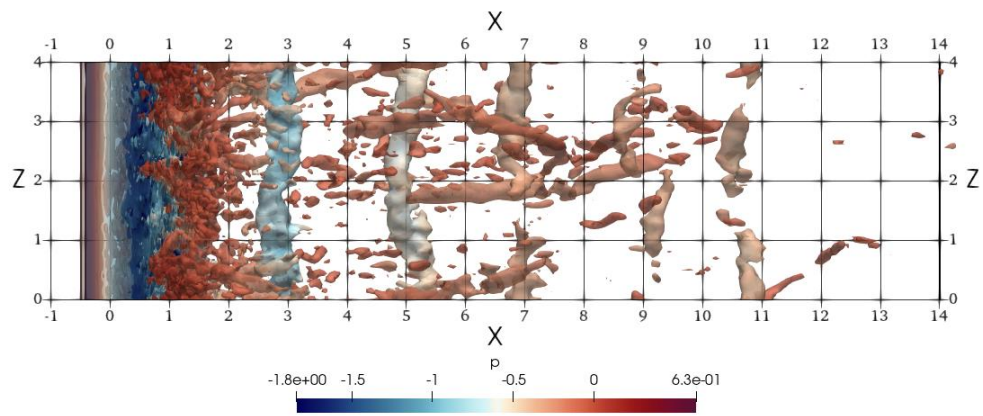
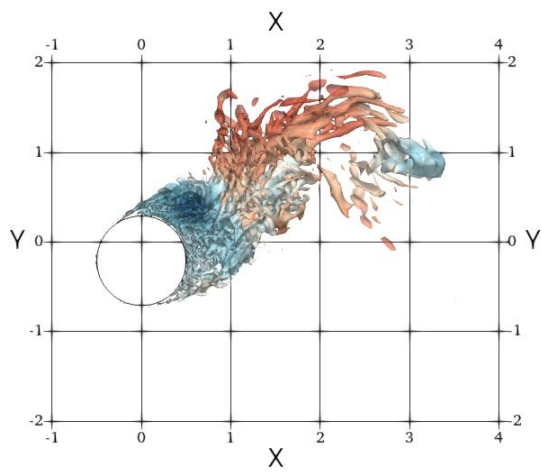
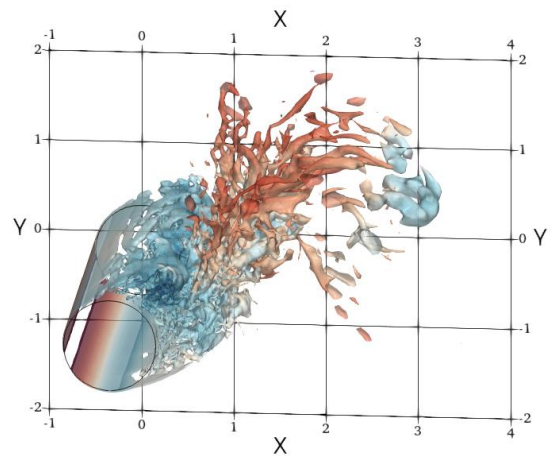


Figure 48: Iso-surface of Q-criterion colored by pressure for Ur 5 at $\frac{tU}{D} = 40$: (a,b) $Q = 10$; (c) $Q = 3$.

(a)



(b)



(c)

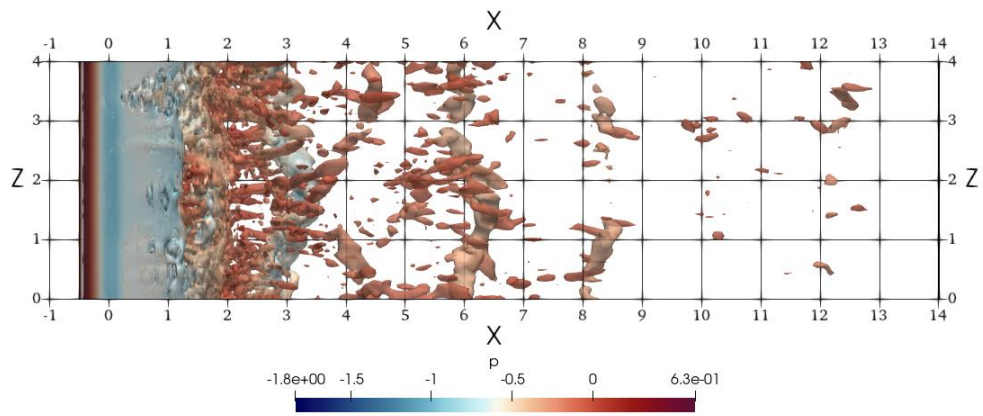


Figure 49: Iso-surface of Q-criterion colored by pressure for $Ur = 7$ at $\frac{tU}{D} = 160$: (a,b) $Q = 10$; (c) $Q = 3$.

5.2 Proper Orthogonal Decomposition

The Proper Orthogonal Decomposition (POD) is a technique that extracts the basis for a modal decomposition from an ensemble of a random vector field (Berkooz et al., 1993). The technique of POD was first proposed by Lumley (1967) in the context of turbulence studies. In fluid mechanics POD is frequently employed to decompose the time dependent flow into spectral modes which can be used to identify the dominant, energy containing, coherent structures in the flow. The major advantage of the POD is the fact that it is a linear procedure. The time dependent variables $q(\chi, t)$, where χ denotes the coordinates and t is the time, are decomposed into spectral modes, $\phi_j(\chi)$, and their temporal coefficients, $a_j(t)$, in the following way:

$$q(\chi, t) = \sum_j a_j(t) \phi_j(\chi) \quad (5-2)$$

In the POD algorithm the sampled data is arranged in the Matrix M consisting of vectors V_1^n containing the cartesian components of a random vector field.

$$M = V_1^n = [v_1, v_2, \dots, v_n] \quad (5-3)$$

Applying the Singular Value Decomposition (SVD) on the matrix M gives the POD modes

$$M = U \Sigma V^T \quad (5-4)$$

where V and U are, respectively, the right and left singular vectors of M , and Σ denotes the diagonal matrix. The matrix U contains the POD modes $\phi_j(\chi)$ in column vectors and the matrix V contains the temporal coefficients $a_j(t)$. Both U and V are orthogonal matrices.

$$U^T U = I \quad (5-5)$$

$$V^T V = I \quad (5-6)$$

Σ contains the singular values of the matrix M ($\Sigma = \text{diag}(\lambda_1, \lambda_2, \lambda_3 \dots \lambda_n)$) where each diagonal value represents energy of each POD mode.

$$\lambda_1 > \lambda_2 > \lambda_3 > \dots > \lambda_n > 0 \quad (5-7)$$

To reduce the computational load the economy-size SVD algorithm is used (Anderson, et al. 1999). In the economy-size SVD, for a rectangular matrix $M_{m \times n}$ with $m > n$ only the first n columns from the left singular vectors are calculated which results in the reduced matrix Σ with $n \times n$ dimensions.

In the present study the POD is performed on data vector containing the three orthogonal components of the velocity field. For the analyses of the turbulent wake of a vibrating cylinder the POD is carried out on data sampled from the cylinder's wake for three cases with different Ur . A set of 2D planes normal to the flow direction and one plane normal to the spanwise direction are used to formulate the POD basis. The location of sampling planes is showcased in Figure 50. The sampling interval is set to $\Delta t U/D = 0.02$ which corresponds to every 10th time step in the present CFD simulations.

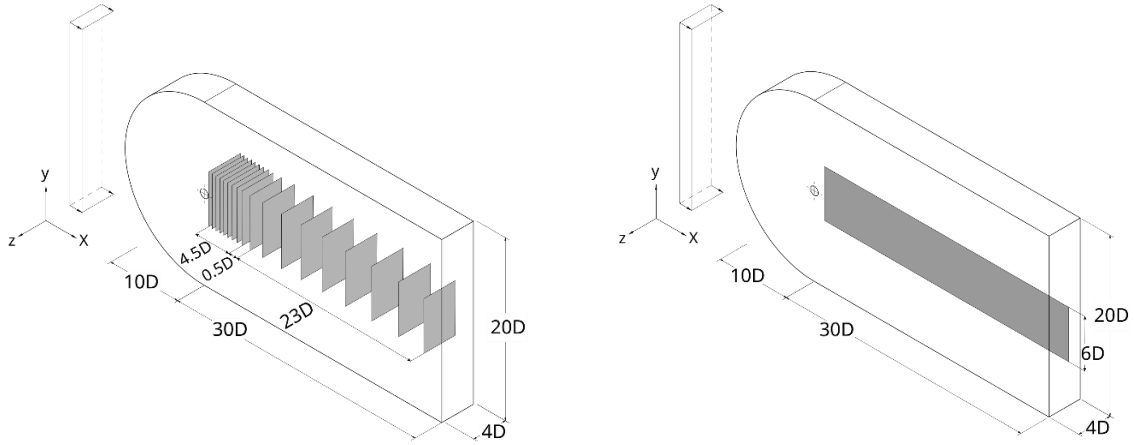


Figure 50: Schematic of the data sampling planes locations in the computational domain, (a) XZ-planes, (b) XY-plane.

To ensure that the results of the POD analysis are independent of the sampling time interval and the number of snapshots a convergence study is performed based on a method proposed by Muld et al. (2012). According to Muld et al. (2012), the scalar product of two leading POD modes of different sampling time (T_A) must be 1 for full convergence. The scalar product of between the leading POD modes is define as

$$\varepsilon_{ortho} = \langle \phi_{j,1}, \phi_{j,2} \rangle \quad (5-8)$$

Where j denotes the number of the mode and 1,2 denote the samples with different sampling time. The POD mode with the smallest sampling time ($T_A = 0.02$) is used as a reference. Figure 51 shows the mean of ε_{ortho} from the XY plane at Ur 4 for the 10 most energetic modes. All values of ε_{ortho} are close to 1 and the difference for $T_A = 0.04$ and $T_A = 0.08$ only show minimal divergence from the reference calculation with $T_A = 0.02$, this indicates a sufficient convergence.

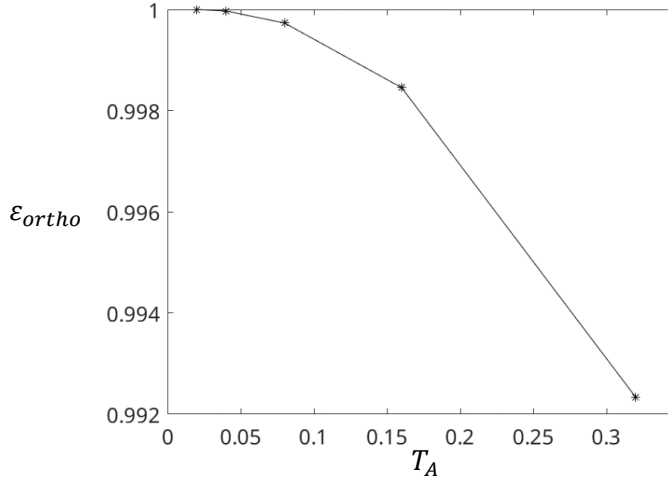


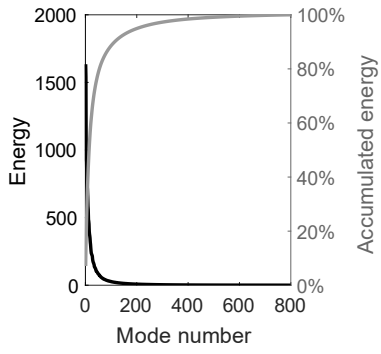
Figure 51: The mean value of E_{ortho} of the first ten most energetic evaluated for POD analysis with different sampling time intervals.

5.2.1 POD mode distribution on XY-plane

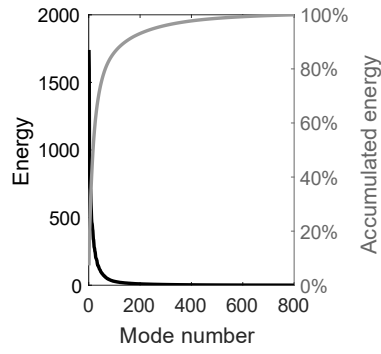
Modal decomposition of the turbulent wake for three different values of Ur is presented on the spanwise plane located in the axis of symmetry of the cylinder. Figure 52 shows the fluctuating kinetic energy of each mode and cumulative fluctuating kinetic energy of all 800 POD modes for Ur 4, Ur 5 and Ur 7. To capture 90% of the energy of the flow the 114, 142 and 82 first most energetic modes are required for Ur 4, Ur 5 and Ur 7, respectively. The number of modes required to capture 99% of the energy increases to 482 (Ur 4), 544 (Ur 5) and 303 (Ur 7). Figure 53 presents the energy contribution of the leading 20 POD modes for Ur 4, Ur 5 and Ur 7. The POD modes come in pairs of similar energy. There is a large separation between the energy of the first two leading modes which contribute nearly double the amount of energy than the higher order modes. Modes 1 and 2 have energy contribution of 9% to 6.6% while higher modes contribute 4% or less. A large amount of modes is required to accurately reconstruct the flow field but due to the high energy contribution of the first 2 modes only a few leading nodes are required to reconstruct the main vortex shedding mechanism. Time coefficients (a_i) and power spectral density ($PSD_{(a_i)}$) of time coefficients for the first two leading modes are shown in the figures 56, 59 and 60 for Ur 4, Ur 5, and Ur 7, respectively. The frequency of time coefficients for the first two leading modes is coincident with the Strouhal frequency for all investigated Ur . The time coefficients shown in figures 56(a), 59(a) and 60(a) are shifted in phase. The phase portraits shown in Figure 57 are close to a circle which indicates a phase shift of approximately 90° (a quarter wavelength). Furthermore, the amplitudes of the time coefficients are similar which indicates a traveling wave. The two leading modes are typically associated with the largest, energy containing coherent structures which in the present cases correspond to the primary vortex street. The spatial distributions of POD modes with frequencies close to the fundamental frequency of cylinder vibration for all investigated Ur are shown in Figure 54. The development and characteristics of the dominant coherent structures in the wake can be better understood from the analysis of the decomposition of the velocity fields. For the sake of brevity, we will denote n-th POD mode as Φ_n henceforth. There is a general similarity between the spatial patterns of the two leading POD modes for all the investigated Ur . The structure of the u-

component for Φ_1 and Φ_2 is antisymmetric about the x-axis and can be associated with periodically shed vortices. The aforementioned overlap between the vortex shedding frequency and frequencies of a_1 and a_2 support this statement. The structure of the v-component for Φ_1 and Φ_2 is symmetric about the x-axis and represents the transverse movement of the fluid in the cylinder's wake driven by the alternating vortex street. Both Φ_1 and Φ_2 satisfy the requirements to be considered as a representation of coherent motion which are: similar turbulent kinetic energy, clearly observable circular relationship in phase space and phase shift by a quarter wavelength. They can, therefore, be named as the first dynamic mode pair. Similar dynamic mode pairs can be found among the higher order modes which contain significant frequency content at $f/St = 2$. The second harmonic dynamic mode pairs are presented in Figure 55. The second harmonic appears for different mode numbers for the respective cases of Ur considered in the present study. The phase portraits of the second harmonic mode pairs, shown in Figure 58, are more chaotic than the phase portraits for the first harmonic mode pairs. But the phase portraits still follow circular orbits which is indicating a phase shift of approximately a quarter wavelength. For Ur 4 the pair of second harmonic modes are Φ_7 and Φ_8 which have a slightly lower energy contribution than Φ_3 - Φ_6 which have a chaotic structure. The flow pattern shows an antisymmetric behavior and there is a quarter wavelength phase shift in the time coefficient which can be seen in Figure 56 (b) which indicates a travelling wave, this is similar to the behavior of the first harmonic mode pair. For Ur 5 (Figure 55(c,d)) the second harmonic mode pair appears on Φ_5 and Φ_6 . They show in comparison to the second harmonic mode pair of Ur 4 a less clear flow pattern. However the flow pattern can be identified as asymmetric. There is a phase shift in the time coefficients which can be seen in Figure 59(b). However, the power spectra of Φ_6 shows an overlining secondary frequency peak at $0.5f/St$ which can explain the less clear pattern compared to the case at Ur 4. Similar to the first harmonic mode and Ur 4 the asymmetric pattern and the phase shift indicate a traveling wave. The second harmonic for Ur 7 is appearing on Φ_3 and Φ_4 . The flow patterns in Figure 55(e,f) show an antisymmetric pattern and the time coefficients (Figure 60(b)) show a phase shift of a quarter wave length. This indicates a traveling wave in the same way as for the second harmonic mode pairs for Ur 4 and Ur 5. For all Ur the flow patterns for the second harmonic mode pair is symmetric with respect to the center line for the u-component and antisymmetric for the v-component. The flow structure of the w-component shows no clear pattern and is mostly chaotic, however for the case with Ur 4 a small symmetric pattern can be identified close to the cylinder.

(a) *Ur 4*



(b) *Ur 5*



(c) *Ur 7*

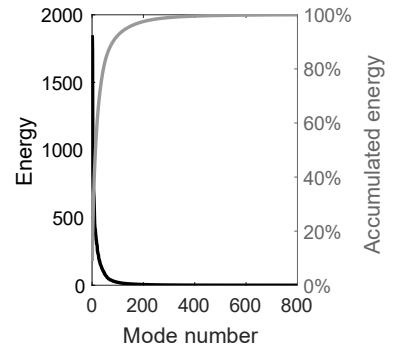
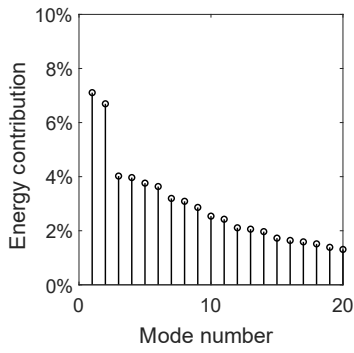
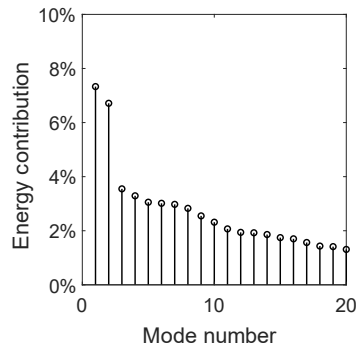


Figure 52: Energy and accumulated energy of POD modes on *XY* plane; (a) *Ur 4*; (b) *Ur 5*; (c) *Ur 7*

(a) *Ur 4*



(b) *Ur 5*



(c) *Ur 7*

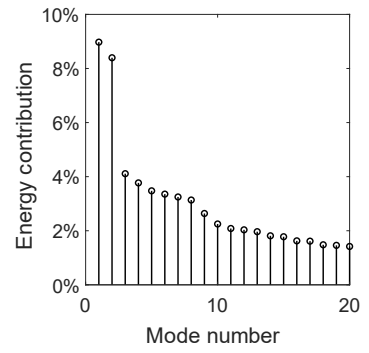


Figure 53: Energy contribution of the first 20 POD modes on *XY* plane; (a) *Ur 4*; (b) *Ur 5*; (c) *Ur 7*

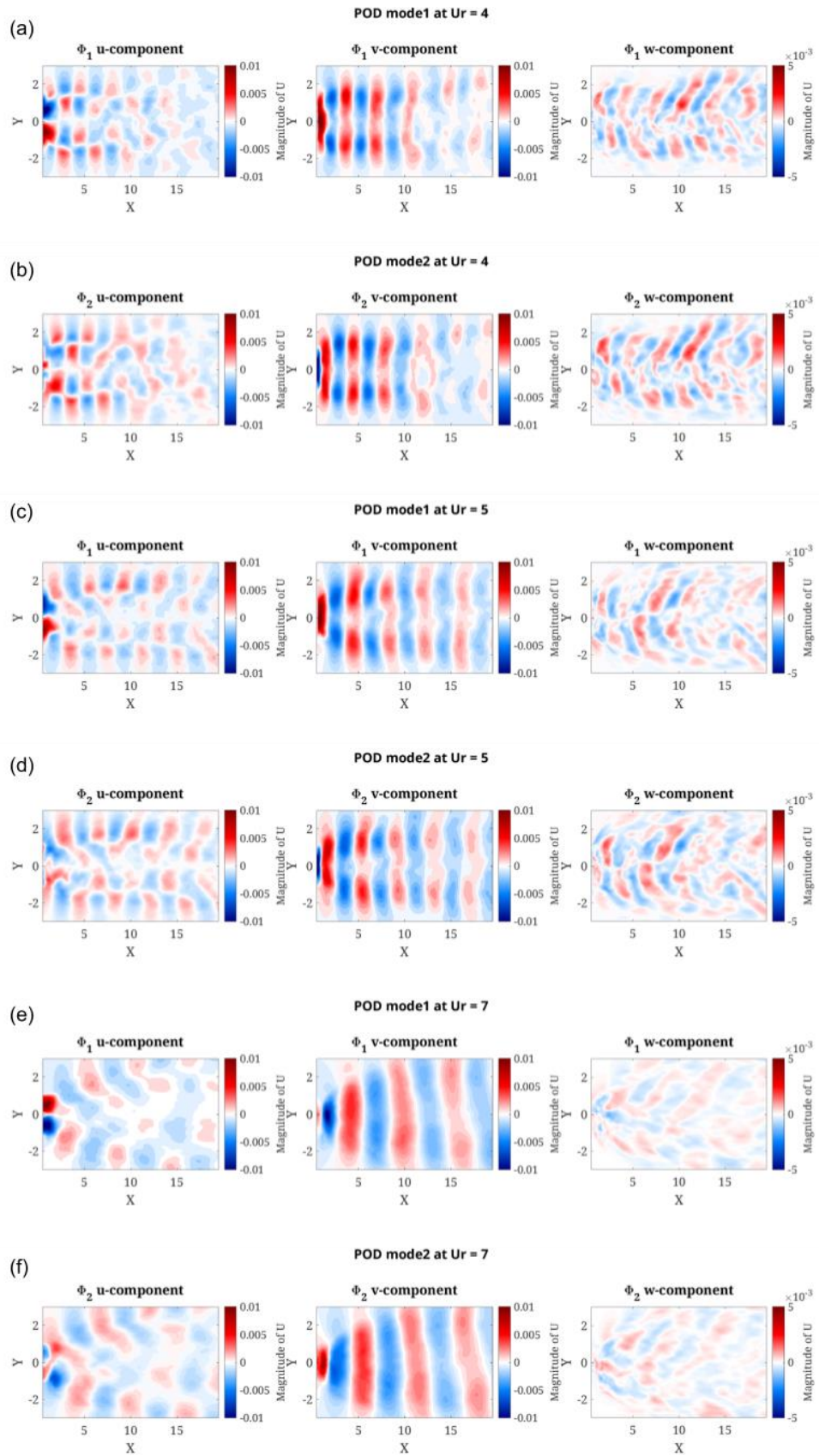


Figure 54: Spatial structure of two leading POD modes: (a, b) Ur 4; (c, d) Ur 5; (e, f) Ur 7

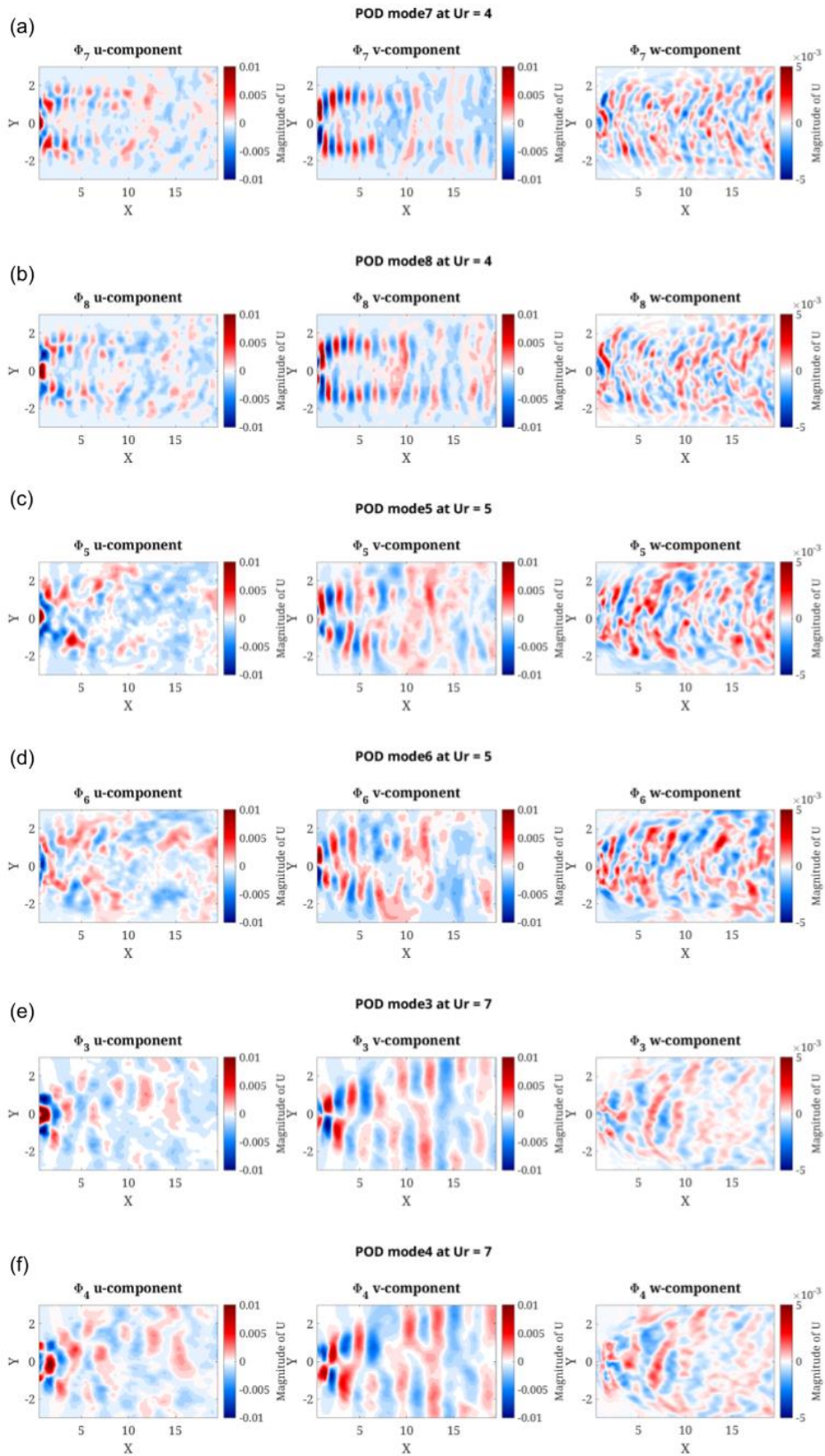


Figure 55: second super harmonic shedding POD modes: (a,b) Ur 4; (c,d) Ur 5; (e,f) Ur 7; (a) mode 7; (b) mode 8; (c) mode 5; (d) mode 6; (e) mode 3; (f) mode 4

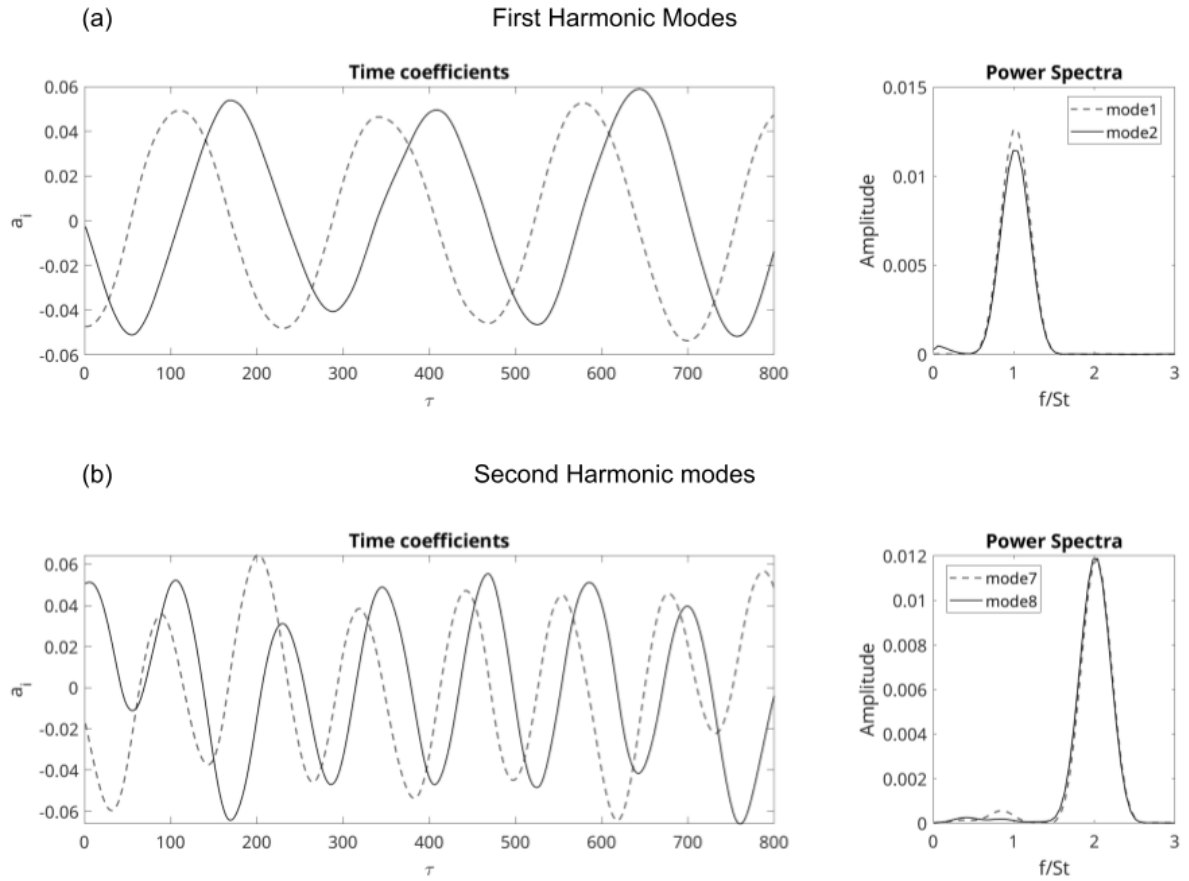


Figure 56: Time coefficient and power spectra for harmonic mode pairs on the XY plane for Ur 4: (a) first harmonic mode pair; (b) second harmonic mode pair.

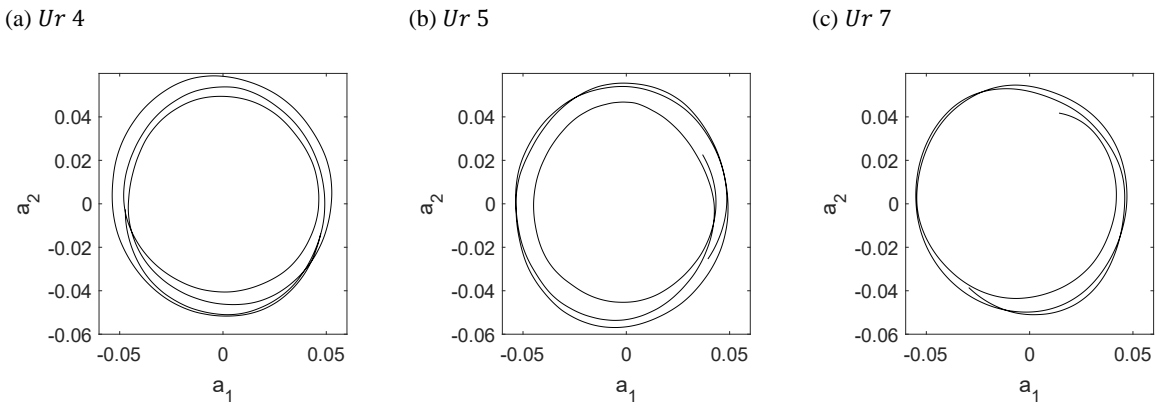
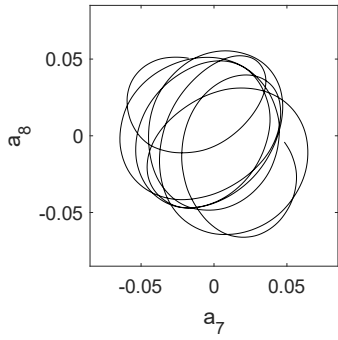
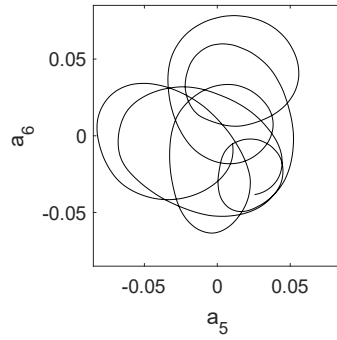


Figure 57: Phase portraits of the time coefficients for the first two most energetic POD modes on the XY plane for Ur 4 (a); Ur 5 (b); Ur 7 (c).

(a) *Ur* 4



(b) *Ur* 5



(c) *Ur* 7

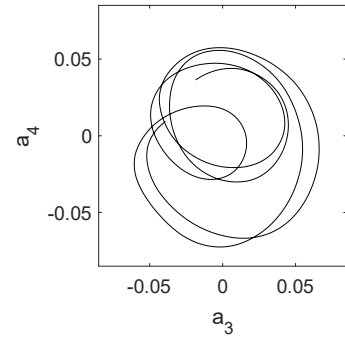


Figure 58: Phase portraits of the time coefficients for the second super harmonic shedding POD modes on the *XY* plane for: *Ur*4 (a); *Ur*5 (b); *Ur*7 (c).

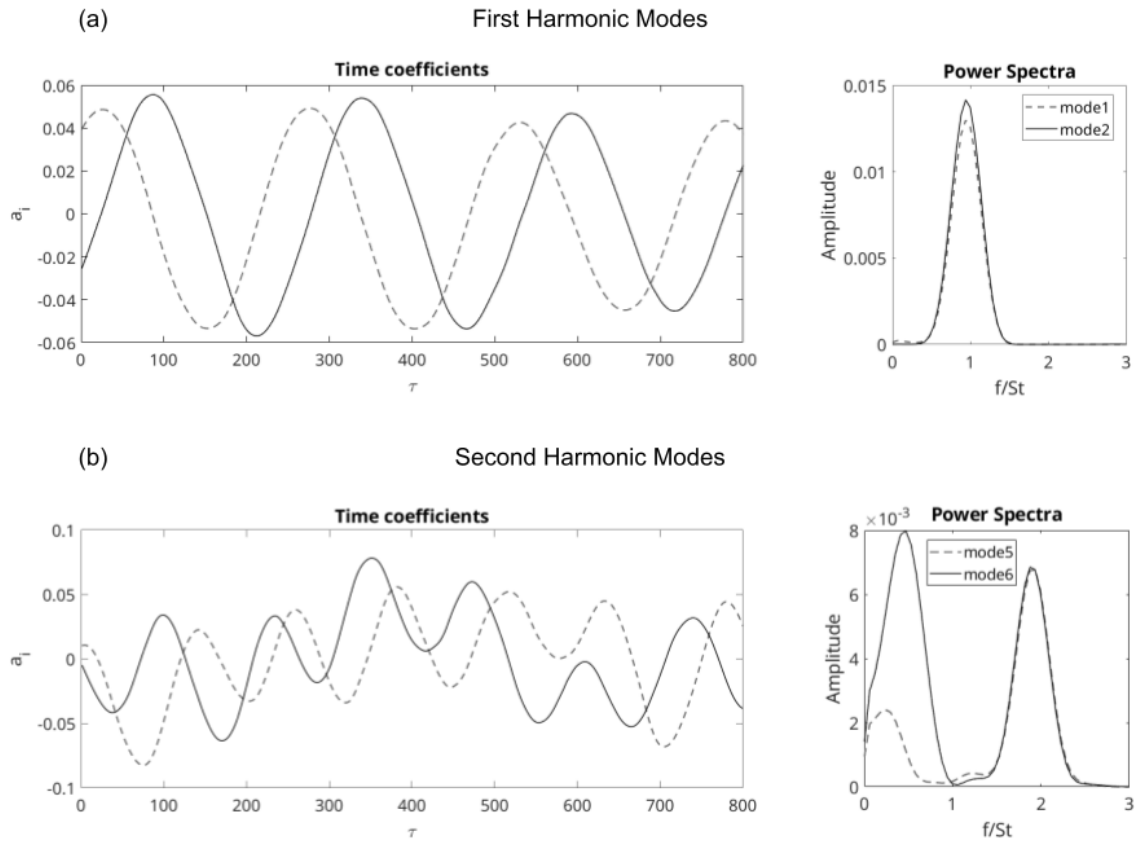


Figure 59: Time coefficient and power spectra for harmonic mode pair on *XY*-plane for *Ur* 5: (a) first harmonic mode pair; (b) second harmonic mode pair.

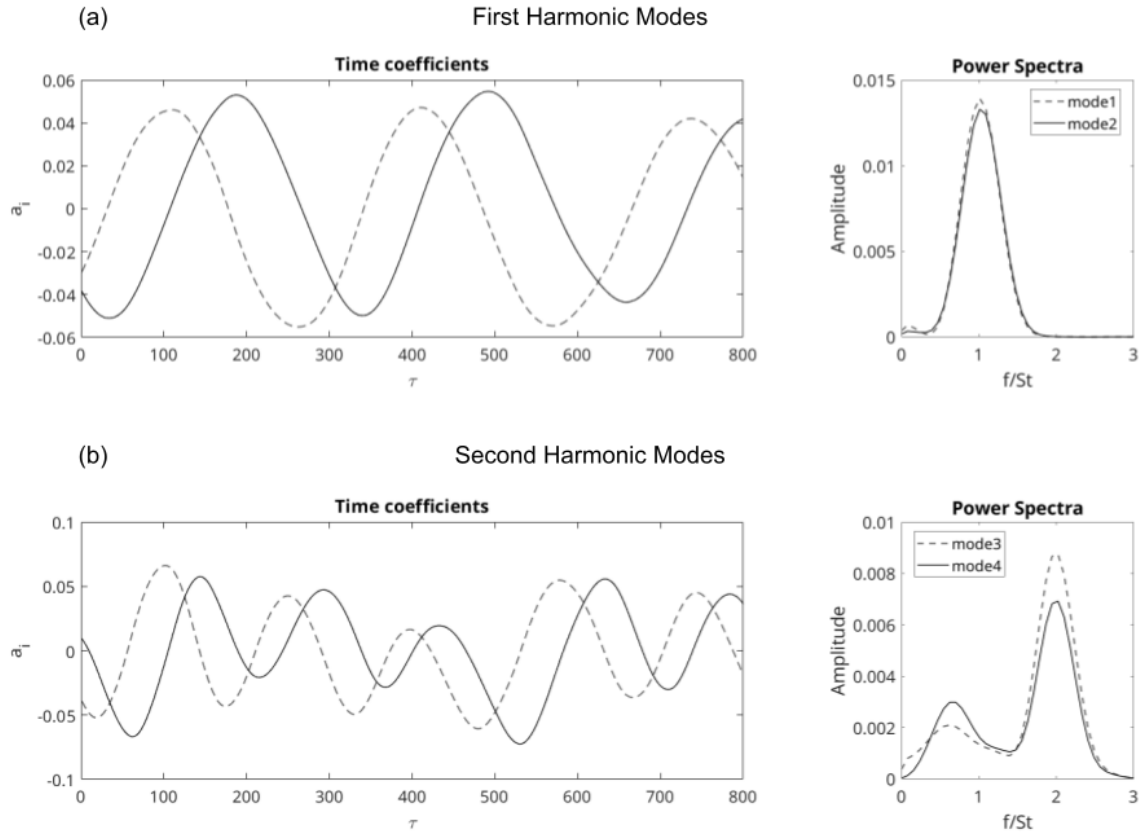


Figure 60: Time coefficients and power spectra for harmonic mode pair on XY-plane for Ur 7: (a) first harmonic mode pair; (b) second harmonic mode pair.

5.2.2 POD mode distribution on YZ-planes

To further study the wake dynamics POD is performed on multiple planes normal to the flow direction (YZ-planes) distributed downstream the cylinder. The most representative locations are chosen for the analysis which are located at distances $x = [0.5, 1, 2, 4, 6, 8]D$ measured from the center of the cylinder.

5.2.2.1 Ur 4

The energy and accumulated energy for full set of POD modes is shown in the Figure 67 and the energy contribution of the leading 20 modes is shown in Figure 68. For locations close to the cylinder a larger number of POD modes is required to capture a sufficient percentage of the total amount of the energy, compared to locations further downstream. For a distance of $x = 1D$ the first 200 modes capture less than 85% of the energy (Figure 67(b)) while at a the distance of $x = 6D$ the first 200 modes capture close to 100% of the energy (Figure 67(e)). The total amount of energy that is captured by the POD analyses decreases with an increasing distance to the cylinder. The first most energetic mode contributes between 7.4% and 12.6% of the energy at the different distances to the cylinder. With the highest energy contribution at the sampling plane at $x = 4D$. The main difference between the distribution of mode energy for the XY-plane and the YZ-planes is the lack of apparent mode pairing; i.e. consecutive modes do not appear in pairs with similar energy.

Figures 61 and 62 show the spatial distribution of the u-component for the modes 1 to 8 and figures 63 and 64 show the spatial distribution of the v-component for the modes 1 to 8. For mode 1 the v-component has the highest magnitude (Figure 63(a)) while mode 2 shows the highest magnitude for the u-component (Figure 61(b)). The first mode is dominated by the v-component while the second mode is dominated by the u-component this is independent of the distance to the cylinder. Therefore, most energy is included in the v-component. For the first harmonic mode pair the flow pattern of the u-component is antisymmetric, and the v-component is symmetric around the centerline. For the second harmonic the u-component is symmetric, and the v-component is antisymmetric. This is the same behavior as for the *XY*-planes. The first harmonic pod modes show a symmetric pattern for the v-component while the second harmonic is symmetric in the u-component. Figures 65 and 66 show the spatial distribution of the w-component for the modes 1 to 8. For the w-component of mode 1 (Figure 65(a)) it can be seen that at a location close to the cylinder ($x = 0.5D$) there are 4 cells of vortex formation, this structure brakes apart and is unregular for $x = 1.5D$. Further downstream at $x = 4D$ there is a clear mode structure again with 2 cells.

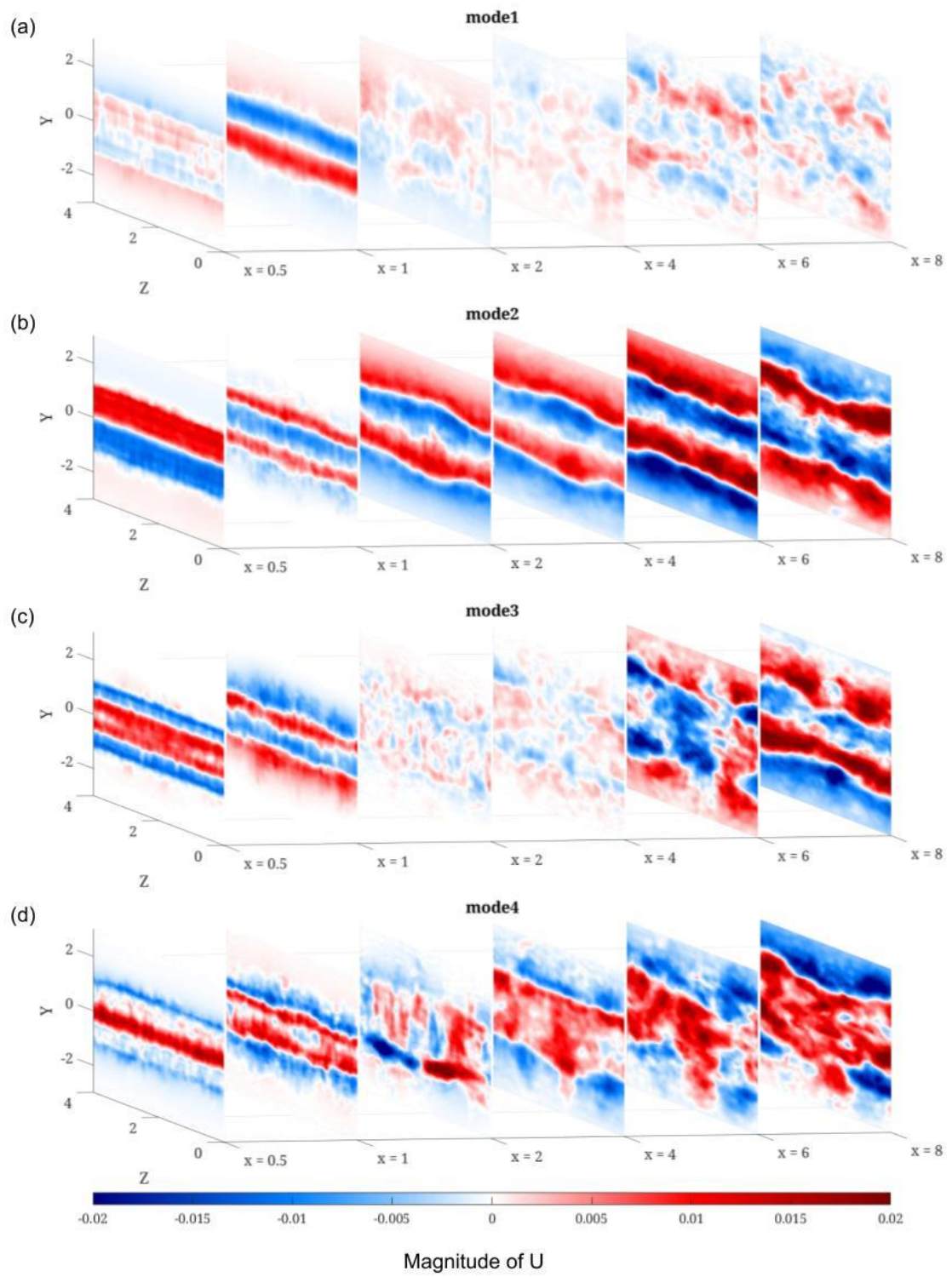


Figure 61: Φ_3 u-component of the POD modes at different x locations for $Ur 4$: (a) mode 1; (b) mode 2; (c) mode 3; (d) mode 4.

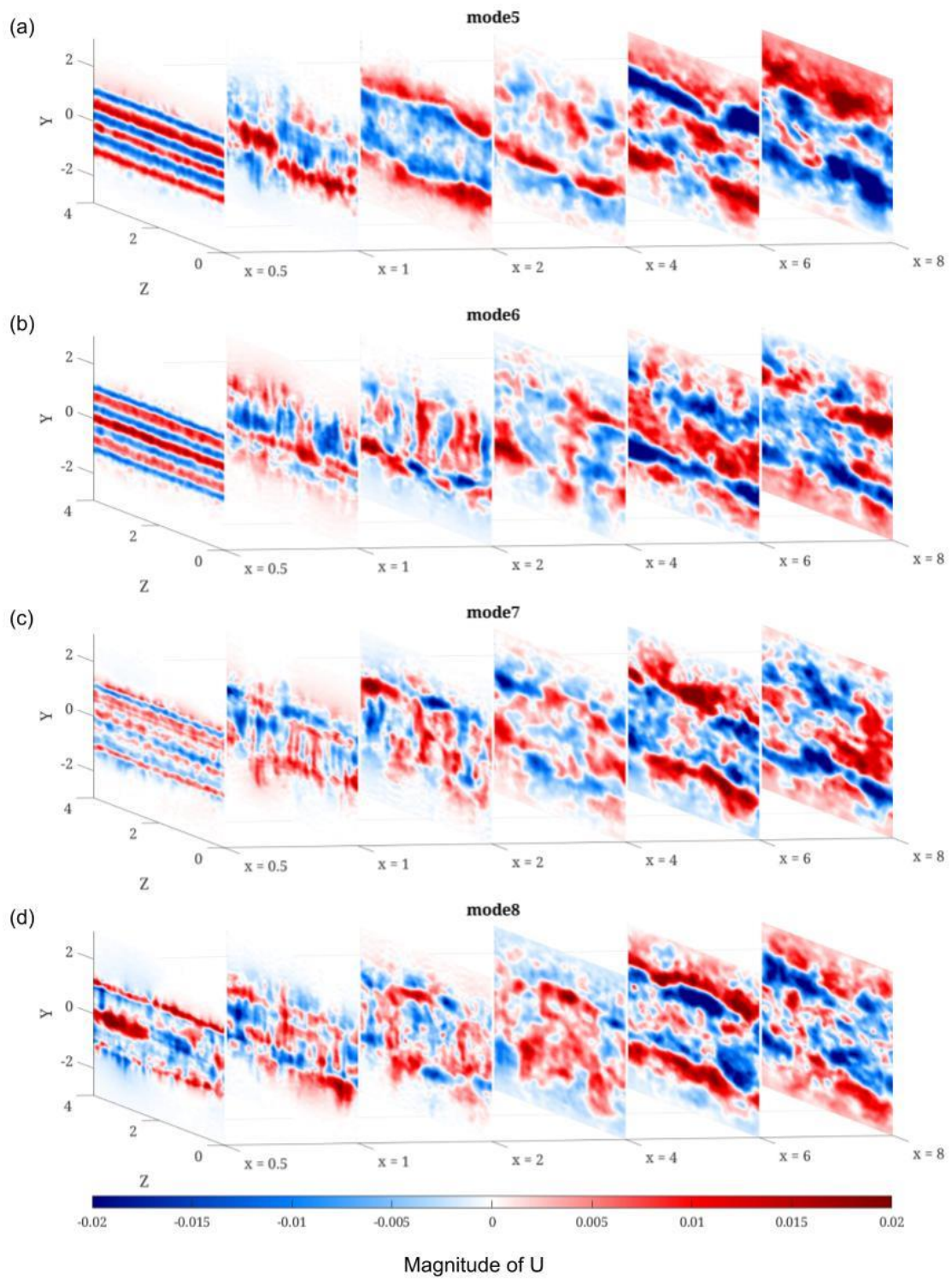


Figure 62: Φ_3 u-component of the POD modes at different x locations for $Ur = 4$: (a) mode 5; (b) mode 6; (c) mode 7; (d) mode 8.

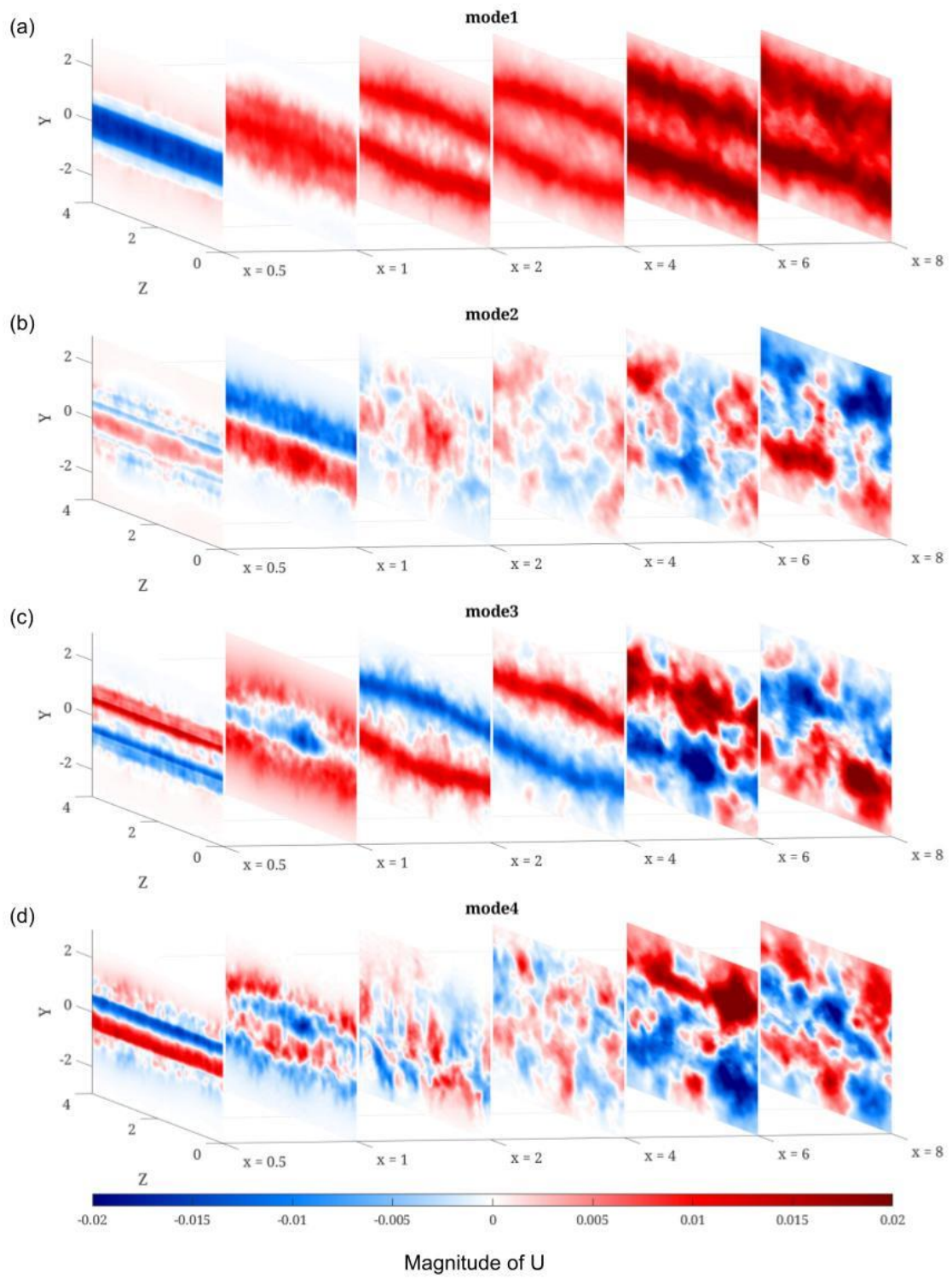


Figure 63: Φ_3 v-component of the POD modes at different x locations for $Ur = 4$: (a) mode 1; (b) mode 2; (c) mode 3; (d) mode 4.

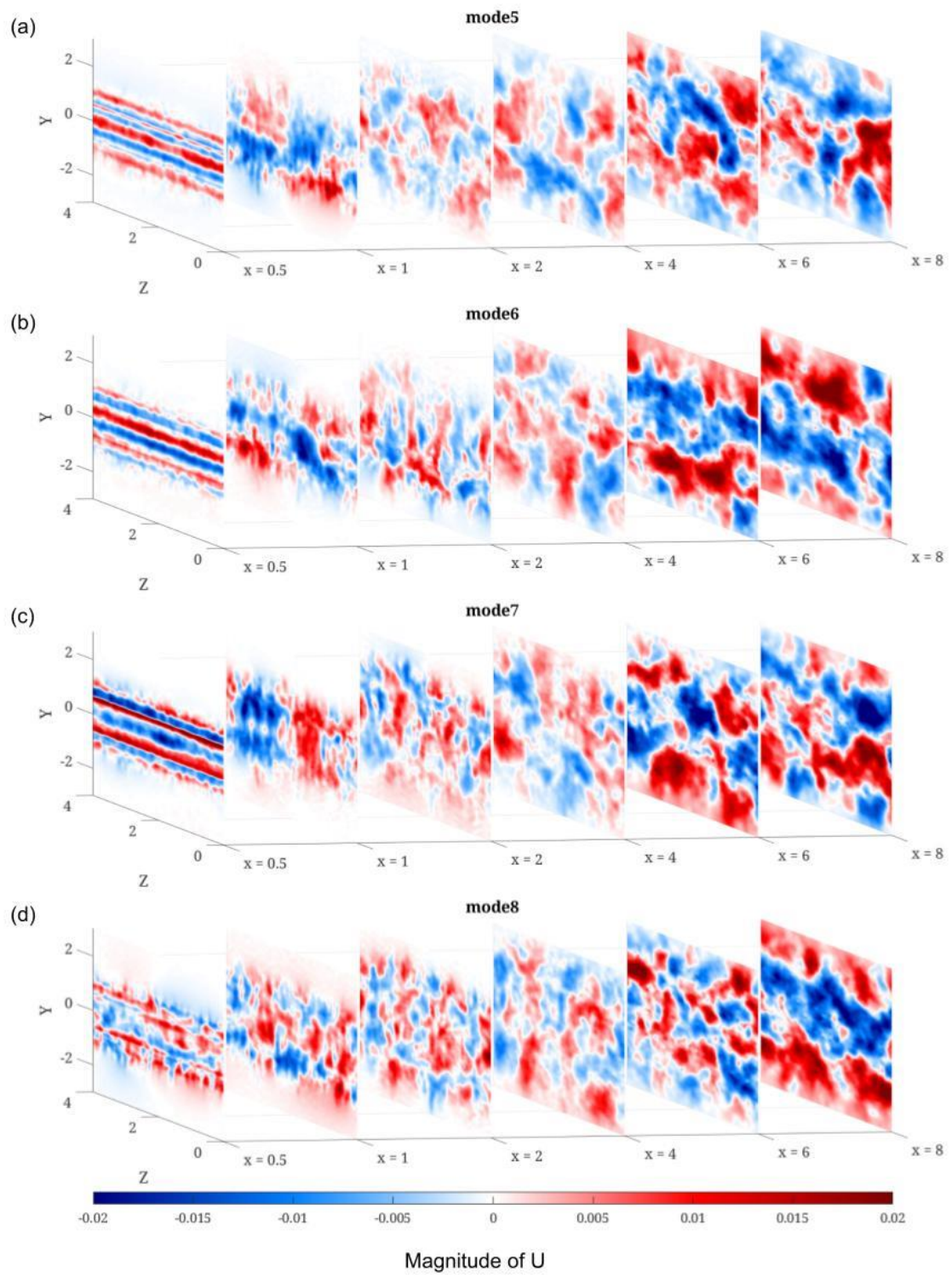


Figure 64: Φ_3 v-component of the POD modes at different x locations for $Ur = 4$: (a) mode 5; (b) mode 6; (c) mode 7; (d) mode 8.

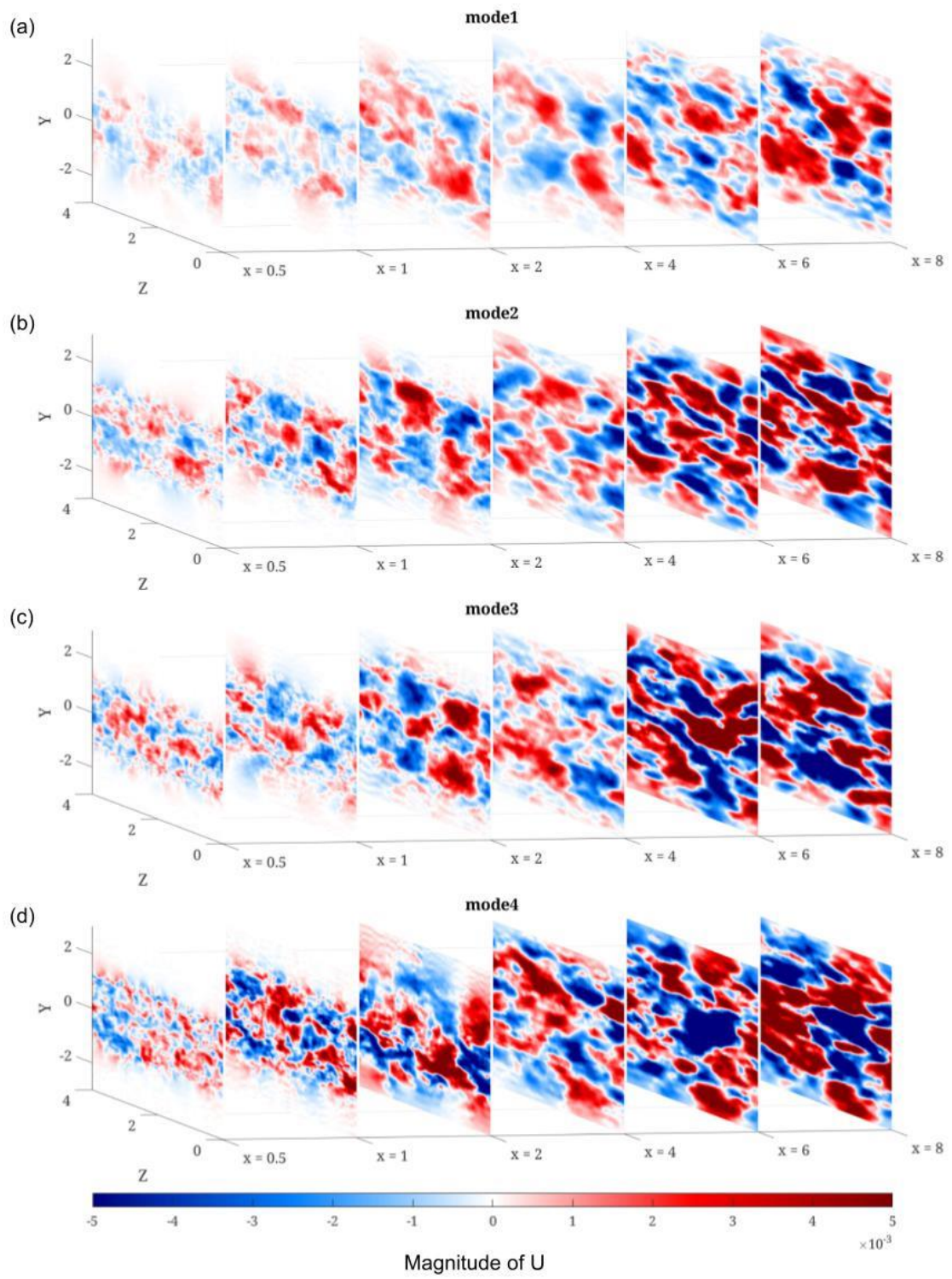


Figure 65: Φ_3 w -component of the POD modes at different x locations for $Ur = 4$: (a) mode 1; (b) mode 2; (c) mode 3; (d) mode 4.

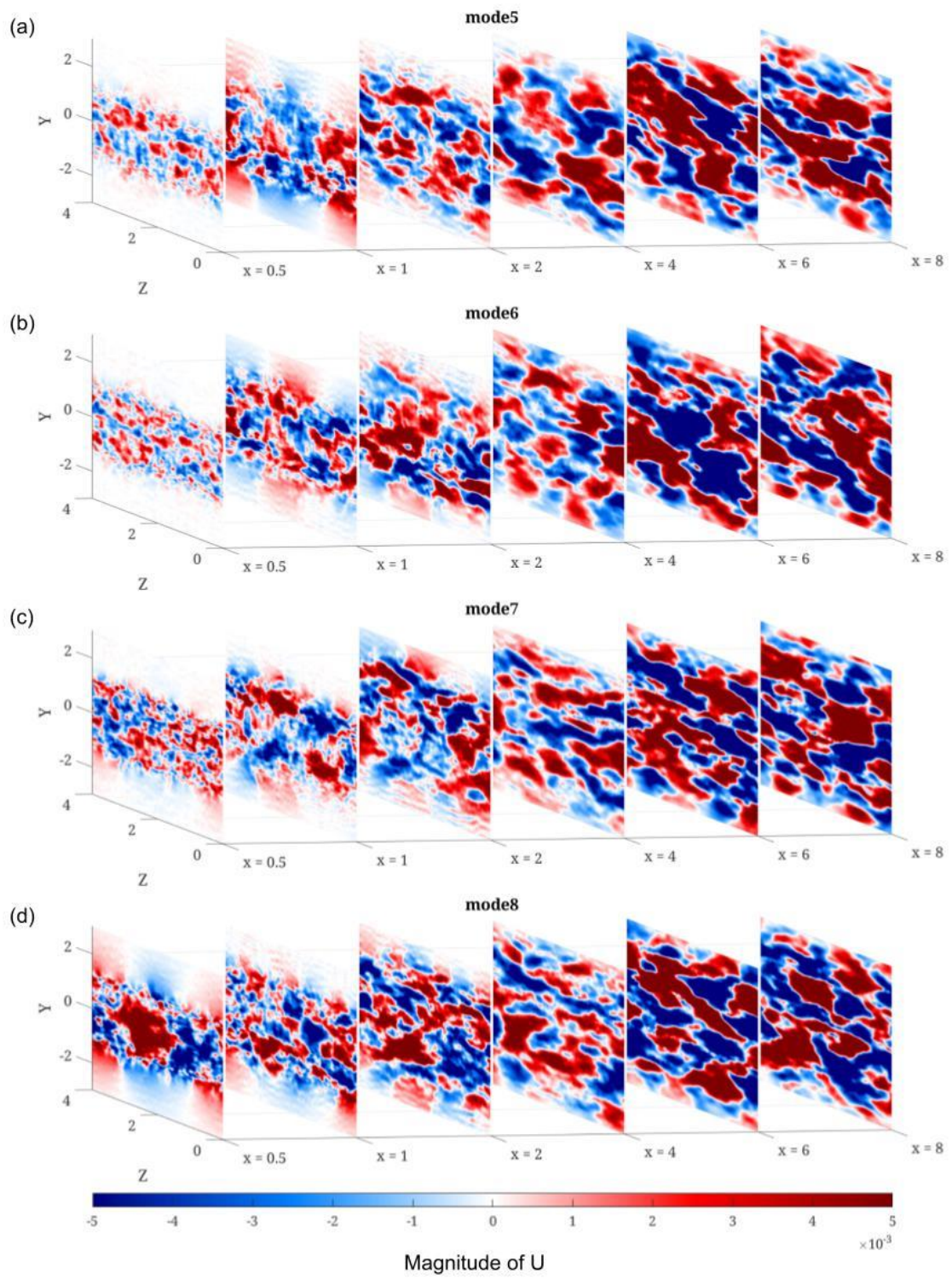
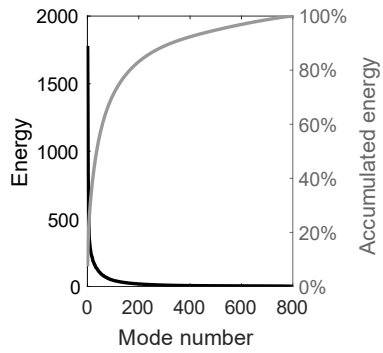
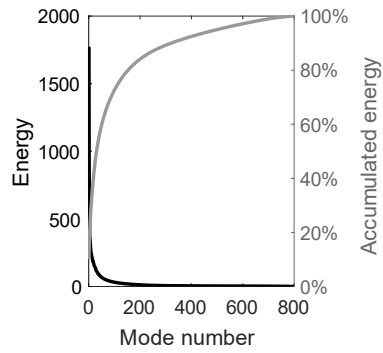


Figure 66: Φ_3 w -component of the POD modes at different x locations for $Ur = 4$: (a) mode 5; (b) mode 6; (c) mode 7; (d) mode 8.

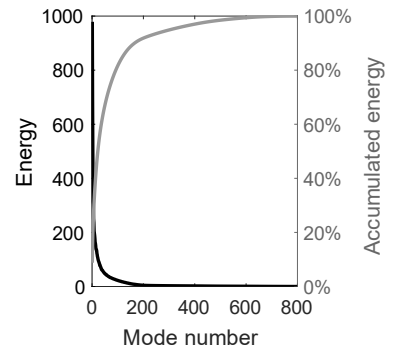
(a) $x = 0.5D$



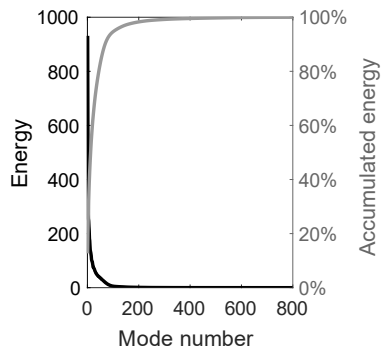
(b) $x = 1D$



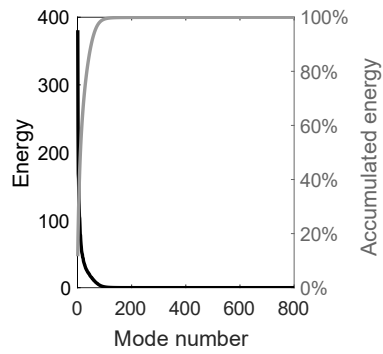
(c) $x = 2D$



(d) $x = 4D$



(e) $x = 6D$



(f) $x = 8D$

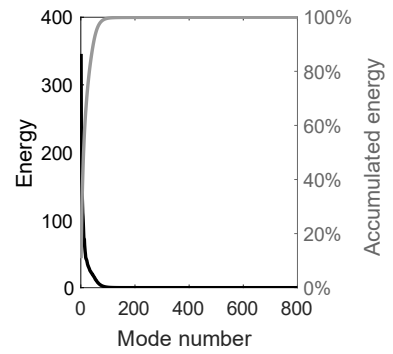


Figure 67: Energy and accumulated energy of POD modes for $Ur = 4$ on YZ planes: (a) $x = 0.5D$; (b) $x = 1D$; (c) $x = 2D$; (d) $x = 4D$; (e) $x = 6D$; (f) $x = 8D$.

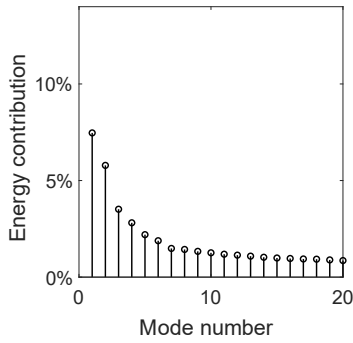
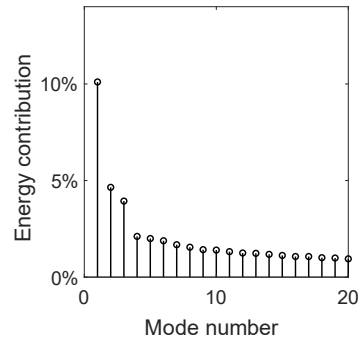
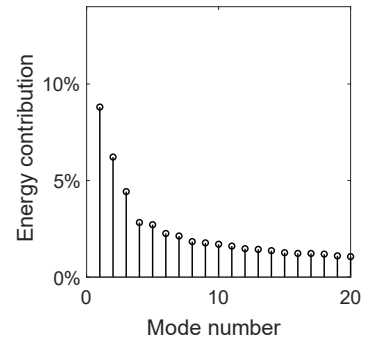
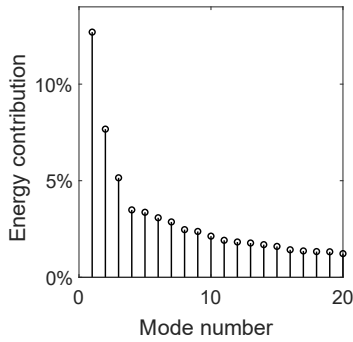
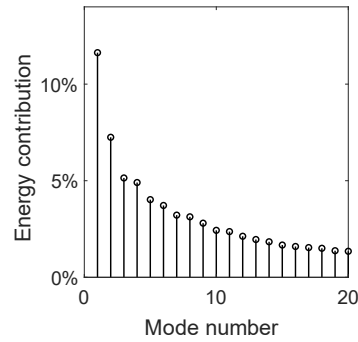
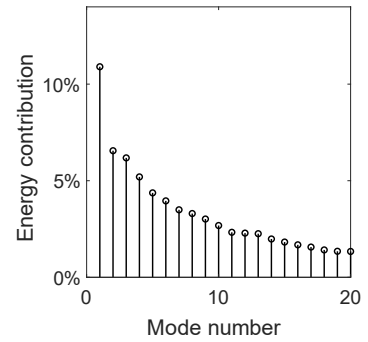
(a) $x = 0.5D$ (b) $x = 1D$ (c) $x = 2D$ (d) $x = 4D$ (e) $x = 6D$ (f) $x = 8D$ 

Figure 68: Energy contribution of the first 20 POD modes for *Ur* 4 on *YZ* planes: (a) $x = 0.5D$; (b) $x = 1D$; (c) $x = 2D$; (d) $x = 4D$; (e) $x = 6D$; (f) $x = 8D$.

5.2.2.2 *Ur* 5

The results for *Ur* 5 are in general similar to the findings from *Ur* 4. Figure 75 shows the energy and accumulated energy of POD modes for the *YZ*-planes. Figure 76 shows the energy contribution of the first 20 POD modes for the *YZ*-planes. Like for the case with *Ur* 4, the POD modes do not come in pairs of similar energy like they do for the *XY*-planes. Similar to the case at *Ur* 4 the energy accumulation of the first 200 modes increases with the distance of the sampling plane to the cylinder.

Figures 77 and 78 show the spatial distribution of the *u*-component for the modes 1 to 8 and figures 79 and 80 show the spatial distribution of the *v*-component for the modes 1 to 8. Like for *Ur* 4 the mode 1 has a high magnitude in the *v*-component while the mode 2 has a high magnitude for the *u*-component. Figures 73 and 74 show the spatial distribution of the *w*-component for the modes 1 to 8. The structure of the first mode for the *w*-component at a distance of $x = 4D$ indicates that there are 4 cells of vortex shedding. (Figure 73 (a)).

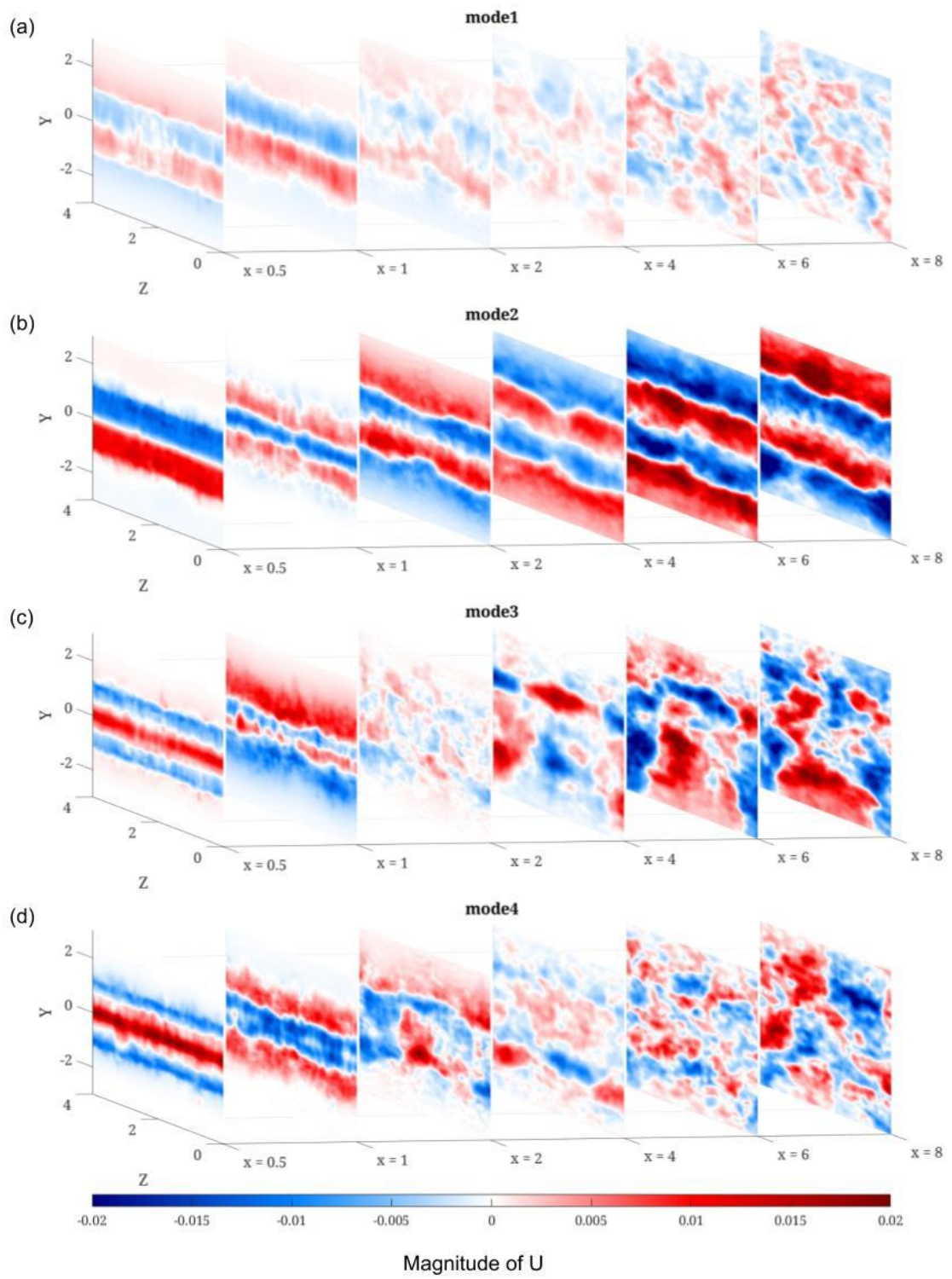


Figure 69: Φ_3 u-component of the POD modes at different x locations for Ur 5: (a) mode 1; (b) mode 2; (c) mode 3; (d) mode 4.

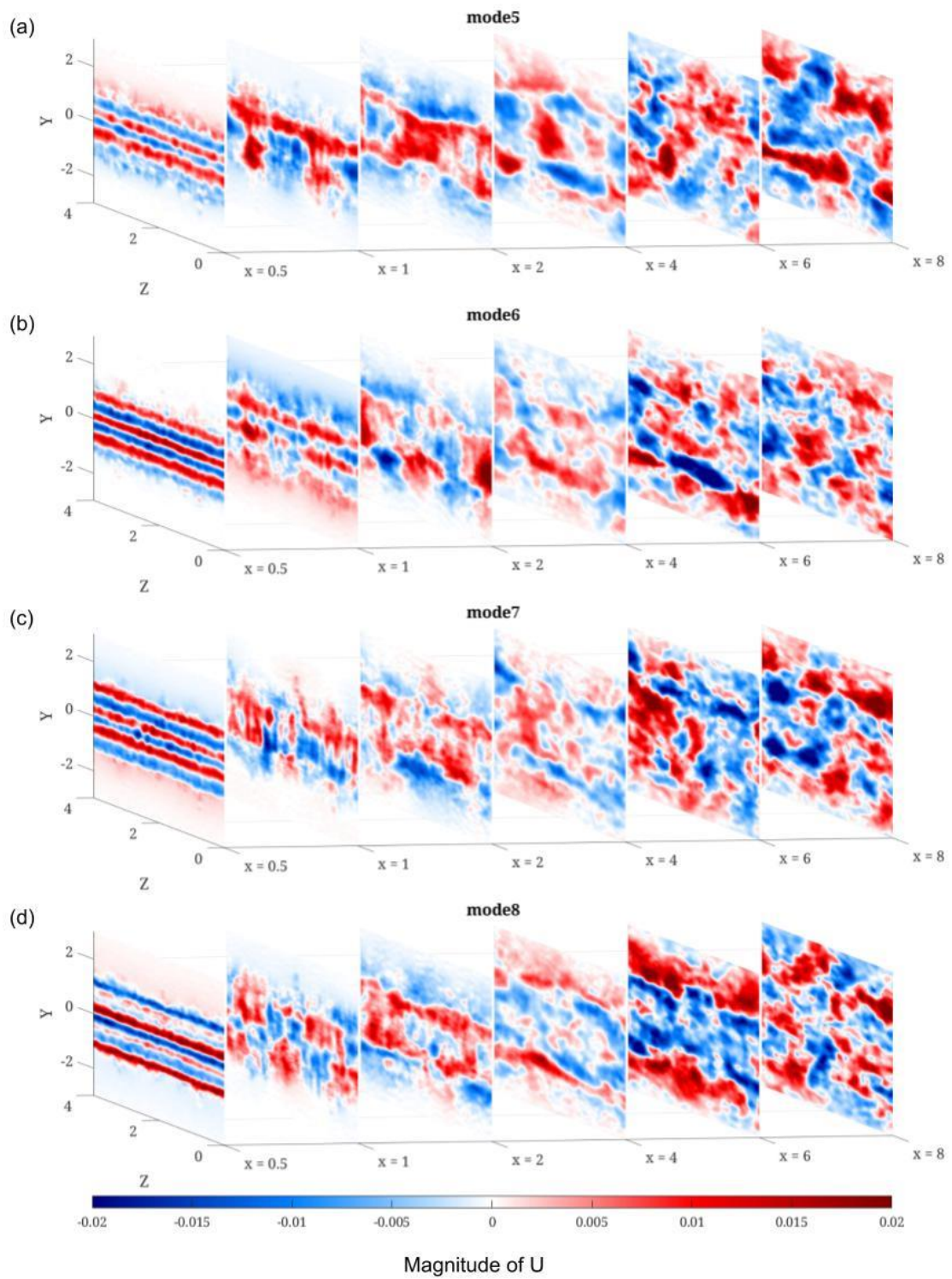


Figure 70: Φ_3 u-component of the POD modes at different x locations for Ur 5: (a) mode 5; (b) mode 6; (c) mode 7; (d) mode 8.

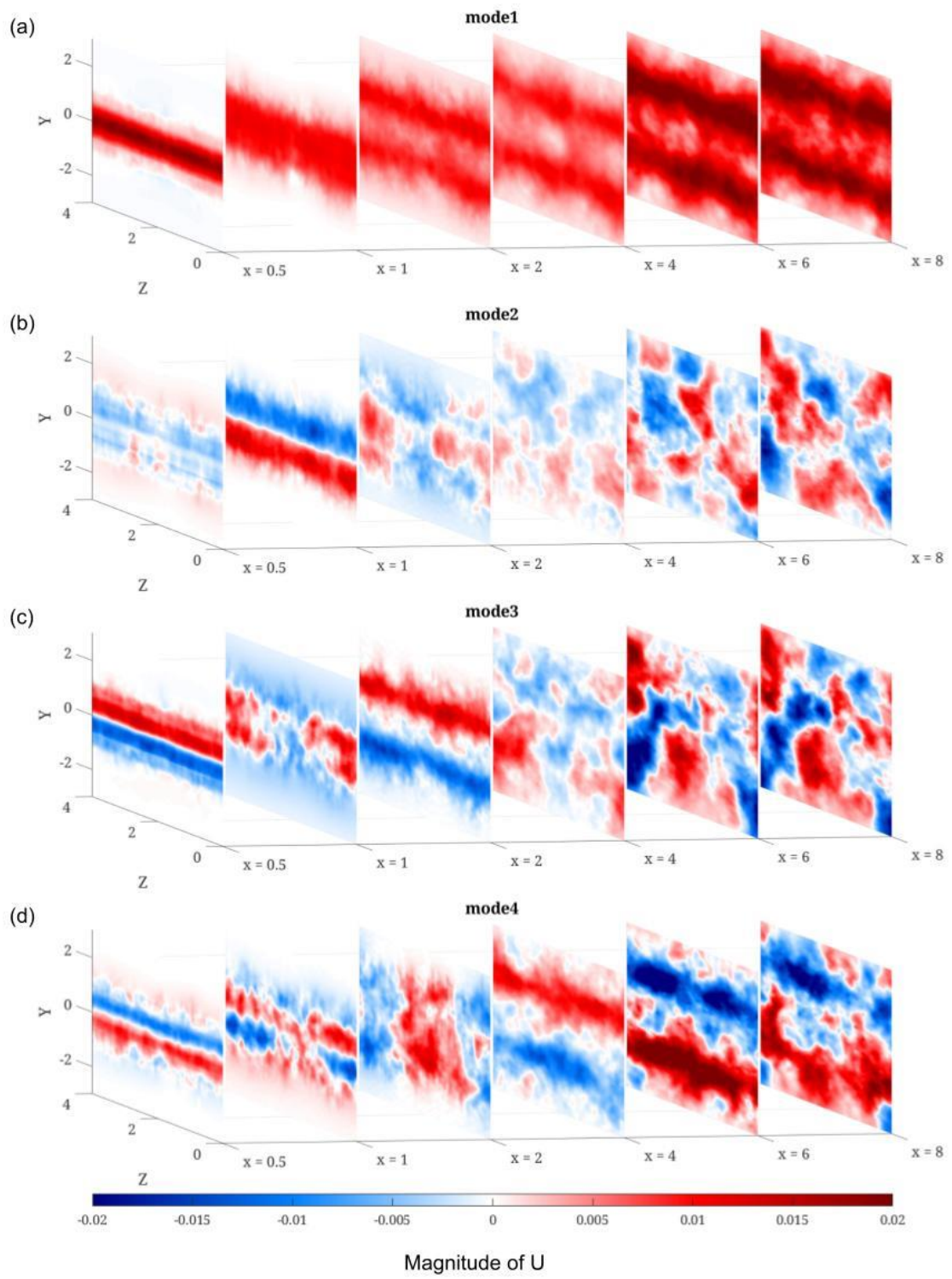


Figure 71: Φ_3 v-component of the POD modes at different x locations for $Ur = 5$: (a) mode1; (b) mode2; (c) mode3; (d) mode4.

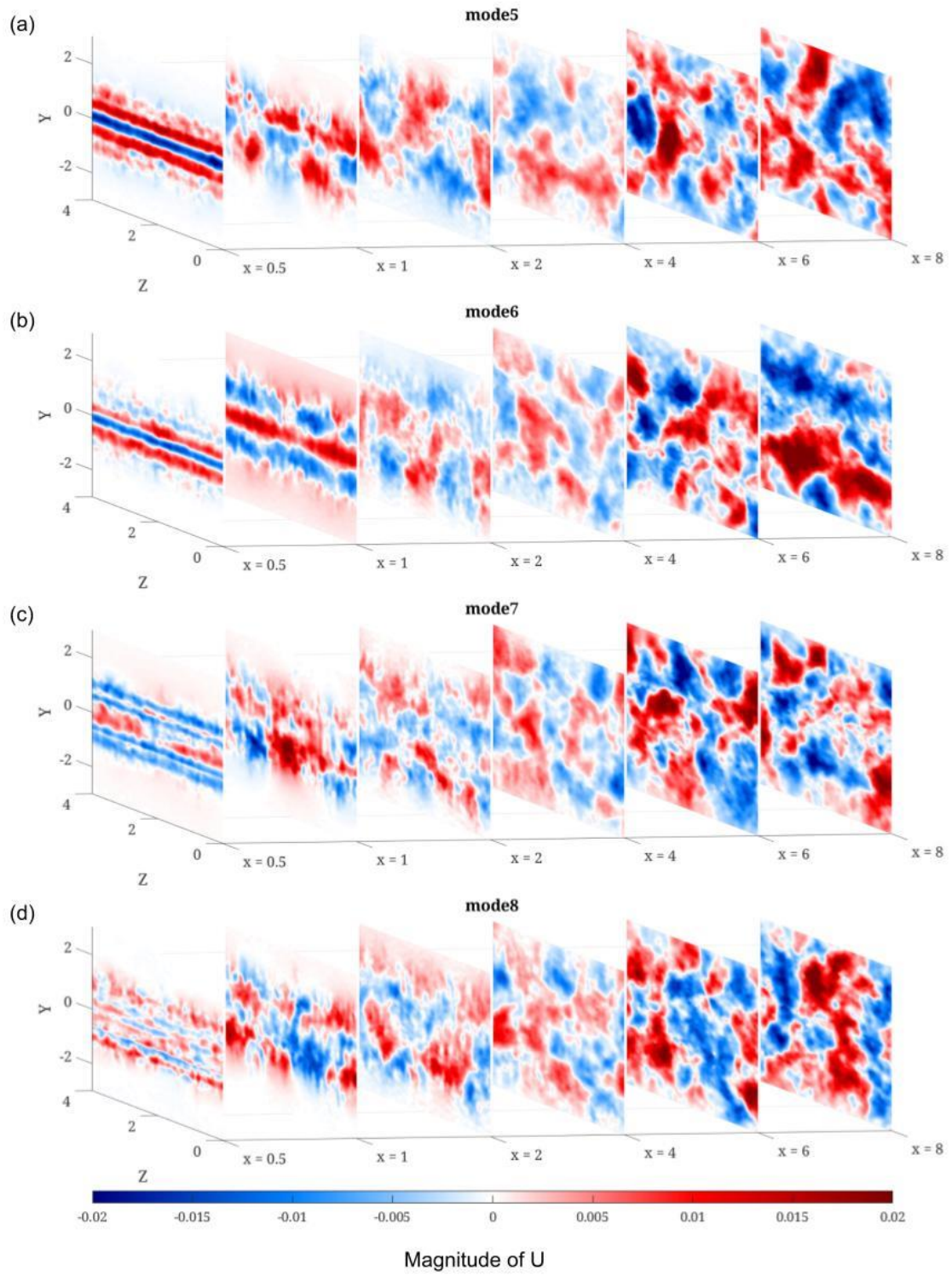


Figure 72: Φ_3 v-component of the POD modes at different x locations for $Ur = 5$: (a) mode 5; (b) mode 6; (c) mode 7; (d) mode 8.

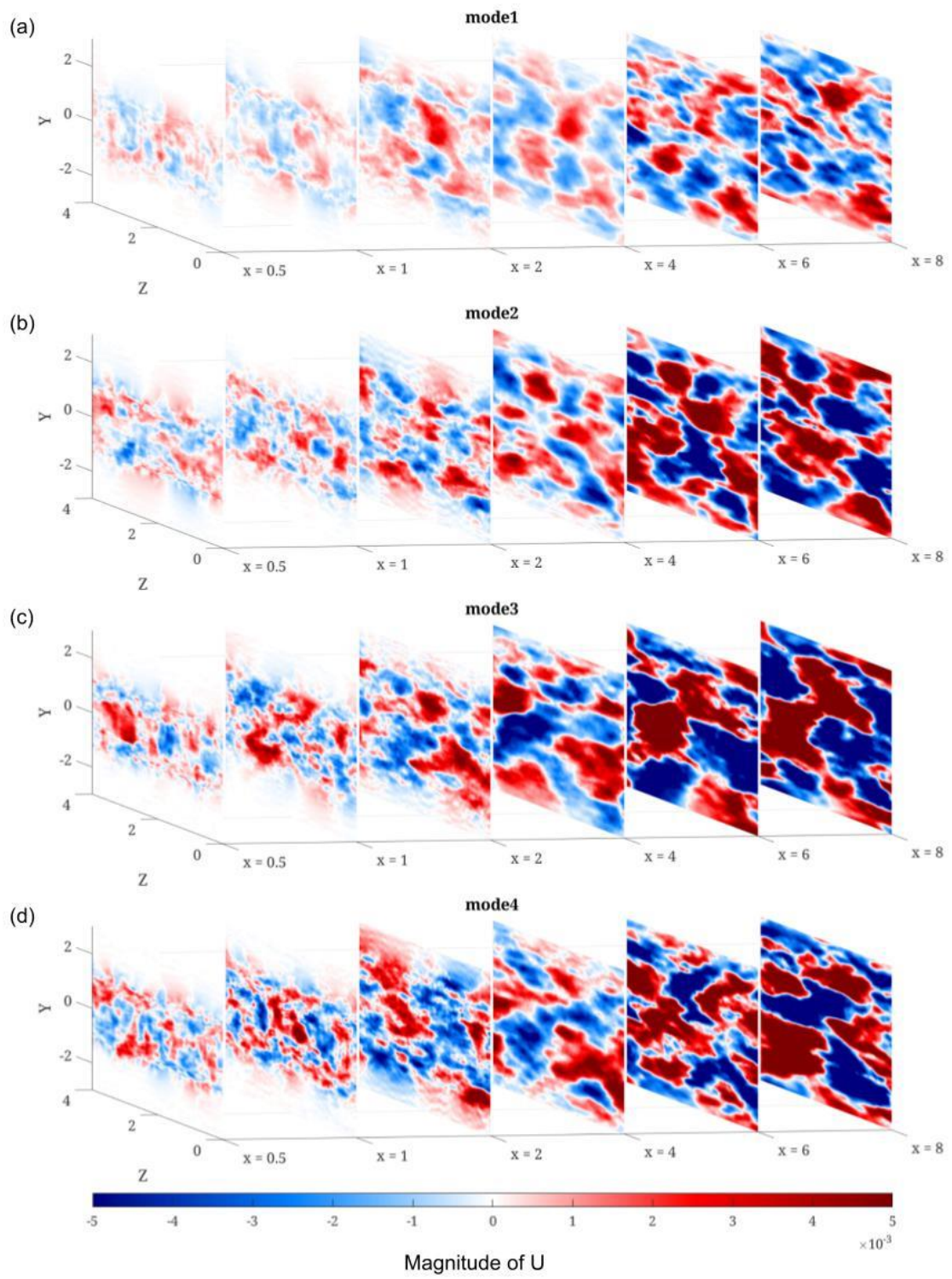


Figure 73: Φ_3 w-component of the POD modes at different x locations for $Ur = 5$: (a) mode 1; (b) mode 2; (c) mode 3; (d) mode 4.

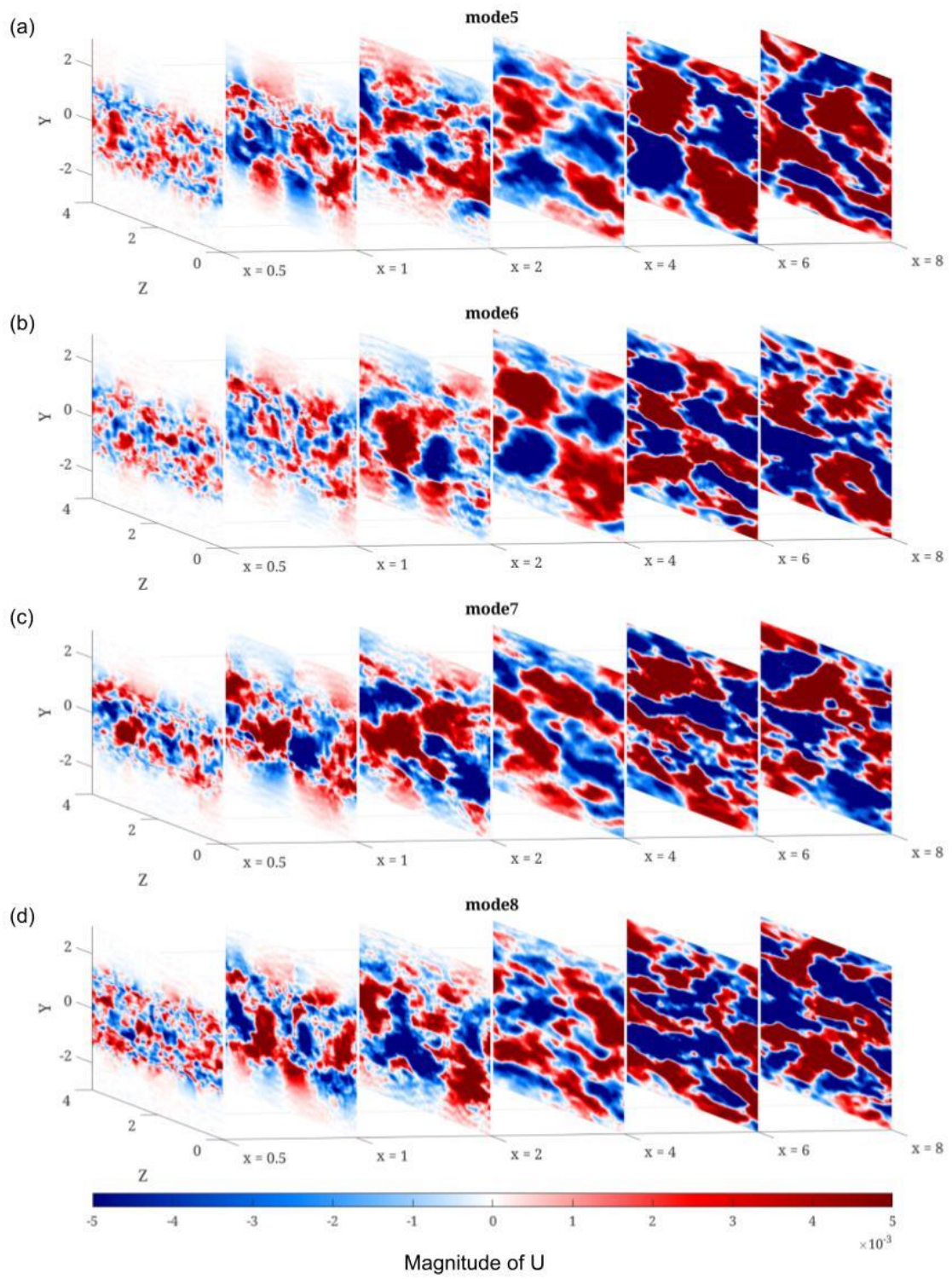
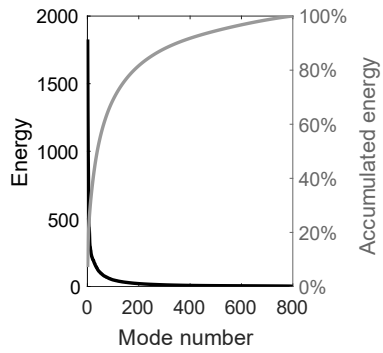
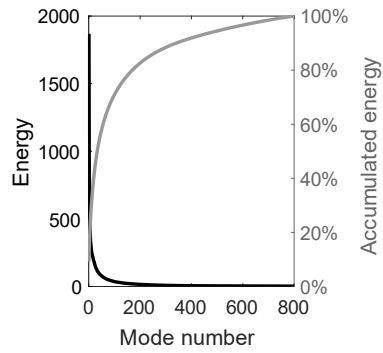


Figure 74: Φ_3 w-component of the POD modes at different x locations for Ur 5: (a) mode 5; (b) mode 6; (c) mode 7; (d) mode 8.

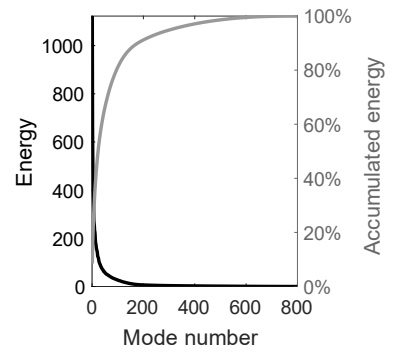
(a) $x = 0.5D$



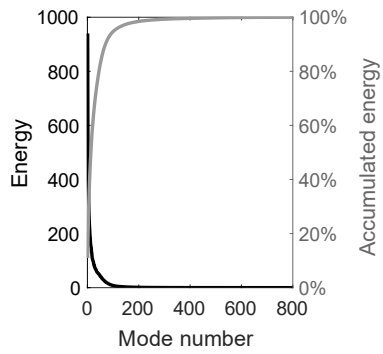
(b) $x = 1D$



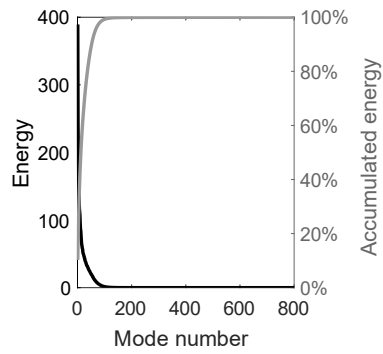
(c) $x = 2D$



(d) $x = 4D$



(e) $x = 6D$



(f) $x = 8D$

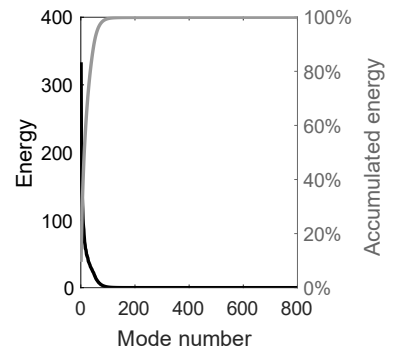


Figure 75: Energy and accumulated energy of POD modes for $Ur = 5$ on YZ planes: (a) $x = 0.5D$; (b) $x = 1D$; (c) $x = 2D$; (d) $x = 4D$; (e) $x = 6D$; (f) $x = 8D$.

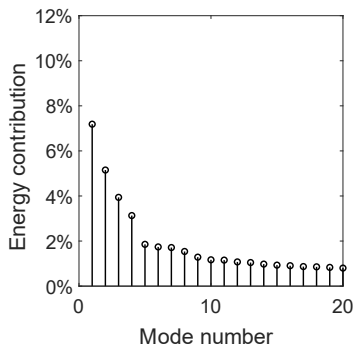
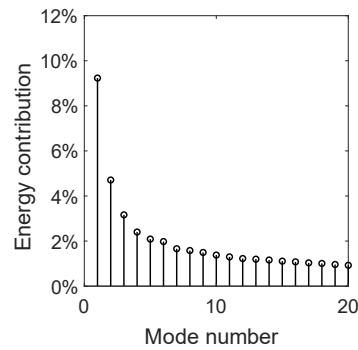
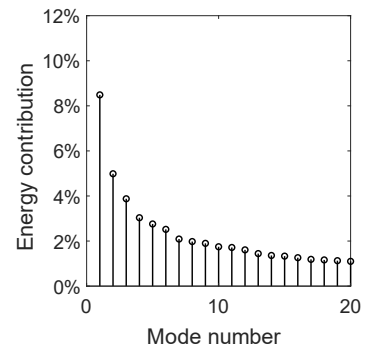
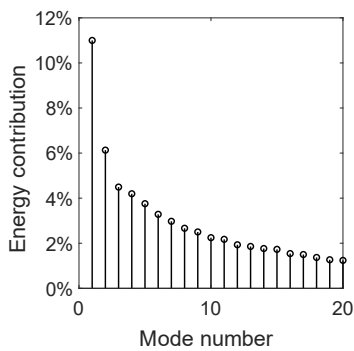
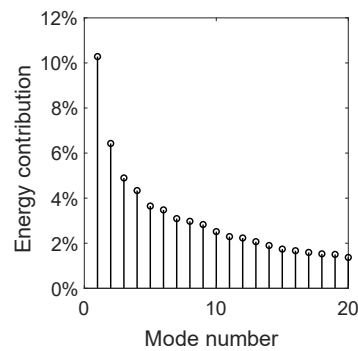
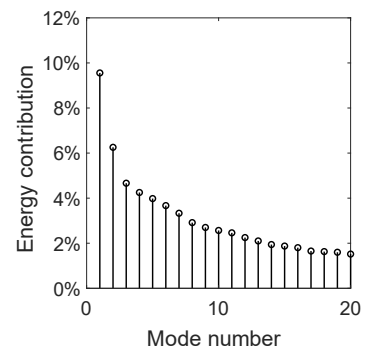
(a) $x = 0.5D$ (b) $x = 1D$ (c) $x = 2D$ (d) $x = 4D$ (e) $x = 6D$ (f) $x = 8D$ 

Figure 76: Energy contribution of the first 20 POD modes for *Ur* 5 on *YZ* planes: (a) $x = 0.5D$; (b) $x = 1D$; (c) $x = 2D$; (d) $x = 4D$; (e) $x = 6D$; (f) $x = 8D$.

5.2.2.3 *Ur* 7

Figure 83 shows the energy and accumulated energy of POD modes for the *YZ*-planes. The results of the energy and accumulated energy are similar to the cases for *Ur* 4 and *Ur* 5. Figure 84 shows the energy contribution of the first 20 POD modes for the *YZ*-planes. Compared to the cases for *Ur* 4 and *Ur* 5 it is noticeable that the energy contribution of the first most energetic mode is in general higher for *Ur* 7 across all sampling locations. The difference in the energy contribution between the first most energetic mode and the second most energetic mode is higher, the first mode has a energy contribution of more than 2 times of the contribution of the second mode.

The figures 77 and 78 show the spatial distribution of the *u*-component for the modes 1 to 8. It can be seen that mode 1 (Figure 77(a)) has a clear structure and a high magnitude of *U* for locations close to the cylinder at $x = 0.5D$ and $x = 1D$. For a bigger distance to the cylinder the magnitude drops significantly. Mode 2 (Figure 77(b)) shows a different behaviour than mode 1 with a higher magnitude for the distance of $x = 6D$ and $x = 8D$. The second harmonic modes 3 and 4 (Figure 77(c,d)) show a less clear pattern. For modes higher than mode 4 and a distance greater than $x = 2D$ no pattern can be

identified. Figures 79 and 80 show the spatial distribution of the v -component for the modes 1 to 8. The mode 1 (Figure 79(a)) shows only positive or negative magnitudes for each YZ -plane with indicates uniform flow. Figures 81 and 82 show the spatial distribution of the w -component. The mode 1 (Figure 81(a)) has the lowest magnitude across all x locations of the sampling plane. For the modes 3, 4 and 5 the spatial distribution on the YZ -plane at $x = 6D$ shows 4 cells of vortex formation. For the other modes no clear vortex formation cells are found.

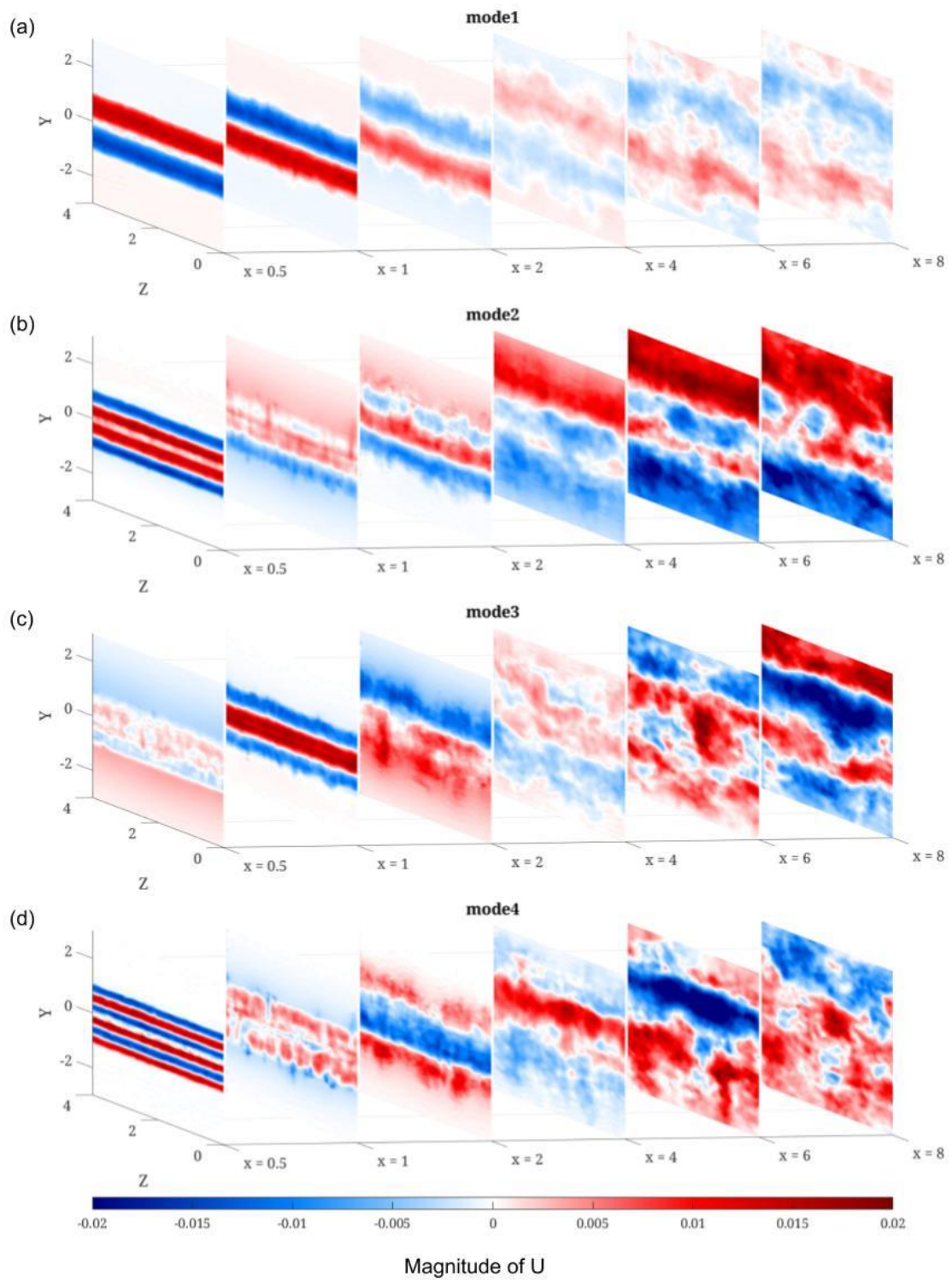


Figure 77: Φ_3 u-component of the POD modes at different x locations for $Ur 7$: (a) mode 1; (b) mode 2; (c) mode 3; (d) mode 4.

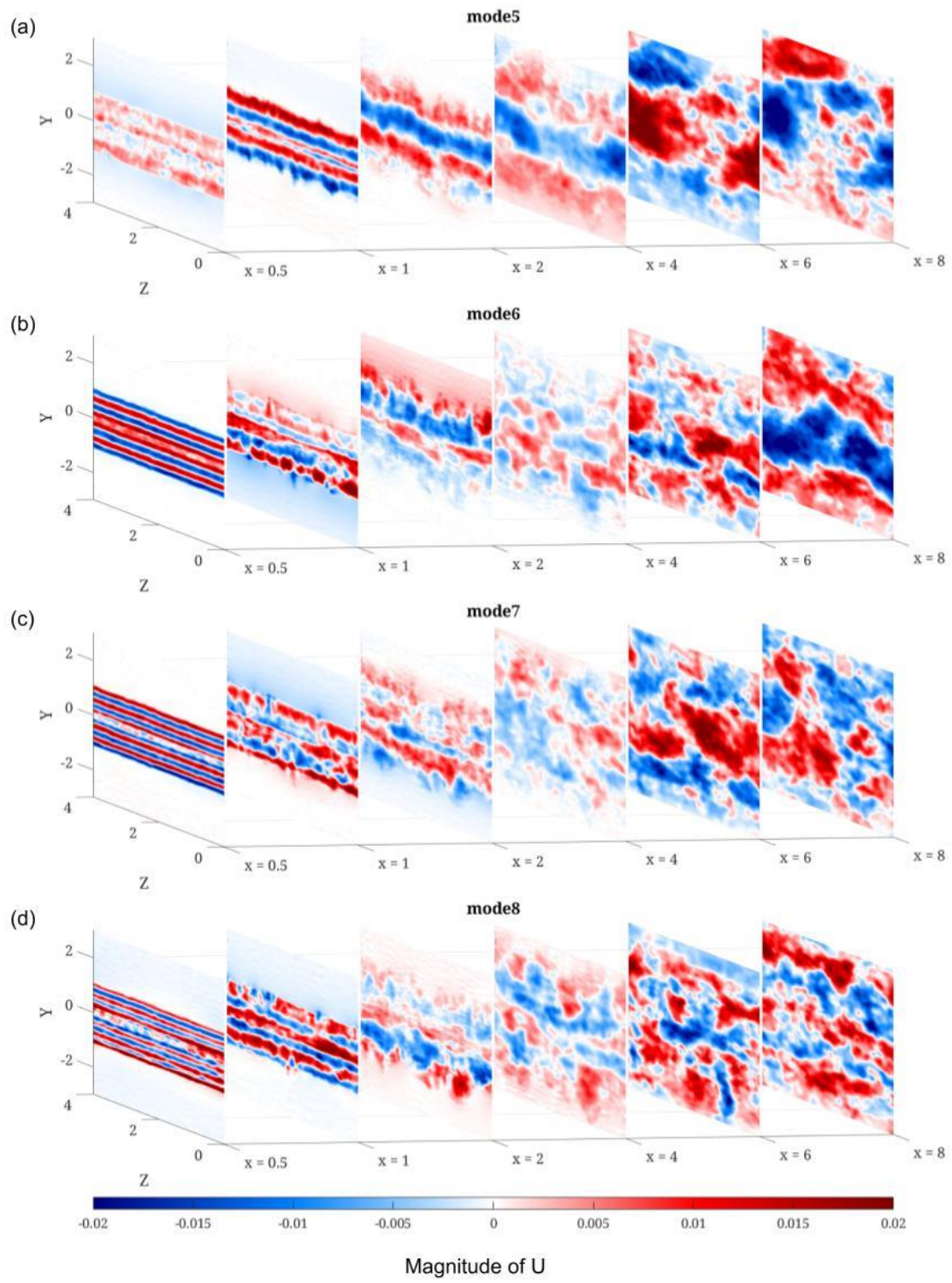


Figure 78: Φ_3 u-component of the POD modes at different x locations for Ur 7: (a) mode 5; (b) mode 6; (c) mode 7; (d) mode 8.

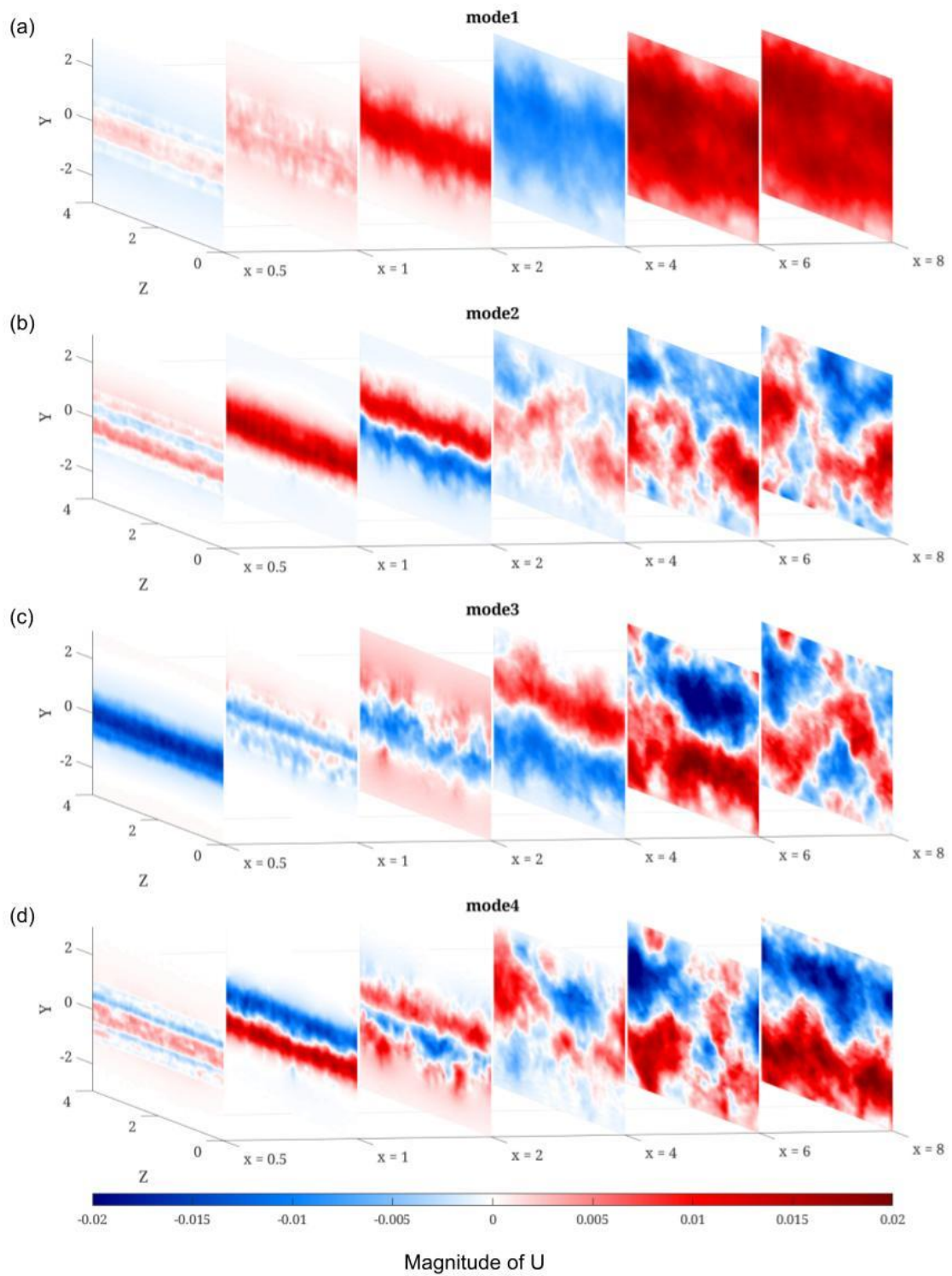


Figure 79: Φ_3 v-component of the POD modes at different x locations for $Ur = 7$: (a) mode 1; (b) mode 2; (c) mode 3; (d) mode 4.

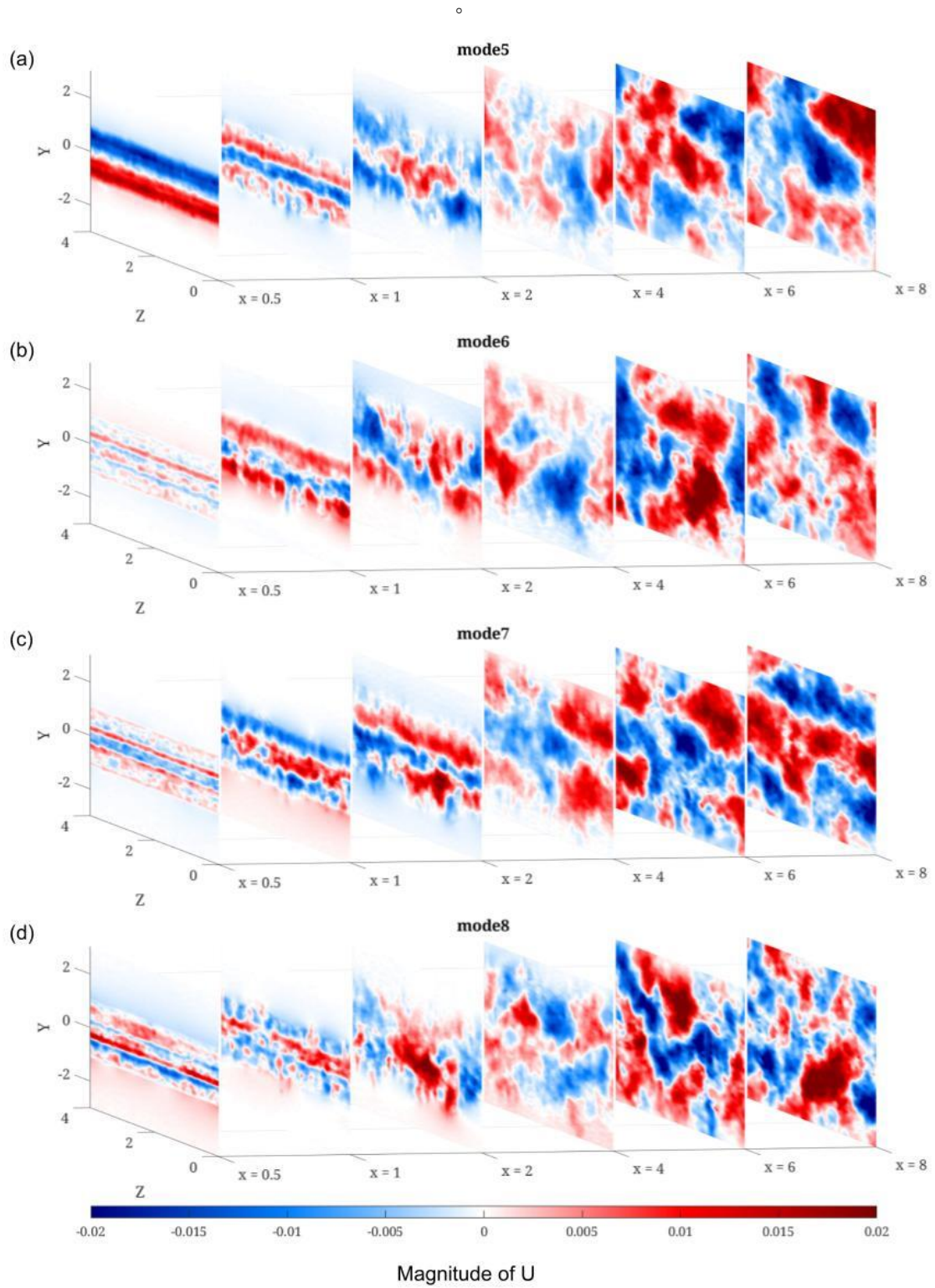


Figure 80: Φ_3 v-component of the POD modes at different x locations for $Ur = 7$: (a) mode 5; (b) mode 6; (c) mode 7; (d) mode 8.

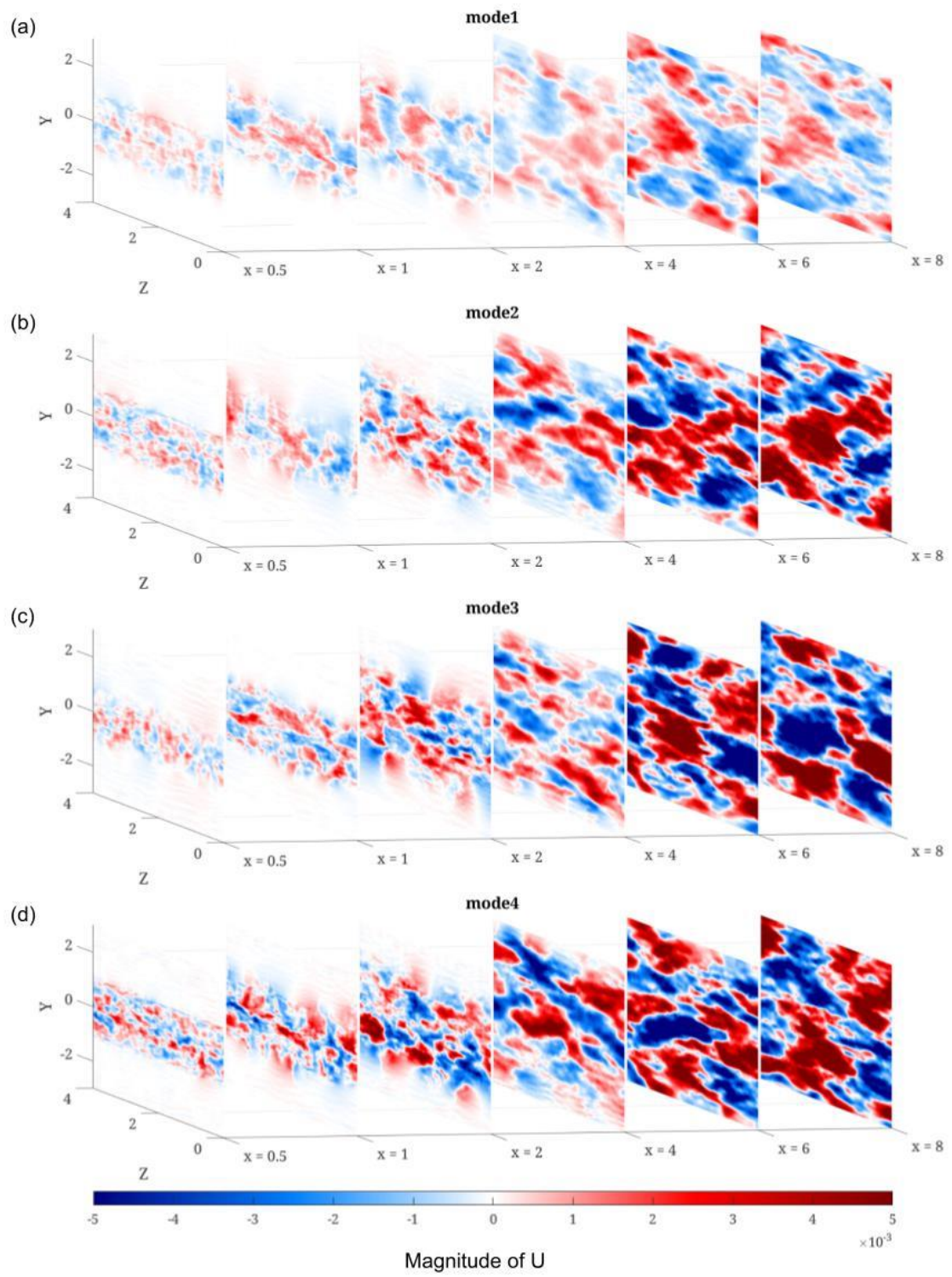


Figure 81: Φ_3 w-component of the POD modes at different x locations for $Ur = 7$: (a) mode 1; (b) mode 2; (c) mode 3; (d) mode 4.

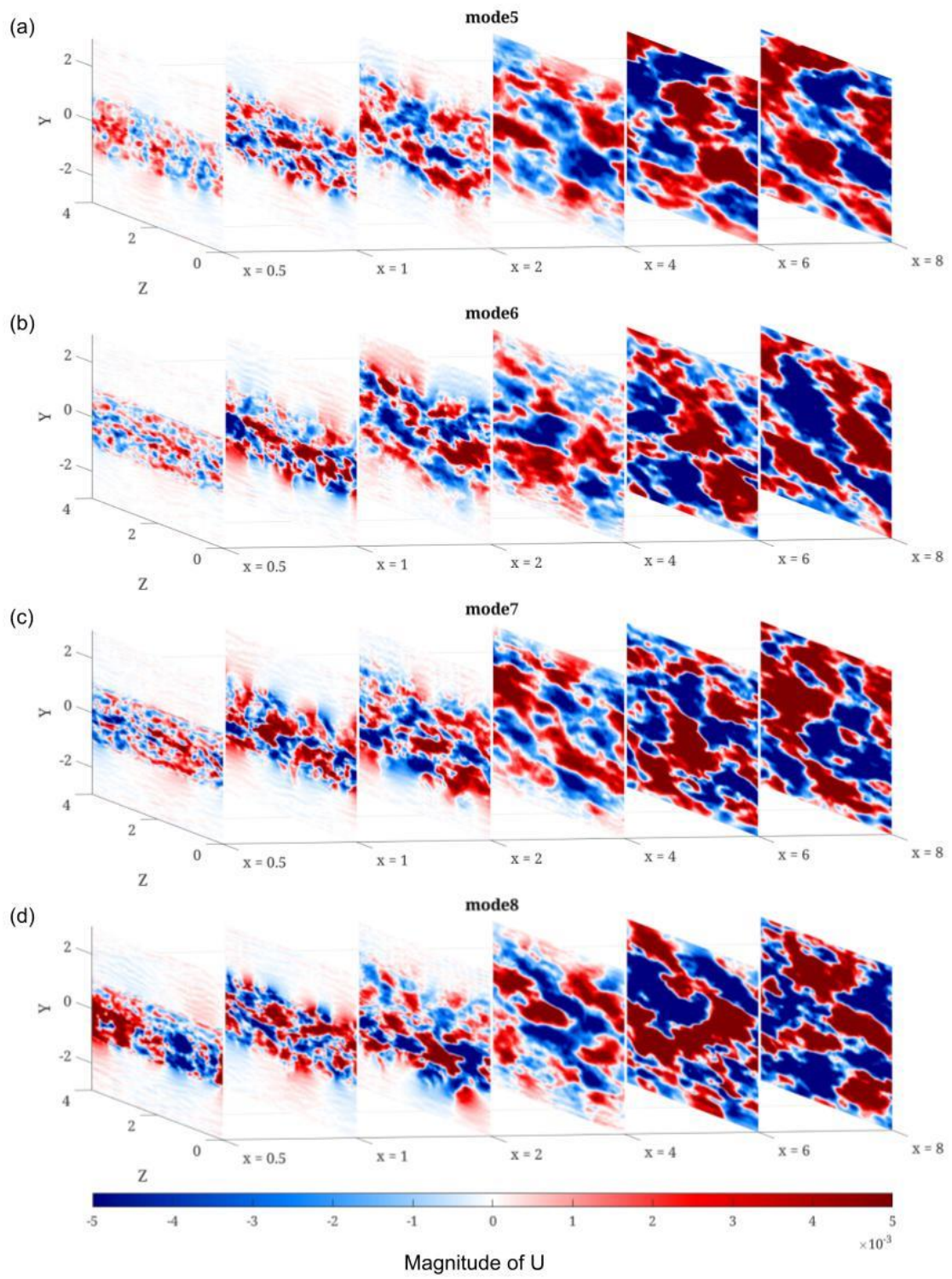
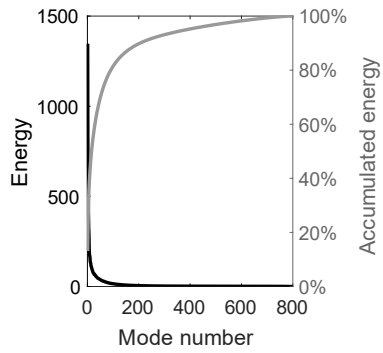
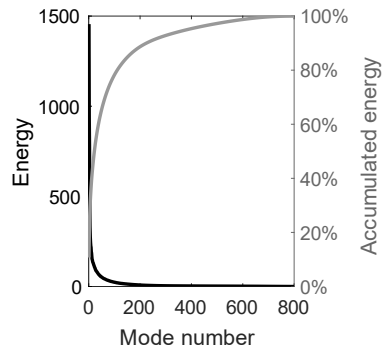


Figure 82: Φ_3 w-component of the POD modes at different x locations for $Ur = 7$: (a) mode 5; (b) mode 6; (c) mode 7; (d) mode 8.

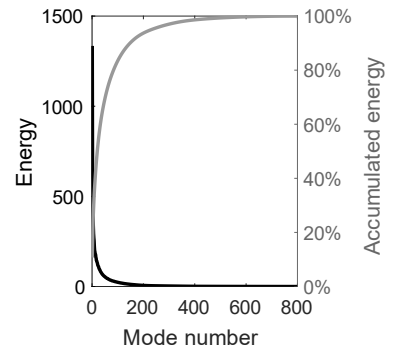
(a) $x = 0.5D$



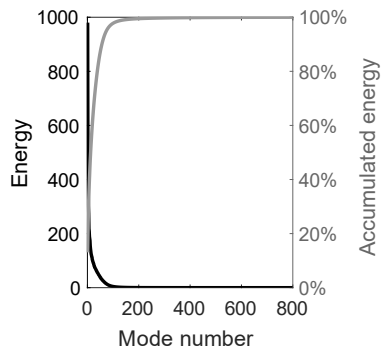
(b) $x = 1D$



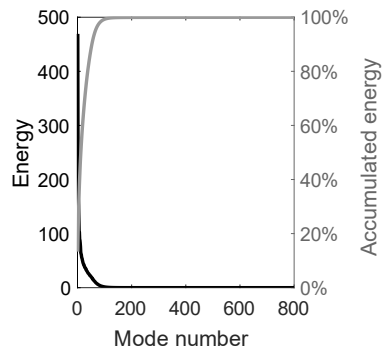
(c) $x = 2D$



(d) $x = 4D$



(e) $x = 6D$



(f) $x = 8D$

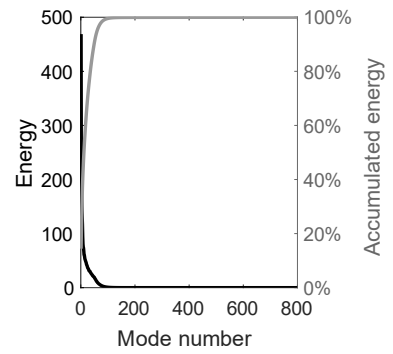
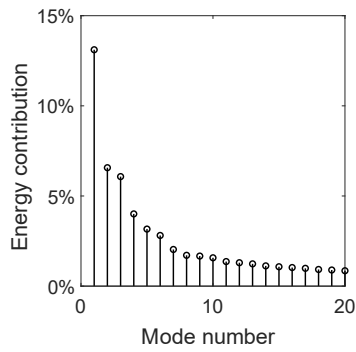
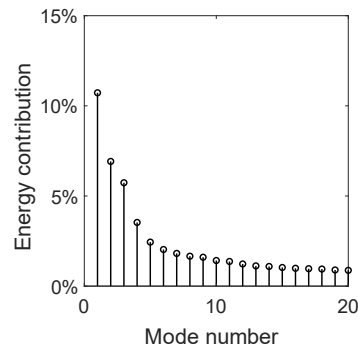


Figure 83: Energy and accumulated energy of POD modes for $Ur = 7$ on YZ planes: (a) $x = 0.5D$; (b) $x = 1D$; (c) $x = 2D$; (d) $x = 4D$; (e) $x = 6D$; (f) $x = 8D$.

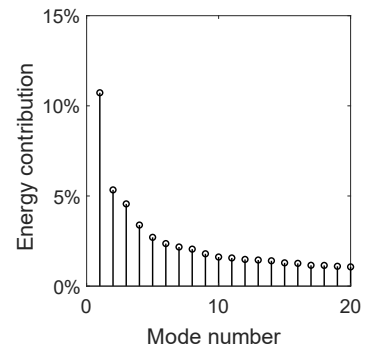
(a) $x = 0.5D$



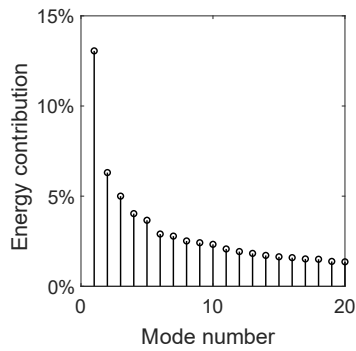
(b) $x = 1D$



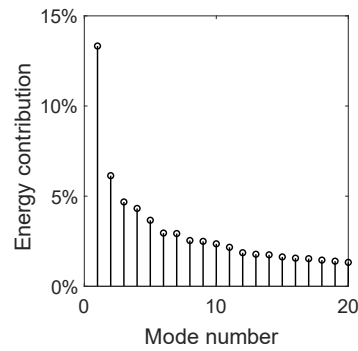
(c) $x = 2D$



(d) $x = 4D$



(e) $x = 6D$



(f) $x = 8D$

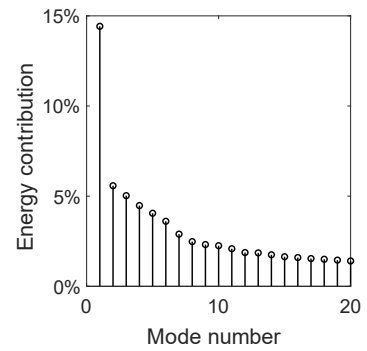


Figure 84: Energy contribution of the first 20 POD modes for *Ur* 7 on *YZ* planes: (a) $x = 0.5D$; (b) $x = 1D$; (c) $x = 2D$; (d) $x = 4D$; (e) $x = 6D$; (f) $x = 8D$.

6 Conclusion

In the present study simulations of a cylinder subject to VIV in the subcritical Re regime are performed and the wake structures are analyzed. First a convergence study for the mesh verification is performed for a stationary cylinder configuration. The normal mesh with ≈ 5 million cells is found to provide good balance of computational cost and accuracy. The time step of $\Delta t = 0.002$ is found to give sufficient temporal resolution. The present numerical model is validated by extensive comparison with available experimental data on stationary and vibrating cylinders at similar Re . The averaged flow velocities in the wake, pressure coefficient on the cylinder surface and skin friction coefficient are discussed and found to be in good agreement with the experimental data. It is concluded that the accuracy of the present simulation is sufficient. Based on the simulation parameters of the stationary cylinder an elastically mounted cylinder which is free to move in the cross-flow direction is simulated. The simulation is performed at three different values of Ur . The lift and drag coefficients as well as the cross-flow displacement are reported. The displacements observed in the present simulations are slightly lower than experimentally measured displacements reported by Assi, Bearman and Meneghini (2010). Vortex shedding modes in the investigated cases are analyzed and classified. A good agreement is found between the observed vortex shedding modes and those predicted by the shedding mode map created by Morse and Williamson (2009). The $2P_0$ mode is found during the initial phase in the simulation for Ur 5. For further analysis of the wake structure the POD analysis is performed on data obtained from sampling planes located in the wake. The POD analysis is used to identify the coherent structures in the wake of the vibrating cylinder. First and second harmonic mode pairs are found. A traveling wave is identified in the wake. Vortex formation cells for the spanwise direction are found on the YZ-planes in the wake flow.

7 Future Work

7.1 VIV Mitigation

In engineering applications, the most frequently encountered passive VIV mitigation devices are based on strakes attached to the cylinder. Effectiveness of this type of devices has been well studied and documented in numerous studies. However, there are some undesired effects associated with strakes, e.g. increased drag due to increase in effective diameter of the cylinder and asymmetry in hydrodynamic loading. Furthermore Quen, et al. (2018) have already shown that low mass-ratio cylinders require a larger pitch to effectively mitigate VIV. The topic of VIV Mitigation of low mass-ratio cylinders is of grade interest and the effect of a variety of changes to the helix structure can be investigated for their effects. Changes could include the variation of the number of helix strakes, the pitch or the heights of the strake. Other geometries for VIV mitigation are also of interest. The flow structure that was found in this paper can help to develop new geometries that break apart the cells of vortex formation to reduce the lift force on the cylinder. The numerical model that was validated in this paper can be used for the simulation of new passive VIV mitigation devices.

7.2 Wake Induced Vibrations (WIV)

For a tandem arrangement of cylinders, where one cylinder is located in the wake of the upstream cylinder, the wake can cause extensive motion on the downstream cylinder. Assi, Bearman and Meneghini (2010) have shown that the downstream cylinder can reach vibration amplitudes of up to $6D$. For the investigation of a WIV mitigation method and the effectiveness of current VIV mitigation strategies against WIV, a detailed flow simulation of a tandem cylinder configuration is of great interest.

References

- Anderson, Edward, et al. "LAPACK users' guide." *Society for industrial and applied mathematics*, 1999.
- Assi, Gustavo R. S., and T. Crespi. "Laboratory Investigation of Helical Strakes With Serrated and Twisted Fins to Suppress VIV." *International Conference on Offshore Mechanics and Arctic Engineering, American Society of Mechanical Engineers.*, 2019.
- Assi, Gustavo R. S., J. Meneghini, J. Aranha, P. Bearman, and E. Casaprima. "Experimental investigation of flow-induced vibration interference between two circular cylinders." *Journal of Fluids and Structures* 22(6-7) (2006): 819-827.
- Assi, Gustavo R. S., P. W. Bearman, and J. R. Meneghini. "On the wake-induced vibration of tandem circular cylinders: the vortex interaction excitation mechanism." *Journal of Fluid Mechanics* (Journal of Fluid Mechanics) 661 (2010): 365.
- Assi, Gustavo R. S., R. M. Orselli, and M. Silva-Ortega. "Control of vortex shedding from a circular cylinder by rotating wake-control cylinders at a moderate Reynolds number." *FIV2018 Conference.*, 2018.
- Bakker , André. "Lecture 7-Meshing Applied Computational Fluid Dynamics." 2002.
- Baz, A., and M. Kim. "Active modal control of vortex-induced vibrations of a flexible cylinder." *Journal of Sound and Vibration* no. 1 (1993): 69-84.
- Bearman, P., and M. Branković. "Experimental studies of passive control of vortex-induced vibration." *European Journal of Mechanics-B/Fluids* 23 (2004): 9-15.
- Çengel, Yunus A., and John M. Cimbala. *Fluid Mechanics: Fundamentals and Applications*. McGraw-Hill Higher Education, 2006.
- Cicolin, M., and G. Assi. ""Experiments with flexible shrouds to reduce the vortex-induced vibration of a cylinder with low mass and damping." *Applied Ocean Research* 65 (2017): 290-301.
- Ecke, Robert. *The turbulence problem: An experimentalist's perspective*. Los Alamos Science, 2005.
- Feng, C. C. "The measurement of vortex induced effects in flow past stationary and oscillating circular and D-section cylinders." *Doctoral dissertation, University of British Columbia*, 1968.
- Feng, Li-Hao, Jin-Jun Wang, and Chong Pan. "Proper orthogonal decomposition analysis of vortex dynamics of a circular cylinder under synthetic jet control." *Physics of Fluids* 23, no. 1 (2011): 014106.

- Gabbai, R., and H. Benaroya. "An overview of modeling and experiments of vortex-induced vibration of circular cylinders." *Journal of Sound and Vibration* 282(3-5) (2005): 575-616.
- Govardhan, R., and C. Williamson. "Resonance forever: existence of a critical mass and an infinite regime of resonance in vortex-induced vibration." *Journal of Fluid Mechanics* 473 (2002): 47-166.
- Greenshields, C. "OpenFOAM–The OpenFOAM Foundation–User Guide, version 8." 2020.
- Jauvtis, N., and C. Williamson. "The effect of two degrees of freedom on vortex-induced vibration at low mass and damping." *Journal of Fluid Mechanics* 509 (2004): 23.
- Khalak, Asif, and Charles HK Williamson. "Motions, forces and mode transitions in vortex-induced vibrations at low mass-damping." *Journal of fluids and Structures* 13, no. no. 7-8 (1999): 813-851.
- Kravchenko, A. G., and P. Moin. "Numerical studies of flow over a circular cylinder at $Re = 3900$." *Physics of fluids* 12(2) (2000): 403-417.
- Lourenco, L., and C. Shih. "Characteristics of the plane turbulent near wake of a circular cylinder: A particle image velocity study (private communication), reported by Kravchenko, AG, Moin, P., 2000. Numerical studies of flow over a circular cylinder at $ReD= 3900$." *Phys. Fluids* 12 (1993): 403-417.
- Lumley, JL. . *The structure of inhomogeneous turbulent flows Atmospheric Turbulence and Radio Wave Propagation ed AM Yaglom and VI Tatarski*. Atmospheric turbulence and radio wave propagation, 1967.
- Ma, X., G.-S. Karamanos, and G. Karniadakis. "Dynamics and low-dimensionality of a turbulent near wake." *Journal of fluid mechanics* 410 (2000): 29-65.
- Moghadam, Seifollahi, François Guibault Zahra, and André Garon. "On the Evaluation of Mesh Resolution for Large-Eddy Simulation of Internal Flows Using Openfoam." *Fluids* 6 no. 1 (2021): 24.
- Morse, T., and C. Williamson. "Fluid forcing, wake modes, and transitions for a cylinder undergoing controlled oscillations." *Journal of Fluids and Structures* 25(4) (2009): 697-712.
- Muld, Tomas W., Gunilla Efraimsson, and Dan S. Henningson. "Mode decomposition on surface-mounted cube." *Flow, turbulence and combustion*, 2012: 279-310.
- Nicoud, F., and F. Ducros. "Subgrid-scale stress modelling based on the square of the velocity gradient tensor." *Flow, turbulence and Combustion* 62(3) (1999): 183-200.

- Norberg, C., and B. Sunden. "Turbulence and Reynolds number effects on the flow and fluid forces on a single cylinder in cross flow." *ournal of Fluids and Structures* 1(3) (1987): 337-357.
- Ong, L., and J. Wallace. "The velocity field of the turbulent very near wake of a circular cylinder." *Experiments in fluids* 20(6) (1996): 441-453.
- Parnaudeau, P., D. Carlier, D. Heitz, and E. Lamballais. "Experimental and numerical studies of the flow over a circular cylinder at Reynolds number 3900." *Physics of Fluids* 20(8) (2008): 085101.
- Prsic, M. A., M. C. Ong, B. Pettersen, and D. Myrhaug. "Large Eddy Simulations of flow around a smooth circular cylinder in a uniform current in the subcritical flow regime." *Ocean engineering* 77 (2014): 61-73.
- Quen, L. K., A. Abu, N. Kato, P. Muhamad, L. K. Tan, and H. S. Kang. "Performance of two-and three-start helical strakes in suppressing the vortex-induced vibration of a low mass ratio flexible cylinder." *Ocean Engineering* 166 (2018): 253-261.
- Riches, Graham, Robert Martinuzzi, and Chris Morton. "Proper orthogonal decomposition analysis of a circular cylinder undergoing vortex-induced vibrations." *Physics of Fluids* 30(10) (2018): 105103.
- Roshko, A. "Experiments on the flow past a circular cylinder at very high Reynolds number." *J. Fluid Mech.*, 1961: 10:345-356.
- Samani, Maziar. *Study of coherent structures in turbulent flows using Proper Orthogonal Decomposition*. PhD diss., University of Saskatchewan, 2014.
- Sarwar, Wasim, and Fernando Mellibovsky. "Characterization of three-dimensional vortical structures in the wake past a circular cylinder in the transitional regime." *Physics of Fluids* 32(7) (2020): 074104.
- Schewe, G. "On the force fluctuations acting on a circular cylinder in cross-flow from subcritical up to transcritical Reynolds numbers." *J. Fluid Mech.*, 1983: 133:265-285.
- Sidebottom, W., A. Ooi, and D. Jones. "A parametric study of turbulent flow past a circular cylinder using large eddy simulation." *Journal of Fluids Engineering* 137, no. 9 (2015).
- Son, J. S., and T. J. Hanratty. "Velocity gradients at the wall for flow around a cylinder at Reynolds numbers from 5×10^3 to 10^5 ." *Journal of Fluid mechanics* 35(2) (1969): 353-368.
- Sumer, B. Mutlu, and Jorgen Fredsøe. *Hydrodynamics Around Cylindrical Structures*. World Scientific Publishing Co Pte Ltd, 2006.
- Tennekes, Hendrik, and John L. Lumley. "A first course in turbulence." *MIT press.*, 1972: 1-4.

- Weller, H. G., G. Tabor, H. Jasak, and C. Fureby. "A tensorial approach to computational continuum mechanics using object-oriented techniques." *Computers in physics* 12(6) (1998): 620-631.
- Williamson, C. H. K., and A. Roshko. "Vortex formation in the wake of an oscillating cylinder." *Journal of fluids and structures* 2(4) (1988): 355-381.
- Williamson, C. H. "Oblique and parallel modes of vortex shedding in the wake of a circular cylinder at low Reynolds numbers." *CALIFORNIA INST OF TECH PASADENA GRADUATE AERONAUTICAL LABS*, 1989: 206:579-627.